Förster energy transfer in the vicinity of a metallic nanosphere

by

José Alejandro Gonzaga Galeana

Thesis submitted to the pogram in Electronics,
Electronics Department
in partial fulfillment of the requirements for the degree of

**MASTER OF SCIENCES
IN ELECTRONICS**

at the

**National Institute of Astrophysics,
Optics and Electronics**
July 2012
Tonantzintla, Puebla

Advisor:

Dr. Jorge Roberto Zurita Sánchez
Titular researcher
Electronics Department
INAOE

Resumen

El proceso Förster es un mecanismo mediante el cual la energía de una molécula excitada (donador) puede ser transferida a una molécula cercana (aceptor) en estado base. En esta tesis, se analiza teóricamente y a fondo la influencia de una esfera nanométrica y hecha de metal (plata) sobre la rapidez de transferencia de energía Förster K_{F}. Se examina la dependencia de K_{F} con las posiciones del donador y del aceptor, el tamaño de la partícula, y las orientaciones de los momentos dipolares del aceptor y del donador. Además, se estudia el impacto de la excitación de plasmones superficiales sobre K_{F}. Existen dos canales de desexcitación del donador: la transferencia de energía Förster y el decaimiento directo de donador; se investiga la eficiencia η (probabilidad de ocurrencia) de transferencia de energía Förster, la cual caracteriza la competencia entre estos procesos de desexcitación. Se considera una respuesta dieléctrica modificada de la esfera, la cual es debida al confinamiento nanométrico de los electrones libres del metal y su interacción con el medio que los rodea. Particularmente, se obtienen gráficos de contorno de $K_{\mathrm{F}}(\mathbf{r}_{\mathrm{A}})$ (siendo $\mathbf{r}_{\mathrm{A}}$ la posición del aceptor). Las líneas de contorno de $K_{\mathrm{F}}(\mathbf{r}_{\mathrm{A}}) = k$ con un valor alto [región cercana a la posición del donador (distancia intermolecular $\lesssim 3$ nm)] practicamente no sufren cambios con la presencia de la partícula metálica, mientras que las líneas de contorno con valor bajo son fuertemente perturbadas por la presencia de la esfera y dependen de la posición del donador, de las orientaciones de los dipolos donador y aceptor, y sí los plasmones superficiales son excitados. La rapidez de transferencia de energía Förster normalizada con respecto al medio homogéneo ($K_{\mathrm{F}}/K_{\mathrm{F0}}$) es mejorada cuando el donador y el aceptor son colocados en lados opuestos de la esfera (coincidiendo con trabajos teóricos previos). Las líneas de contorno de eficiencia Förster alta [$\eta(\mathbf{r}_{\mathrm{A}}) > 0.5$] tienen la misma forma que aquellas para el medio homogéneo, pero sus longitudes son reducidas y dependen fuertemente de la posición del donador. Este efecto es originado por el enorme aumento de la rapidez de decaimiento del donador K_{D} conforme el donador se acerca a la esfera. Consecuentemente, en la región de eficiencia alta, la interacción electromagnética directa entre el donador y el aceptor domina y por lo tanto la influencia del tamaño de la nanopartícula y la excitación plasmónica es despreciable. Se discute la comparación de los resultados teóricos con los resultados de varios experimentos. En presencia de una nanopartícula, algunos de estos experimentos encontraron mejora en la eficiencia Förster y otros una reducción en la eficiencia. Artículos experimentales reportando reducción en la eficiencia concuerdan cualitativamente con los resultados presentados aquí. La excitación externa no deseada del aceptor y el tamaño de los puntos cuánticos podrían explicar la mejora en la eficiencia y por lo tanto porque estos resultados experimentales difieren de los resultados teóricos contenidos en esta tesis.

Abstract

The Förster process is a mechanism for which the energy of an excited molecule (donor) can be transfered to a nearby molecule (acceptor) in ground state. Herein, the influence of a nanoscale metallic (silver) sphere on the Förster energy transfer rate K_{F} is theoretically analyzed in depth. The dependence of donor and acceptor positions, particle size, and orientations of the acceptor and donor dipole moments on K_{F} is examined. Also, the impact of surface plasmons excitation on K_{F} is studied. There are two donor de-excitation channels: Förster energy transfer and donor direct decay, the efficiency η (occurrence likelihood) of the Förster energy transfer which characterizes the competition between these de-excitation processes is investigated. A modified dielectric response of the sphere due to the nanoscale confinement of metal free-electrons and their interaction with the surrounding medium is considered. Particularly, contour plots of $K_{\mathrm{F}}(\mathbf{r}_{\mathrm{A}})$ ($\mathbf{r}_{\mathrm{A}}$ being the acceptor position) are obtained. High-value contour lines $K_{\mathrm{F}}(\mathbf{r}_{\mathrm{A}}) = k$ [region near the donor position (intermolecular distance $\lesssim 3$ nm)] are practically unchanged with presence of the metallic particle, whereas the low-value contour lines are strongly perturbed by the presence of the sphere and they depend on donor position, orientations of the donor and acceptor dipoles, and whether surface plasmons are excited. The normalized Förster energy rate with respect to bulk medium ($K_{\mathrm{F}}/K_{\mathrm{F0}}$) is enhanced when donor and acceptor are placed on opposite sides of the sphere (coinciding with previous theoretical works). The high Förster efficiency contour lines [$\eta(\mathbf{r}_{\mathrm{A}}) > 0.5$] have the same shape as those for the bulk medium, but their lengths are reduced and depend strongly on donor position. This effect is because of the large enhancement of the donor decay rate K_{D} as the donor approaches to the sphere. Consequently, in the high efficiency region, the direct donor-acceptor electromagnetic interaction pathway dominates and therefore the influence of particle size and the plasmonic excitation is negligible. The comparison of the theoretical outcomes and the results of several experiments is discussed. In presence of the nanoparticle, some of these experiments found improvement of Förster efficiency and others efficiency reduction. Experimental papers that report efficiency reduction are in qualitative agreement with the results of this work. Unwanted external excitation of the acceptor and the dipole strength of quantum dots might explain the efficiency improvement and hence why these experimental results differ with the theoretical outcomes contained herein.

Acknowledgement

I would like to thank everyone that I met during my master studies for their support and encouragement. Above all, I am thankful to Shender for her personal support and great patience at all time, and for listening whenever I was excited or angry about my thesis. I also thank my Family for their unconditional support and words of encouragement. I wish to express my gratitude to my advisor Dr. Jorge Zurita for his support, good advice and great patience to guide me in the field of nano-optics. This thesis would not have been possible without his help. To my Friends at INAOE, I would like to thank them for their friendship and support. I thank the Faculty and Technical Staff of the National Institute of Astrophysics, Optics and Electronics for their teachings and help. I greatly appreciate the financial support for my master studies provided by the CONACYT (Scholarship No. 235182 and Basic Science Grant CB-2008/98449-F).

Contents

Chapter 1

Introduction

An excited molecule (donor) D^* can directly transfer its energy to a nearby molecule (acceptor) A in ground state. This process, illustrated in Fig. 1.1, is known as Förster energy transfer and occurs typically when the intermolecular separation R is $\lesssim 10$ nm. Actually, the energy of an excited donor molecule can be released via two pathways: (1) the energy is transferred to the acceptor molecule (Förster process) and (2) the donor molecule decays directly to its ground state as if the acceptor was absent [the released energy can be converted into radiation (fluorescence)] (see Fig. 1.1). The electromagnetic field interaction with donor and acceptor is responsible for these energy transfer and decay mechanisms. Since, as mentioned, the Förster energy transfer occurs for an intermolecular separation $R \lesssim 10$ nm, nearfields are involved (Coulomb dipole-dipole coupling). In fact, the Förster energy transfer is usually associated to a radiationless process.

The first experiments that observed Förster energy transfer were performed during the third decade of the 20th century [1]. Weigert (1920), and Gaviola and Pringsheim (1924) found that the fluorescence polarization coming out of a fluorophore solution depends on the solution concentration [2, 3]. Cario (1922) illuminated a mixture of mercury and thallium gases in such a way that only mercury atoms could be excited and he observed not only fluorescence generated

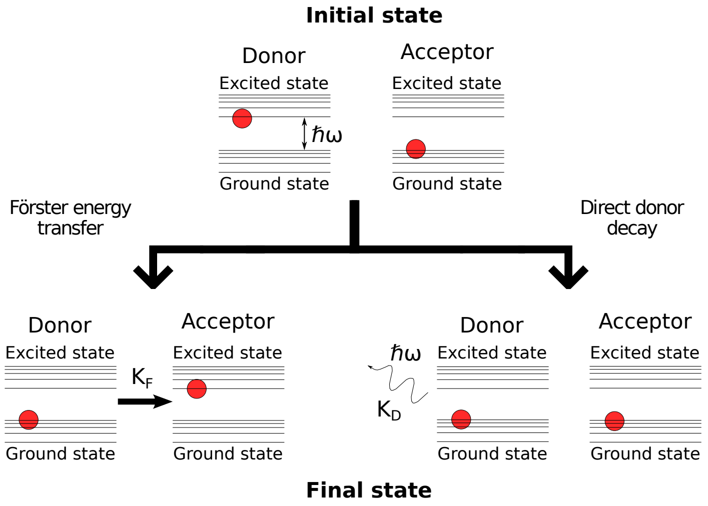

Figure 1.1: Illustration of the donor de-excitation pathways: (1) Förster energy transfer [acceptor becomes excited] and (2) direct decay [energy is released to the environment].

from the mercury atoms but also from the thallium atoms [4]. This energy transfer occurred unexpectedly at a larger distance than the collisional radii and the term ”sensitized fluorescence” was coined for the thallium fluorescence [1]. In 1925, J. Perrin explained by using classical theory that the intermolecular energy transfer happening in fluorophore solutions is due to the interaction between oscillating dipoles [1, 5]. He predicted an incorrect energy transfer rate dependence proportional to R^{-3}. Four years later, Kallmann and London presented a quantum mechanical description of collisional cross-section between two atoms for explaining the ”sensitized fluorescence” [6]. Remarkably, these authors found that the energy transfer probability varies as R^{-6}. F. Perrin developed a quantum theory of energy transfer in fluorophore solutions in 1932 and he obtained the same energy transfer rate distance dependence ($\propto R^{-3}$) as his father (J. Perrin) [7]. Actually, J. and F. Perrin studied the *coherent* energy transfer rate, namely, the frequency at which the energy would translate periodically from one molecule to the other one and viceversa (one interacting pathway). However, molecules have broadened electronic energy levels (vibrational sublevels) and there are many interacting pathways with the external environment. Consequently, the energy of the excited molecule can be released through many channels and this yields an *incoherent* mechanism of energy transfer. In a short abstract that was published in 1941, Oppenheimer elucidated that the high efficiency energy transfer between the chlorophyll molecules (photosynthesis) could be only possible if molecules are close to each other [8]. Finally, Förster also became interested in the efficient photosynthetic energy transfer process [1] and he established the current theory of intermolecular energy transfer that bears his name [9, 10]. The seminal works of Förster led to the understanding of the plant photosynthesis. By means of the Förster energy transfer mechanism, the energy absorbed by chlorophyll molecules is transported long distances until it reaches the cell reaction centers [11]. Also the Förster process takes part in energy transport inside complex molecular assemblies [12] and artificial structures (quantum dots [13, 14]). Furthermore, this process can be exploited for studying real-time dynamics of intracellular processes. The initial work on this direction was reported in 1967 by Stryer and Haugland who showed that the Förster energy transfer can be used as a spectroscopic ruler [15]. The development of this powerful tool capable of detecting nanometric displacements was enabled by the technological advances in microscopy (single molecule detection), synthesis of new fluorophores, and chemical labeling (fluorophore binding). For example, it was possible to observe the myosin motion that works as a lever arm acting on an actin filament (muscular contraction) [16], the kinesin motion for organelle transport through microtubules [17], and the DNA (deoxyribonucleic acid) folding that is activated by a non-structured hepatitis C virus protein [18].

My thesis focuses on the influence of a metallic nanoscale sphere on the intermolecular Förster energy transfer rate K_{F} of a molecular system $D^{*}A$. Since the direct donor decay and the Förster energy transfer rates are mediated by electromagnetic fields, they depend not only on intrinsic properties of molecules but also on the geometry and the dielectric properties of the objects surrounding the molecules (Purcell effect [19]). This dependence can be understood by considering that the channels in which the energy flows (electromagnetic modes) and its energetic transport capacity (molecule-mode coupling strength) is determined by the environment in which the molecules are embedded.

The initial theoretical study describing the influence on the Förster energy transfer by a metal particle (spheroid with size ~ 10 nm) was realized by Gersten et al. [20, 21]. They predicted that, when the donor and acceptor are placed at the opposite sides of the nanoscale spheroid, the Förster energy transfer rate K_{F} can be enhanced many orders of magnitude in comparison with that for free-space. In another theoretical works, the Förster energy transfer between quantum dots nearby metallic spherical solid particles (8 nm size) and nanoshells (~ 40 nm size) were investigated in Refs. [22, 23]. In these articles, a low efficiency of the Förster energy transfer was found when the quantum dots are located close to the particles. Later, the influence of smaller metallic nanoshells and nanospheres (~ 10 nm) was examined (nonlocal response of the particles was considered) [24] on the Förster energy transfer rate, obtaining enhancement in comparison to free-space. On the experimental side, ensemble fluorescent measurements of donor-acceptor pairs in the surroundings of silver islands (~ 300 nm wide and ~ 50 nm height) yielded presumably a Förster energy transfer efficiency enhancement due to the presence of the silver particle [25]. A single donor-acceptor pair experiment in the vicinity of a 20 nm diameter silver particle improved the Förster energy transfer efficiency [26]. In a sequel of this experimental work, this efficiency improvement was still observed for another particle sizes (diameters: 15 nm, 40 nm, and 80 nm) [27]. Experiments realized with donors and acceptors deposited on gold nanodisks (15 nm height and $30-80$ nm diameters) showed that the Förster energy transfer probability drops out with the presence of the nanodisk, as a consequence of donor decay rate increase [28]. In an experimental set up of concentric layers of donors and acceptors around a 50 nm size metallic particle, the efficiency of the Förster energy transfer augmented with the presence of the sphere [29]. The same result came out in subsequent experiments done by this group with smaller metallic particles (diameter 40 nm) [30]. Donor-acceptor pairs (intermolecular distance ~ 3.8 nm) were attached to gold nanodimers and single nanoparticles (40 nm size), it turned out that the Förster energy transfer rate was enhanced due to the influence of the sphere, although the efficiency of the Förster process was reduced about 9% with respect to case without nanostructure [31]. Also the same Förster energy transfer rate relative enhancement between quantum-dots sandwiching a gold nanoparticle was measured [32]. For completeness, I finally mentioned that there are other studies that treat the Förster energy transfer modification by other environments. The theoretical descriptions of this effect for a microcavity (a circular cylinder) are encountered in Refs. [33, 34] (Ref. [35]); while experiments in microcavities are reported in Refs. [36, 37]. Förster energy transfer between molecules that were placed at opposite sides of a thin metallic film (intermediated by surface plasmons) was observed [38].

On the other hand, the direct donor decay rate (as if the acceptor was absent) is strongly influenced by the environment in which is embedded. This decaying mechanism has been analyzed exhaustively in diverse environments. Early observations of this effect were realized by placing molecules a few nanometers from metallic planar surfaces [39]. During the 1970s and 1980s, many experimental studies treating this decay were extended to molecules located nearby metallic planar surfaces with sharp protuberances or metallic nanoparticles deposited on planar substrates [40, 41]. In this stage, the evidence of the influence of the environment on the molecular de-excitation rate was inferred from the optical response of an ensemble of molecules. However, as a consequence of the development of novel microscopy techniques (confocal and near-field) together with the development of techniques that enabled the grown and manipulation of artificial and natural nano-structures, the experiments of environment influence on molecular radiative properties can be done at a *single molecule* level [42–47]. As seen, the donor is de-excited through two paths: (1) direct donor decay rate K_{D} and (2) Förster energy transfer rate K_{F}. The relative difference between K_{F} and K_{D} determines which process is more probable to occur and it is related to the efficiency of the Förster process.

Since previous theoretical studies dealing with solid nanoparticles are limited to a few particular cases, my thesis is devoted to delve into the dependence of the Förster energy transfer rate with: (1) the donor and acceptor placement elsewhere in the vicinity of a metallic nanosphere, (2) the donor and acceptor dipole moment orientations, and (3) particle size. Furthermore I analyze the impact on the Förster energy transfer rate due to the electromagnetic excitation of surface plasmons (resonant collective charge oscillations) in the metallic nanoparticle. This is achieved by considering two donor-acceptor pairs: the overlap between the donor emission and acceptor absorption spectra of one of these pairs allows the excitation of these plasmons resonances (on-resonance), and the spectral overlap belonging to other pair lies far from the surface plasmon resonant frequencies (off-resonance). On the other hand, as mentioned the donor is de-excited via two pathways (Förster energy transfer and direct decay), thereof my thesis also explores the competition between this de-excitation channels (Förster efficiency) as the donor and acceptor positions and their dipole moments vary, and as the particle size changes. It is noted that results of the experimental works (listed above) are contrastable; some of these studies report improvement of efficient, while others efficiency reduction. At last, from the results that are contained herein, I address possible hypotheses to explain these differences.

My thesis is organized as follows. In Chap. 2, by using a classical approach, the Förster energy transfer rate K_{F} and the direct donor decay rate K_{D} are derived for a spatially inhomogeneous medium. Also, this chapter defines the Förster energy transfer efficiency η. Chapter 3 presents the particular expressions of K_{F} and K_{D} for the case in which the acceptor and donor molecules are located in the vicinity of a sphere (quasi-static approximation). Chapter 4 analyzes the Förster energy transfer when the molecules are nearby a *silver* spherical nanoparticle. This chapter contains numerical simulations of K_{F} and η as a function of the acceptor position for several particle sizes, donor positions, donor and acceptor dipole orientations, and off- and on-resonance cases. Also, plots of K_{D} against the donor position for several particle sizes, donor dipole orientations and the off- and on-resonance cases are included. In addition, this chapter discusses the chosen two fluorophore pairs for treating the on- and off-resonance cases along with their corresponding spectra, the embedding and silver dielectric functions, and surface plasmon resonances of nanoparticles. In Chap. 5, conclusions are presented. This thesis is complemented by four appendices. Appendix A is devoted to the Green tensor and the power released (absorbed) by a dipole (polarizable particle). The potentials originating from a point charge and a point dipole are derived in Appendix B. In Appendix C, the explicit expressions of the quasi-static Green tensor components for a sphere are shown. Appendix D explains how the normalized donor emission and acceptor absorption (imaginary part of the acceptor polarizability) spectra are obtained from data provided by the molecular probe manufacturers.

Chapter 2

Theory of Förster energy transfer in an inhomogeneous medium

The conventional quantum electrodynamics (QED) derivation of the Förster transfer rate K_{F} (the change rate of probability for finding the acceptor in the excited state) follows from a second order perturbation Fermi golden rule [48, 49]. As mentioned, molecules have broadened electronic energy levels (vibrational sublevels). Consequently, the energy can flow through many channels, and therefore the Fermi golden rule can be applied. The second order perturbation can be seen as two interacting step process in which the intermediate states are called virtual. In the case of the Förster energy transfer mechanism, the intermediate electromagnetic field states (modes) contain photons. Hence, the Förster energy transfer process involves the exchange of *virtual* photons. In this QED picture, the electromagnetic fields require to be expressed as a superposition of modes. As a consequence, this modal representation is limited for environments free of electromagnetic absorption. This seems a strong restriction because practically all materials exhibit dispersion, implying absorption (Kramers-Kronig relationships [50]). However by using concepts of statistic mechanics near equilibrium (fluctuation-dissipation theorem [51]), a quantum fluctuational representation of electromagnetic fields in presence of absorbing objects is possible [52, 53]. By

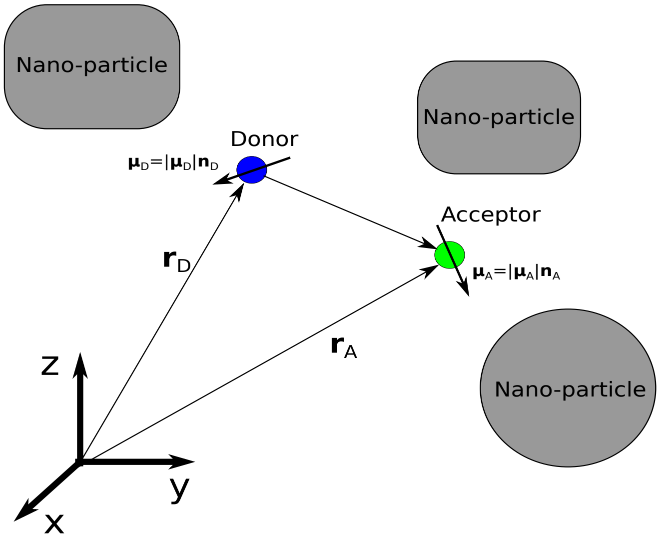

Figure 2.1: Energy transfer between two molecules placed in an inhomogeneous environment.

using this theoretical framework, the intermolecular energy transfer in an arbitrary environment has been treated by Dung et al. [54, 55]. However, a classical approach can be applied for obtaining the Förster energy transfer rate K_{F} and the direct decay K_{D} in presence of absorbing elements. Next I derive K_{F} and K_{D} for an arbitrary environment in the classical framework.

I consider two molecules as shown in Fig. 2.1. The donor (acceptor) molecule is located at $\mathbf{r}_{\mathrm{D}}$ $(\mathbf{r}_{\mathrm{A}})$ and has a transition electric dipole moment $\boldsymbol{\mu}_{\mathrm{D}}$ $(\boldsymbol{\mu}_{\mathrm{A}})$. The molecules are embedded in a linear and isotropic medium with dielectric function $\epsilon(\mathbf{r}, \omega)$ (spatially inhomogeneous) and magnetic constant $\mu = 1$ (non magnetic). The excited donor molecule can decay to the ground state either by transferring its energy to the acceptor molecule (Förster transfer) or by releasing its energy to the environment as if the acceptor molecule was absent [see Fig. 1.1]. I remark that in the classical picture the molecular transition dipoles are associated to classical dipoles.

2.1 Förster energy transfer rate

When a monochromatic electric field $\mathbf{E}_{\mathrm{i}}(\mathbf{r}, \omega)$ oscillating with angular frequency ω interacts with the acceptor molecule, the average power absorbed by the electric dipole associated with this molecule is (see Appendix A)

$$P_{\mathrm{A}}(\omega) = -\frac{\omega}{2}\text{Im}\left[\boldsymbol{\mu}_{\mathrm{A}}^{*}(\omega) \cdot \mathbf{E}_{\mathrm{i}}\left(\mathbf{r}_{\mathrm{A}}, \omega\right)\right], \tag{2.1}$$

where Im$[\ldots]$ denotes imaginary part. The acceptor dipole moment $\boldsymbol{\mu}_{A}(\omega)$ is induced by the incident electromagnetic field as

$$\boldsymbol{\mu}_{\mathrm{A}}(\omega) = \overleftrightarrow{\boldsymbol{\alpha}}_{\mathrm{A}}(\omega) \cdot \mathbf{E}_{\mathrm{i}}(\mathbf{r}_{\mathrm{A}}, \omega), \tag{2.2}$$

where $\overleftrightarrow{\boldsymbol{\alpha}}_{\mathrm{A}}(\omega)$ is the polarizability tensor of the acceptor molecule. By substituting Eq. (2.2) into Eq. (2.1) and assuming that the acceptor molecule can be only polarized along the unit vector $\mathbf{n}_{\mathrm{A}}$ [$\overleftrightarrow{\boldsymbol{\alpha}}_{\mathrm{A}}(\omega) = \alpha_{\mathrm{A}}(\omega)\mathbf{n}_{\mathrm{A}}\mathbf{n}_{\mathrm{A}}$], the absorbed power by the acceptor molecule is

$$P_{\mathrm{A}}(\omega) = \frac{\omega}{2}\text{Im}\left[\alpha_{\mathrm{A}}(\omega)\right]\left|\mathbf{n}_{\mathrm{A}} \cdot \mathbf{E}_{\mathrm{i}}(\mathbf{r}_{\mathrm{A}}, \omega)\right|^{2}. \tag{2.3}$$

In my case, the electric field $\mathbf{E}_{\mathrm{i}}(\mathbf{r}_{\mathrm{A}}, \omega)$ is precisely created by the donor molecule dipole $\boldsymbol{\mu}_{\mathrm{D}}$. This field is obtained from

$$\mathbf{E}_{\mathrm{i}}(\mathbf{r}_{\mathrm{A}}, \omega) = \frac{\omega^{2}}{c^{2}\epsilon_{0}}\overleftrightarrow{\mathbf{G}}\left(\mathbf{r}_{\mathrm{A}}, \mathbf{r}_{\mathrm{D}}; \omega\right) \cdot \boldsymbol{\mu}_{\mathrm{D}}, \tag{2.4}$$

where $\overleftrightarrow{\mathbf{G}}\left(\mathbf{r}_{\mathrm{A}}, \mathbf{r}_{\mathrm{D}}; \omega\right)$ is the Green tensor of the inhomogeneous medium in which the molecules are embedded (see Appendix A), ϵ_{o} is the vacuum permittivity, and c is the vacuum light speed. Hence from Eq. (2.4), the power absorbed by the acceptor molecule due to the field generated by the donor molecule dipole yields

$$P_{\mathrm{A}}(\omega) = \frac{\left|\boldsymbol{\mu}_{\mathrm{D}}\right|^{2}}{2\epsilon_{\mathrm{o}}^{2}}\frac{\omega^{5}}{c^{4}}\mathrm{Im}[\alpha_{\mathrm{A}}(\omega)]\left|\mathbf{n}_{\mathrm{A}} \cdot \overleftrightarrow{\mathbf{G}}(\mathbf{r}_{\mathrm{A}}, \mathbf{r}_{\mathrm{D}}; \omega) \cdot \mathbf{n}_{\mathrm{D}}\right|^{2}, \tag{2.5}$$

where the donor molecule dipole is polarized along the unit vector $\mathbf{n}_\mathrm{D}$. The Förster energy transfer rate $K_\mathrm{F}(\omega)$ can be obtained from the classical picture by using the relation [56]

$$\frac{K_\mathrm{F}(\omega)}{K_\mathrm{D0}(\omega)} = \frac{P_\mathrm{A}(\omega)}{P_\mathrm{D0}(\omega)}. \tag{2.6}$$

By neglecting the presence of the acceptor molecule, $P_\mathrm{D0}(\omega)$ is the power released by the donor dipole in free space and $K_\mathrm{D0}(\omega)$ is decay rate of the donor molecule in free space which are given by

$$P_\mathrm{D0}(\omega) = \frac{\omega^4 \left|\boldsymbol{\mu}_\mathrm{D}\right|^2}{12\pi\epsilon_\mathrm{o}c^3}, \tag{2.7}$$

$$K_\mathrm{D0}(\omega) = \frac{\omega^3 \left|\boldsymbol{\mu}_\mathrm{D}\right|^2}{3\pi\epsilon_\mathrm{o}\hbar c^3}. \tag{2.8}$$

Here $\hbar$ is the reduced Planck constant. By substituting Eqs. (2.5,2.7,2.8) into Eq. (2.6), the Förster energy transfer rate becomes

$$K_\mathrm{F}(\omega) = \frac{2\left|\boldsymbol{\mu}_\mathrm{D}\right|^2}{\hbar\epsilon_\mathrm{o}^2}\frac{\omega^4}{c^4}\mathrm{Im}\left[\alpha_\mathrm{A}(\omega)\right]\left|\mathbf{n}_\mathrm{A}\cdot\overleftrightarrow{\mathbf{G}}(\mathbf{r}_\mathrm{A},\mathbf{r}_\mathrm{D};\omega)\cdot\mathbf{n}_\mathrm{D}\right|^2. \tag{2.9}$$

Since the donor molecule emits over a range of frequencies, a spectral emission distribution function $f_\mathrm{D}(\omega)$ must be incorporated. This function is normalized as

$$\int_0^\infty f_\mathrm{D}(\omega)\,\mathrm{d}\omega = 1. \tag{2.10}$$

Then, the emission spectrum $f_\mathrm{D}(\omega)$ is inserted in Eq. (2.9) and the total Förster energy transfer rate K_F is obtained by adding the contribution of all the positive frequencies, that is,

$$K_\mathrm{F} = \frac{2\left|\boldsymbol{\mu}_\mathrm{D}\right|^2}{\hbar\epsilon_\mathrm{o}^2}\int_0^\infty f_\mathrm{D}(\omega)\frac{\omega^4}{c^4}\mathrm{Im}\left[\alpha_\mathrm{A}(\omega)\right]\left|\mathbf{n}_\mathrm{A}\cdot\overleftrightarrow{\mathbf{G}}(\mathbf{r}_\mathrm{A},\mathbf{r}_\mathrm{D};\omega)\cdot\mathbf{n}_\mathrm{D}\right|^2\mathrm{d}\omega. \tag{2.11}$$

This is the final expression for the Förster energy transfer rate. It is worth to mention that this derivation of K_F coincides with the quantum electrodynamics fluctuational approach of Ref. [54]. The Förster energy transfer can be seen as resulting from the interaction of the field created by the donor molecule with the acceptor molecule. Therefore, the Förster energy transfer rate K_{F} depends on the spectral overlap between the emission spectrum of the donor molecule and the absorption spectrum of the acceptor molecule, the orientations of the donor and acceptor dipoles, and the environment in which the molecules are embedded (Green tensor).

2.2 Donor molecule decay rate

I recall that the excited donor molecule can release its energy directly to the environment as if the acceptor molecule was absent. Then by omitting the presence of the acceptor molecule, the average energy per unit time released by the donor molecule is (see Appendix A)

$$P_{\mathrm{D}}(\omega) = \frac{\omega}{2}\mathrm{Im}[\boldsymbol{\mu}_{\mathrm{D}}^{*} \cdot \mathbf{E}_{\mathrm{i}}(\mathbf{r}_{\mathrm{D}}, \omega)]. \tag{2.12}$$

Notice that $\mathbf{E}_{\mathrm{i}}(\mathbf{r}_{\mathrm{D}})$ is the field produced by the donor molecule dipole at its own position [Eq. (2.4)]. Consequently, $P_{\mathrm{D}}(\omega)$ becomes

$$P_{\mathrm{D}}(\omega) = \frac{\omega^{3}|\boldsymbol{\mu}_{\mathrm{D}}|^{2}}{2c^{2}\epsilon_{\mathrm{o}}}\mathrm{Im}\left[\mathbf{n}_{\mathrm{D}} \cdot \overleftrightarrow{\mathbf{G}}(\mathbf{r}_{\mathrm{D}}, \mathbf{r}_{\mathrm{D}}; \omega) \cdot \mathbf{n}_{\mathrm{D}}\right]. \tag{2.13}$$

Similarly as the Förster energy transfer rate K_{F}, the donor molecule decay rate K_{D} can be obtained from the classical picture from the relation [56]

$$\frac{K_{\mathrm{D}}(\omega)}{K_{\mathrm{D0}}(\omega)} = \frac{P_{\mathrm{D}}(\omega)}{P_{\mathrm{D0}}(\omega)}. \tag{2.14}$$

By substituting Eqs. (2.7,2.8,2.13) into Eq. (2.14), the donor molecule decay rate $K_{\mathrm{D}}(\omega)$ in the absence of the acceptor molecule is

$$K_{\mathrm{D}}(\omega) = \frac{2|\boldsymbol{\mu}_{\mathrm{D}}|^2}{\hbar\epsilon_{\mathrm{o}}}\frac{\omega^2}{c^2}\mathrm{Im}\left[\mathbf{n}_{\mathrm{D}}\cdot\overleftrightarrow{\mathbf{G}}(\mathbf{r}_{\mathrm{D}},\mathbf{r}_{\mathrm{D}};\omega)\cdot\mathbf{n}_{\mathrm{D}}\right]. \tag{2.15}$$

Again, since the donor molecule emits in a spectral interval, the same spectral emission distribution $f_{\mathrm{D}}(\omega)$ must be introduced in Eq. (2.15). Therefore, the total donor molecule decay rate K_{D} is obtained by the sum of the contribution of all positive frequencies, namely,

$$K_{\mathrm{D}} = \frac{2|\boldsymbol{\mu}_{\mathrm{D}}|^2}{\hbar\epsilon_{\mathrm{o}}}\int_0^\infty f_{\mathrm{D}}(\omega)\frac{\omega^2}{c^2}\mathrm{Im}\left[\mathbf{n}_{\mathrm{D}}\cdot\overleftrightarrow{\mathbf{G}}(\mathbf{r}_{\mathrm{D}},\mathbf{r}_{\mathrm{D}};\omega)\cdot\mathbf{n}_{\mathrm{D}}\right]\,\mathrm{d}\omega. \tag{2.16}$$

From Eq. (2.16), it is evident that also K_{D} depends on the environment in which the donor molecule is located. Finally, I state that the direct released energy by the donor molecule can be either dissipated by the objects conforming the environment (Joule losses) or transformed into electromagnetic radiation. The former process is related to the non-radiative decay, whereas the latter process is related to the radiative decay.

2.3 Förster energy transfer efficiency

As seen in Secs. 2.1 and 2.2, the donor molecule can decay via two paths. As a consequence, the total donor decay is

$$K = K_{\mathrm{F}} + K_{\mathrm{D}}. \tag{2.17}$$

To measure the likelihood of the Förster energy transfer occurrence, I define the Förster efficiency as

$$\eta = \frac{K_{\mathrm{F}}}{K} = \frac{1}{1+\frac{K_{\mathrm{D}}}{K_{\mathrm{F}}}}. \tag{2.18}$$

If $K_{\mathrm{F}} \gg K_{\mathrm{D}}$ then $\eta \to 1$; the Förster energy transfer is most likely to happen. On the contrary, if $K_{\mathrm{F}} \ll K_{\mathrm{D}}$ then $\eta \to 0$; the direct donor decay is the most probable event.

Chapter 3

Förster energy transfer in the vicinity of a sphere (quasi-static approximation)

In the preceding chapter I presented a general theory of the Förster energy transfer in a spatially inhomogeneous medium. Herein I derive the explicit expressions for calculating the Förster energy transfer rate K_{F} and the direct donor decay rate K_{D} for the particular case in which the donor and the acceptor molecules are in the vicinity of a nano-sphere. To achieve this, according to previous chapter, I must obtain the electric field created by a dipole in presence of a sphere, namely, the Green tensor. The first section is devoted to the derivation of the Green tensor of a sphere embedded in an unbounded medium, the aforementioned explicit expressions for calculating K_{F} and K_{D} for this specific environment are presented in the second section.

3.1 Green tensor (quasi-static approximation)

I consider a sphere with radius a and dielectric constant $\epsilon_{\mathrm{b}}(\omega)$ that is centered at the origin (see Fig. 3.1). Moreover, the sphere is surrounded by a medium with dielectric constant $\epsilon_{\mathrm{m}}(\omega)$. The dipole source (donor) with moment $\boldsymbol{\mu}_{\mathrm{D}}$ is located outside the sphere at $\mathbf{r}_{\mathrm{D}} = z_{\mathrm{o}}\mathbf{n}_z$ ($z_{\mathrm{o}} > a$, $\mathbf{n}_z$ is the unit vector along the z-axis). For completeness, I consider that the field point $\mathbf{r}$ (acceptor position) can be inside or outside the sphere.

In my case: the molecular absorption and emission spectra lie in the visible range ($390\,\mathrm{nm} < \lambda_{\mathrm{o}} < 700\,\mathrm{nm}$, λ_{o} being the free-space wavelength), the sphere has a nanoscale size, and the molecules are located in the vicinity of the sphere. Therefore, the molecules and the sphere are enclosed in a volume $V \ll \lambda_{\mathrm{o}}^3$. Furthermore, the typical Förster range is $R \lesssim 10$ nm. By taking into account the aforementioned considerations, the electric field created by the dipole in the vicinity of the nanosphere can be well approximated by the quasi-static approach (retardation effects are neglected). Hence I use the quasi-static approximation to obtain this electric field. It is implicitly assumed that the fields and the sources oscillate harmonically with angular frequency ω [$\exp(-i\omega t)$], thus hereafter this time-dependent factor is omitted. In the quasi-static limit, the electric field can be determined from the electric potential Φ as

$$\mathbf{E}(\mathbf{r}) = -\nabla\Phi(\mathbf{r}), \tag{3.1}$$

where $\Phi(\mathbf{r})$ satisfies the Poisson equation

$$\nabla^2\Phi(\mathbf{r}) = -\frac{\rho_{\mathrm{D}}(\mathbf{r})}{\epsilon_{\mathrm{o}}\epsilon_{\mathrm{m}}}. \tag{3.2}$$

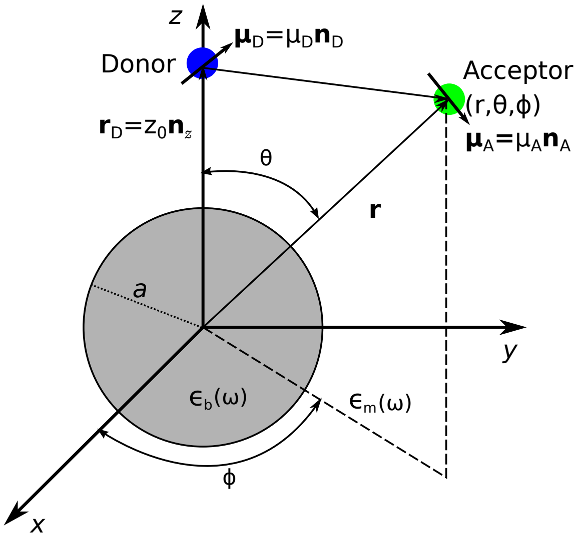

Figure 3.1: Förster energy transfer between two molecules in the vicinity of a nano-sphere. In this case, the donor molecule is placed at $\mathbf{r}_\mathrm{D} = z_\mathrm{o}\mathbf{n}_z$ and the acceptor molecule is anyywhere outside the sphere.

Here, $\rho_\mathrm{D}(\mathbf{r})$ is the charge density of the point dipole $\boldsymbol{\mu}_\mathrm{D}$ that is given by [57]

$$\rho_\mathrm{D}(\mathbf{r}) = -\boldsymbol{\mu}_\mathrm{D} \cdot \nabla\delta(\mathbf{r}-\mathbf{r}_\mathrm{D}) = -\mu_{\mathrm{D}_x}\frac{\partial}{\partial x}\delta(\mathbf{r}-\mathbf{r}_\mathrm{D}) - \mu_{\mathrm{D}_y}\frac{\partial}{\partial y}\delta(\mathbf{r}-\mathbf{r}_\mathrm{D}) - \mu_{\mathrm{D}_z}\frac{\partial}{\partial z}\delta(\mathbf{r}-\mathbf{r}_\mathrm{D}), \tag{3.3}$$

where μ_{D_j} ($j = x, y, z$) are the Cartesian components of $\boldsymbol{\mu}_\mathrm{D}$, and the partial derivatives are taken with respect to the Cartesian components of $\mathbf{r}$ (x,y,z).

Since the Laplace operator is linear and $\rho_\mathrm{D}(\mathbf{r})$ is given by the superposition of three terms [Eq. (3.3)], the solution of Eq. (3.2) can be expressed as

$$\Phi(\mathbf{r}) = \Phi_x(\mathbf{r}) + \Phi_y(\mathbf{r}) + \Phi_z(\mathbf{r}), \tag{3.4}$$

where $\Phi_j(\mathbf{r})$ ($j = x, y, z$) is the potential created by the dipole $\mu_{\mathrm{D}j}$ alone. When $|\mathbf{r}| > a$ (field point outside the sphere), there are two interacting pathways from the source point $\mathbf{r}_\mathrm{D}$ to the field point **r**: the direct path, and the path that goes first to the sphere and from there to the field point; whereas when $|\mathbf{r}| < a$ (field point inside the sphere), there is only one pathway for arriving inside the sphere.

Therefore, the electric potential $\Phi_j(\mathbf{r})$ can be written as

$$\Phi_j(\mathbf{r}) = \begin{cases} \Phi_{0_j}(\mathbf{r}) + \Phi_{1_j}(\mathbf{r}) & |\mathbf{r}| > a \\ \Phi_{2_j}(\mathbf{r}) & |\mathbf{r}| < a \end{cases}, \tag{3.5}$$

where $\Phi_{0_j}(\mathbf{r})$ is the potential created by the dipole μ_j (j=x,y,z) in the absence of sphere (direct pathway), $\Phi_{1_j}(\mathbf{r})$ is the scattering potential outside the sphere originating from the charge redistribution of the sphere [induced by the dipole μ_j (indirect pathway)], and $\Phi_{2_j}(\mathbf{r})$ is the potential inside the sphere arising from the aforementioned charge redistribution.

I can obtain the potential $\Phi(\mathbf{r})$ [Eq. (3.4)] from the potential $\Phi^{\mathrm{e}}(\mathbf{r})$ generated by a single point charge in presence of a sphere. First I add the potential $\Phi^{\mathrm{e}}(\mathbf{r})$ originated from a point charge $-q$ placed at $\mathbf{r}_{\mathrm{D}}$ and the potential $\Phi^{\mathrm{e}}(\mathbf{r})$ produced by a charge q that is displaced $\Delta s \mathbf{n}_{\mathrm{D}}$ from $\mathbf{r}_{\mathrm{D}}$ (the dipole moment of this two charges system is $\boldsymbol{\mu}_{\mathrm{D}} = q\Delta s \mathbf{n}_{\mathrm{D}}$). At last, the potential $\Phi(\mathbf{r})$ for a point dipole $\boldsymbol{\mu}_{\mathrm{D}}$ at $\mathbf{r}_{\mathrm{D}}$ is found by applying the limit $\Delta s \to 0$ in such a way that $q\Delta s$ =constant= $|\boldsymbol{\mu}_{\mathrm{D}}|$. On the other hand, to find the point charge potential $\Phi^{\mathrm{e}}(\mathbf{r})$, first I expand the known potential $\Phi^{\mathrm{e}}_0(\mathbf{r}) = q/(4\pi\epsilon_{\mathrm{o}}\epsilon_{\mathrm{m}}|\mathbf{r} - \mathbf{r}_{\mathrm{D}}|)$ (without sphere) in a multipolar series. Then, I propose that the scattering potential outside the sphere $\Phi^{\mathrm{e}}_1(\mathbf{r})$ and the potential inside the sphere $\Phi^{\mathrm{e}}_2(\mathbf{r})$ which arise from the charge redistribution induced by the point charge q admit as well multipolar expansions. Finally, the multipolar weighting coefficients of $\Phi^{\mathrm{e}}_1(\mathbf{r})$ and $\Phi^{\mathrm{e}}_2(\mathbf{r})$ series are obtained from the boundary conditions that $\Phi^{\mathrm{e}}(\mathbf{r})$ satisfies at the sphere surface. In Appendix B, the potential $\Phi(\mathbf{r})$ and $\Phi^{\mathrm{e}}(\mathbf{r})$ are derived by following the outlined methodology.

It turns out that the potential $\Phi_j(\mathbf{r})$ [Eq. (3.5)] for a field point $\mathbf{r}$ outside the sphere ($|\mathbf{r}| > a$) is given by

$$\Phi_{0_x}(\mathbf{r}) = \frac{\mu_x}{4\pi\epsilon_{\mathrm{o}}\epsilon_{\mathrm{m}}} \frac{\mathbf{R}\cdot\mathbf{n}_x}{|\mathbf{R}|^3}, \tag{3.6}$$

$$\Phi_{0_y}(\mathbf{r}) = \frac{\mu_y}{4\pi\epsilon_{\mathrm{o}}\epsilon_{\mathrm{m}}} \frac{\mathbf{R}\cdot\mathbf{n}_y}{|\mathbf{R}|^3}, \tag{3.7}$$

$$\Phi_{0_z}(\mathbf{r}) = \frac{\mu_z}{4\pi\epsilon_{\rm o}\epsilon_{\rm m}}\frac{\mathbf{R}\cdot\mathbf{n}_z}{|\mathbf{R}|^3}, \tag{3.8}$$

$$\begin{aligned}
\Phi_{1_x}(r,\theta,\phi) &= \frac{\mu_x\cos\phi}{4\pi\epsilon_{\rm o}\epsilon_{\rm m}^2}\sum_{n=1}^{\infty}\frac{\alpha_n}{z_{\rm o}^{n+2}r^{n+1}}P_n^1(\cos\theta), && (3.9)\\
\Phi_{1_y}(r,\theta,\phi) &= \frac{\mu_y\sin\phi}{4\pi\epsilon_{\rm o}\epsilon_{\rm m}^2}\sum_{n=1}^{\infty}\frac{\alpha_n}{z_{\rm o}^{n+2}r^{n+1}}P_n^1(\cos\theta), && (3.10)\\
\Phi_{1_z}(r,\theta) &= \frac{\mu_z}{4\pi\epsilon_{\rm o}\epsilon_{\rm m}^2}\sum_{n=0}^{\infty}\frac{(n+1)\alpha_n}{z_{\rm o}^{n+2}r^{n+1}}P_n(\cos\theta). && (3.11)
\end{aligned}$$

For a field point inside the sphere ($|\mathbf{r}| < a$), the potential $\Phi_j(\mathbf{r})$ is

$$\begin{aligned}
\Phi_{2_x}(r,\theta,\phi) &= \frac{\mu_x\cos\phi}{4\pi\epsilon_{\rm o}}\sum_{n=0}^{\infty}\frac{2n+1}{n\epsilon_{\rm b}+(n+1)\epsilon_{\rm m}}\frac{r^n}{z_{\rm o}^{n+2}}P_n^1(\cos\theta), && (3.12)\\
\Phi_{2_y}(r,\theta,\phi) &= \frac{\mu_y\sin\phi}{4\pi\epsilon_{\rm o}}\sum_{n=0}^{\infty}\frac{2n+1}{n\epsilon_{\rm b}+(n+1)\epsilon_{\rm m}}\frac{r^n}{z_{\rm o}^{n+2}}P_n^1(\cos\theta), && (3.13)\\
\Phi_{2_z}(r,\theta) &= \frac{\mu_z}{4\pi\epsilon_{\rm o}}\sum_{n=0}^{\infty}\frac{(2n+1)(n+1)}{n\epsilon_{\rm b}+(n+1)\epsilon_{\rm m}}\frac{r^n}{z_{\rm o}^{n+2}}P_n(\cos\theta). && (3.14)
\end{aligned}$$

Here, (r,θ,ϕ) are the spherical coordinates of the field point **r**, $\mathbf{n}_x$ ($\mathbf{n}_y$) is the unit vector along the x(y)-axis, $\mathbf{R} = \mathbf{r} - \mathbf{r}_{\rm D}$, α_n are the multipolar polarizabilities [40]

$$\alpha_n = \epsilon_{\rm m}\frac{n(\epsilon_{\rm b}-\epsilon_{\rm m})}{n\epsilon_{\rm b}+(n+1)\epsilon_{\rm m}}a^{2n+1}, \tag{3.15}$$

and P_n^1 is the associated Legendre polynomials of order 1 and degree n which is related to the corresponding Legendre polynomial P_n as

$$P_n^1(u) \equiv (1-u^2)^{\frac{1}{2}}\frac{d}{du}P_n(u). \tag{3.16}$$

Lastly, I obtain the electric field $\mathbf{E}(\mathbf{r})$ from the potential $\Phi(\mathbf{r})$ [Eq. (3.1)]. This renders

$$\mathbf{E}(\mathbf{r}) = \begin{cases} -\sum_j \nabla\left[\Phi_{0_j}(\mathbf{r}) + \Phi_{1_j}(\mathbf{r})\right] = \left[\overleftrightarrow{\mathbf{Q}}_0(\mathbf{r}, z_\mathrm{o}\mathbf{n}_z;\omega) + \overleftrightarrow{\mathbf{Q}}_1(\mathbf{r}, z_\mathrm{o}\mathbf{n}_z;\omega)\right]\cdot\boldsymbol{\mu}_\mathrm{D}, & |\mathbf{r}| > a \\ -\sum_j \nabla\Phi_{2_j}(\mathbf{r}) = \overleftrightarrow{\mathbf{Q}}_2(\mathbf{r}, z_\mathrm{o}\mathbf{n}_z;\omega)\cdot\boldsymbol{\mu}_\mathrm{D}, & |\mathbf{r}| < a \end{cases}. \tag{3.17}$$

As seen in Eq. (3.17), $\mathbf{E}(\mathbf{r})$ can be expressed in a tensorial form where $\overleftrightarrow{\mathbf{Q}}_0(\mathbf{r}, z_\mathrm{o}\mathbf{n}_z;\omega)$ is the unbounded medium quasi-static Green tensor (direct pathway), $\overleftrightarrow{\mathbf{Q}}_1(\mathbf{r}, z_\mathrm{o}\mathbf{n}_z;\omega)$ is the scattering quasi-static Green tensor (indirect pathway) and $\overleftrightarrow{\mathbf{Q}}_2(\mathbf{r}, z_\mathrm{o}\mathbf{n}_z;\omega)$ is the quasi-static Green tensor inside the sphere. The quasi-static Green tensor has the form of a 3×3 matrix, that is,

$$\overleftrightarrow{\mathbf{Q}}_k(\mathbf{r}, z_\mathrm{o}\mathbf{n}_z;\omega) = \begin{bmatrix} Q_{k_{xx}}(\mathbf{r}, z_\mathrm{o}\mathbf{n}_z;\omega) & Q_{k_{xy}}(\mathbf{r}, z_\mathrm{o}\mathbf{n}_z;\omega) & Q_{k_{xz}}(\mathbf{r}, z_\mathrm{o}\mathbf{n}_z;\omega) \\ Q_{k_{yx}}(\mathbf{r}, z_\mathrm{o}\mathbf{n}_z;\omega) & Q_{k_{yy}}(\mathbf{r}, z_\mathrm{o}\mathbf{n}_z;\omega) & Q_{k_{yz}}(\mathbf{r}, z_\mathrm{o}\mathbf{n}_z;\omega) \\ Q_{k_{zx}}(\mathbf{r}, z_\mathrm{o}\mathbf{n}_z;\omega) & Q_{k_{zy}}(\mathbf{r}, z_\mathrm{o}\mathbf{n}_z;\omega) & Q_{k_{zz}}(\mathbf{r}, z_\mathrm{o}\mathbf{n}_z;\omega) \end{bmatrix}, \quad k = 0, 1, 2. \tag{3.18}$$

Here, the components of the Green tensors $Q_{k_{ij}}$ $(i, j = x, y, z)$ are given by

$$Q_{k_{ij}}(\mathbf{r}, z_\mathrm{o}\mathbf{n}_z;\omega) = -\frac{\partial}{\partial i}\left[\frac{\Phi_{k_j}(\mathbf{r})}{\mu_j}\right]. \tag{3.19}$$

The explicit expressions for $Q_{k_{ij}}$ are found in Appendix C. Notice that I have introduced a frequency dependence in the quasi-static Green tensor. I advert that this frequency dependence appears only implicitly in the dielectric constants of the sphere $\epsilon_\mathrm{b}(\omega)$ and the surrounding medium $\epsilon_\mathrm{m}(\omega)$ [dispersion].

3.2 Quasi-static K_F and K_D for a nano-sphere

I restrict myself when the acceptor is located outside the sphere at $\mathbf{r}_A$, thus the field point is redefined as $\mathbf{r}_\mathrm{A} = \mathbf{r}$ $(|\mathbf{r}_\mathrm{A}| > a)$.

In general, the quasi-static Green tensor can be obtained from the dynamic

Green tensor as

$$\overleftrightarrow{\mathbf{Q}}(\mathbf{r},\mathbf{r}';\omega) = \lim_{\frac{\omega}{c}|\mathbf{r}-\mathbf{r}'|\to 0} \frac{\omega^2}{c^2\epsilon_{\mathrm{o}}} \overleftrightarrow{\mathbf{G}}(\mathbf{r},\mathbf{r}';\omega). \tag{3.20}$$

The Förster energy transfer rate K_{F} [Eq. (2.11)] that is valid in the quasi-static limit can be obtained by using the relationship (3.20) between the quasi-static and dynamic tensors. Therefore, the Förster energy transfer rate K_{F} in this limit is reduced to

$$K_{\mathrm{F}} = \frac{2|\boldsymbol{\mu}_{\mathrm{D}}|^2}{\hbar} \int_0^{\infty} f_{\mathrm{D}}(\omega)\mathrm{Im}[\alpha_{\mathrm{A}}(\omega)] \Big| \mathbf{n}_{\mathrm{A}} \cdot \Big[\overleftrightarrow{\mathbf{Q}}_0(\mathbf{r}_{\mathrm{A}}, z_{\mathrm{o}}\mathbf{n}_z;\omega) + \overleftrightarrow{\mathbf{Q}}_1(\mathbf{r}_{\mathrm{A}}, z_{\mathrm{o}}\mathbf{n}_z;\omega) \Big] \cdot \mathbf{n}_{\mathrm{D}} \Big|^2 \mathrm{d}\omega. \tag{3.21}$$

The donor decay rate K_{D} in the quasi-static limit must be handled with care. I recall from Eq. (2.16) that $K_{\mathrm{D}} \propto \mathrm{Im}\left[\mathbf{n}_{\mathrm{D}} \cdot \overleftrightarrow{\mathbf{G}}(\mathbf{r}_{\mathrm{D}},\mathbf{r}_{\mathrm{D}};\omega) \cdot \mathbf{n}_{\mathrm{D}}\right]$ and that $\overleftrightarrow{\mathbf{G}}(\mathbf{r}_{\mathrm{D}},\mathbf{r}_{\mathrm{D}};\omega)$ is related to the field produced by the dipole $\boldsymbol{\mu}_{\mathrm{D}}$ at its own position. Since the field point $\mathbf{r} \to \mathbf{r}_{\mathrm{D}}$ is outside the sphere, the Green tensor $\overleftrightarrow{\mathbf{G}}(\mathbf{r},\mathbf{r}_{\mathrm{D}};\omega)$ can be separated as

$$\overleftrightarrow{\mathbf{G}}(\mathbf{r},\mathbf{r}_{\mathrm{D}};\omega) = \overleftrightarrow{\mathbf{G}}_0(\mathbf{r},\mathbf{r}_{\mathrm{D}};\omega) + \overleftrightarrow{\mathbf{G}}_1(\mathbf{r},\mathbf{r}_{\mathrm{D}};\omega). \tag{3.22}$$

This is consequence of the interacting pathways that I explained in Sec. 3.1. Thus, $\overleftrightarrow{\mathbf{G}}_0(\mathbf{r},\mathbf{r}_{\mathrm{D}};\omega)$ is associated to the electric field produced by the dipole in the unbounded medium (without sphere), and $\overleftrightarrow{\mathbf{G}}_1(\mathbf{r},\mathbf{r}_{\mathrm{D}};\omega)$ is associated to the field scattered by the sphere (generated by the dipole). While the field that is scattered by the sphere back into the dipole position $\left[\propto \overleftrightarrow{\mathbf{G}}_1(\mathbf{r}_{\mathrm{D}},\mathbf{r}_{\mathrm{D}};\omega) \cdot \boldsymbol{\mu}_{\mathrm{D}}\right]$ can be well approximated by the quasi-static limit [Eq. (3.20)], the field associated to $\overleftrightarrow{\mathbf{G}}_0(\mathbf{r}_{\mathrm{D}},\mathbf{r}_{\mathrm{D}};\omega)$ in the quasi-static approximation [Eq. (3.20)] does not yield the correct description. Thus, the dynamic tensor $\overleftrightarrow{\mathbf{G}}_0(\mathbf{r}_{\mathrm{D}},\mathbf{r}_{\mathrm{D}};\omega)$ must be considered. The explicit expression for $\overleftrightarrow{\mathbf{G}}_0(\mathbf{r}_{\mathrm{D}},\mathbf{r}_{\mathrm{D}};\omega)$ is encountered in Appendix A.1.1. From Eq. (A.10), it seems at first instance that $\overleftrightarrow{\mathbf{G}}_0(\mathbf{r}_{\mathrm{D}},\mathbf{r}_{\mathrm{D}};\omega)$ diverges. However, the imaginary part of $\mathbf{n}_{\mathrm{D}} \cdot \overleftrightarrow{\mathbf{G}}_0(\mathbf{r}_{\mathrm{D}},\mathbf{r}_{\mathrm{D}};\omega)\mathbf{n}_{\mathrm{D}}$ converges to

$$\mathrm{Im}[\mathbf{n}_{\mathrm{D}} \cdot \overleftrightarrow{\mathbf{G}}_0(\mathbf{r}_{\mathrm{D}},\mathbf{r}_{\mathrm{D}};\omega) \cdot \mathbf{n}_{\mathrm{D}}] = \frac{\omega}{6\pi c}\sqrt{\epsilon_{\mathrm{m}}(\omega)}, \tag{3.23}$$

where I assume that $\mathrm{Im}\left[\epsilon_{\mathrm{m}}(\omega)\right] = 0$. As expected from the geometrical properties of an unbounded and isotropic medium, Eq. (3.23) does not depend on the dipole position $\mathbf{r}_{\mathrm{D}}$ and the dipole orientation $\mathbf{n}_{\mathrm{D}}$. From the above statements, the donor decay rate K_{D} [Eq. (3.16)] in the quasi-static limit becomes

$$K_{\mathrm{D}} = \frac{2|\boldsymbol{\mu}_{\mathrm{D}}|^2}{\hbar} \int_0^\infty f_{\mathrm{D}}(\omega) \left\{ \frac{\omega^3}{6\pi c^3 \epsilon_{\mathrm{o}}} \epsilon_{\mathrm{m}} + \mathrm{Im}\left[\mathbf{n}_{\mathrm{D}} \cdot \overleftrightarrow{\mathbf{Q}}_1(z_{\mathrm{o}}\mathbf{n}_z, z_{\mathrm{o}}\mathbf{n}_z) \cdot \mathbf{n}_{\mathrm{D}} \right] \right\} \mathrm{d}\omega. \quad (3.24)$$

The Green tensor elements $Q_{1_{ij}}(\mathbf{r}, z_{\mathrm{o}}\mathbf{n}_z; \omega)$ $(i, j = x, y, z)$ can be further simplified when $\mathbf{r} = \mathbf{r}_{\mathrm{D}} = z_{\mathrm{o}}\mathbf{n}_{\mathrm{D}}$. I found that the off-diagonal elements $Q_{1_{ij}}(z_{\mathrm{o}}\mathbf{n}_z, z_{\mathrm{o}}\mathbf{n}_z; \omega)$ $(i \neq j)$ vanish and the diagonal elements are

$$Q_{1_{xx}}(z_{\mathrm{o}}, 0, \phi; z_{\mathrm{o}}\mathbf{n}_z) = Q_{1_{yy}}(z_{\mathrm{o}}, 0, \phi; z_{\mathrm{o}}\mathbf{n}_z) = \frac{1}{4\pi\epsilon_{\mathrm{o}}\epsilon_{\mathrm{m}}^2} \sum_{n=1}^{\infty} n(n+1) \frac{\alpha_n}{z_{\mathrm{o}}^{2n+4}}, \quad (3.25)$$

$$Q_{1_{zz}}(z_{\mathrm{o}}, 0, \phi; z_{\mathrm{o}}\mathbf{n}_z) = \frac{1}{4\pi\epsilon_{\mathrm{o}}\epsilon_{\mathrm{m}}^2} \sum_{n=1}^{\infty} \frac{(n+1)^2 \alpha_n}{z_{\mathrm{o}}^{2n+4}}. \quad (3.26)$$

These results follow by the fact that

$$\Pi_n[0] = \tau_n[0] = \frac{n}{2}(n+1), \text{ and } P_n[1] = 1, \quad (3.27)$$

where $\Pi_n[\theta]$ and $\tau_n[\theta]$ are defined in Eqs. (C.23) and (C.24), respectively. The equations (3.27) can be proved by using the properties and recursion relationships of associated Legendre polynomials P_n^m [58, 59].

Chapter 4

Case study: Silver spherical nanoparticle

4.1 Molecular emission and absorption spectra

Fluorophores are light-emitting organic molecules. Once a fluorophore is excited, it eventually decays to the ground state by emitting a photon (fluorescence). The fluorophore excitation is usually done by means of light illumination in which the absorbed photon energy is larger than the emitted photon energy. Fluorophores are used as molecular probes. These molecular probes are binding structures that contain a fluorophore (label) and that can be only attached to a specific part of a target protein. Therefore, this capability for addressing particular protein sites is exploited for studying biological processes (protein folding, intracellular dynamics), and for identifying and characterizing viruses and bacteria.

Herein, I consider two different donor-acceptor pairs. The first (second) pair possesses donor emission and acceptor absorption spectra that exclude (include) silver nanoparticle plasmonic resonant frequencies. Molecular probe manufacturers usually provide spectral data of fluorophore emission (absorption) $\sigma_{\mathrm{e(a)}}(\lambda_{\mathrm{o}i})$ as a function of a set of free-space wavelength values [$\lambda_{\mathrm{o}i}$, $i = 1, 2, 3, \ldots, M$] with normalized units such that $\mathrm{Max}[\sigma_{\mathrm{e(a)}}(\lambda_{\mathrm{o}i})] = 100$. As seen previously, the normalized donor emission spectrum $f_{\mathrm{D}}(\omega)$ and the acceptor polarizability imaginary part Im$[\alpha_{\mathrm{A}}(\omega)]$ are required for calculating the Förster energy the transfer rate K_{F} and the donor decay rate K_{D}. In Appendix D, I describe how f_{D} and Im$[\alpha_{\mathrm{A}}]$ are obtained from the spectral data $\sigma_{\mathrm{e(a)}}(\lambda_{\mathrm{o}i})$.

4.1.1 Donor (Cy5)-acceptor (Cy5.5) pair (off-resonance)

The molecular pair whose spectra lie far from the sphere plasmonic resonances is composed of a Cy5 molecule (donor) and a Cy5.5 molecule (acceptor). The Cy5 and Cy5.5 belong to the cyanine dye family and they are usually synthesized with reactive groups on either one or both of nitrogen side chains for chemical linking to nucleic acids or proteins [60]. These molecules are commonly used in biological studies. Figure 4.1 shows f_{D} (Cy5) and Im$[\alpha_{\mathrm{A}}]$ (Cy5.5) as a function of the free-space wavevector k_{o} (see Appendix D).

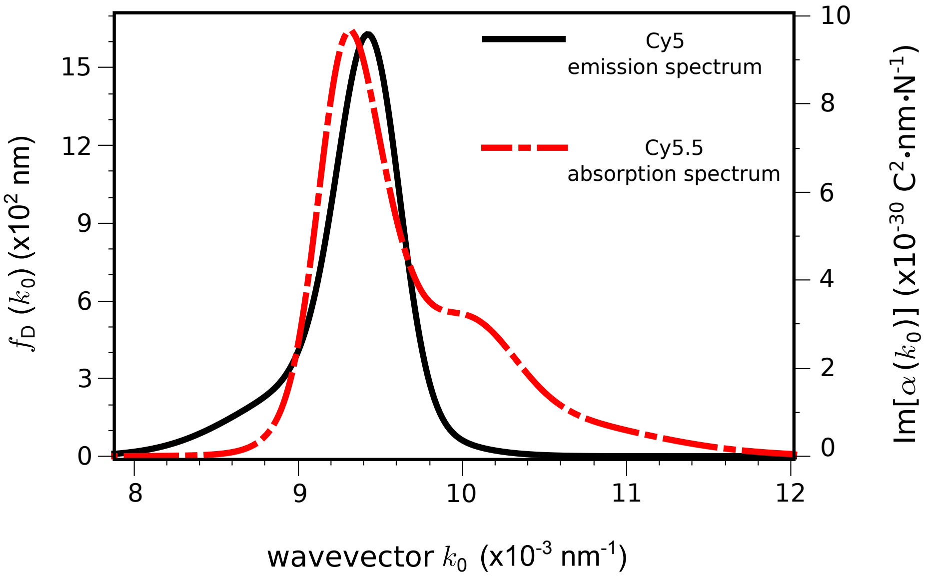

Figure 4.1: The normalized Cy5 (donor) emission spectrum f_{D} and the Cy5.5 (acceptor) absorption spectrum (Im$[\alpha_{\mathrm{A}}]$) vs. free-space wavevector k_{o}.

4.1.2 Donor (LysoTracker$^{\text{TM}}$ Blue)-acceptor (F2N12S) pair (on-resonance)

I have chosen LysoTracker$^{\text{TM}}$Blue (donor) and F2N12S (acceptor) for studying the effects arising from the sphere plasmonic resonances. The LysoTracker$^{\text{TM}}$Blue (donor) is an acidotropic probe (embedded in methanol) for labeling and tracking acidic organelles in live cells [61]. The F2N12S (acceptor) is a violet-excitable dye for detecting asymmetrical membrane changes during apoptosis (programmed cell death process) [62].

In Fig. 4.2, the donor (LysoTracker$^{\text{TM}}$Blue) normalized emission spectrum and the imaginary part of the acceptor (F2N12S) polarizability are plotted (see Appendix D). Notice that the spectral overlap for this pair is different than that for the Cy5-Cy5.5 pair (see Figs. 4.1 and 4.2).

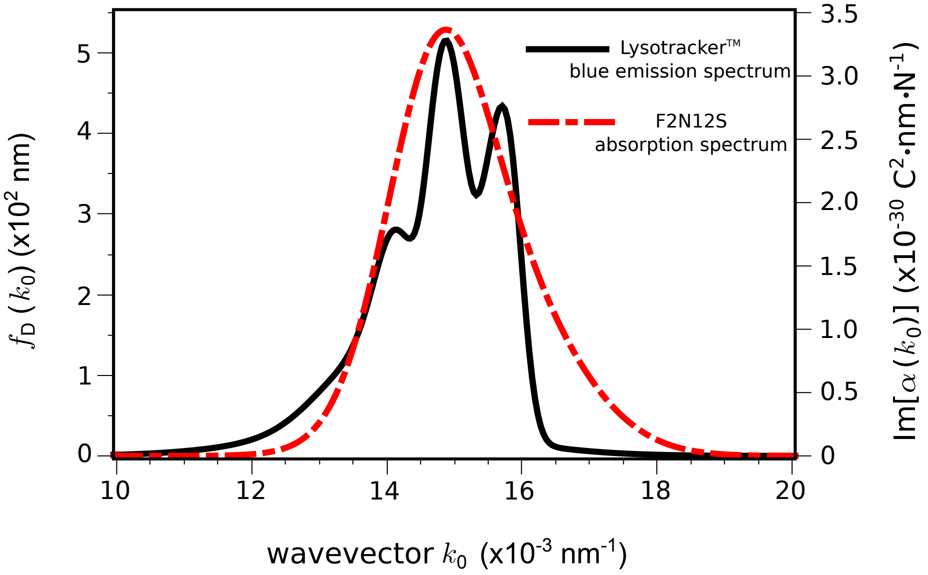

Figure 4.2: The normalized LysoTracker$^{\text{TM}}$ Blue (donor) emission spectrum f_{D} and the F2N12S (acceptor) absorption spectrum (Im$[\alpha_{\mathrm{A}}]$) vs. free-space wavevector k_{o}.

4.2 Sphere and embedding medium dielectric functions

4.2.1 Embedding medium dielectric function

The donor and acceptor molecules (fluorophores) are usually prepared in either water or a buffer solution. The latter is prepared with a weak acid (base) and its conjugate base (acid) and is resistant to pH changes when small quantities of strong acids or bases are introduced. Therefore, I consider that the molecules and the silver nanoparticle are embedded in an aqueous medium with dielectric constant $\epsilon_{\rm m}(\omega) = 1.77$ (water for optical frequencies).

4.2.2 Silver sphere dielectric function

The metal response to electromagnetic fields is associated to free conduction electrons. In this gas of electrons, the single electron ballistic motion is limited by crystal defects, impurities, electron-phonon, and electron-electron interactions. From these considerations, the electric susceptibility of a metal can be described by (Drude model)

$$\chi_{\rm d}(\omega) = -\frac{\omega_{\rm p}^2}{\omega^2 + i\tilde{\gamma}_{\rm d}\omega}, \tag{4.1}$$

where $\omega_{\rm p} = \tilde{n}e^2/(m\epsilon_0)$ is the plasma frequency [e (m) is the electron charge (effective mass) and $\tilde{n}$ is the free electron density] and $\tau_{\rm d} \equiv 1/\tilde{\gamma}_{\rm d} = \ell_\infty/\upsilon_{\rm F}$ is the average time between collisions [ℓ_∞ is the mean free path and $\upsilon_{\rm F}$ is the Fermi velocity]. For silver, $\omega_{\rm p} = 1.38 \times 10^{16}$ rad/s, $\tilde{\gamma}_{\rm d} = 2.7 \times 10^{13}$ rad/s, $\upsilon_{\rm F} = 1.4 \times 10^{15}$ nm/s, and $\ell_\infty = 52$ nm [63, 64]. However, an accurate description of the metal susceptibility should include the contribution of interband transitions (bounded electrons). This susceptibility, given by $\chi_{\rm i}(\omega)$, is significant for optical frequencies.

Therefore, the bulk dielectric function of a metal can be written as

$$\epsilon_{\mathrm{b}}(\omega) = 1 + \chi_{\mathrm{d}}(\omega) + \chi_{\mathrm{i}}(\omega). \tag{4.2}$$

When the volume ℓ^3 of a metallic particle is reduced in such a way that $\ell < \ell_\infty$, the mean free path is modified. As a consequence, the metal dielectric function of the particle is different from that of the bulk. In addition, the interaction of the free electrons with the surface atoms of the surrounding medium causes temporary charge-transfer reactions. This leads to dephasing of the collective motion of the electrons [63–65]. Experimental and theoretical studies found that the free-electron susceptibility of a metallic spherical particle is still given by the Drude model, but the damping factor is size-dependent [66], namely,

$$\chi_{\mathrm{d}}(\omega, a) = -\frac{\omega_{\mathrm{p}}^2}{\omega^2 + i\gamma_{\mathrm{d}}(a)\,\omega}, \tag{4.3}$$

where

$$\gamma_{\mathrm{d}}(a) = \tilde{\gamma}_{\mathrm{d}} + (A_1 + A_2)\frac{v_{\mathrm{F}}}{a} = \tilde{\gamma}_{\mathrm{d}} + A\frac{v_{\mathrm{F}}}{a}. \tag{4.4}$$

Here, A_1 and A_2 are dimensionless factors due to the aforementioned electron confinement and surface effects, respectively. The factor $A = A_1 + A_2$ can be accurately determined by experiments. Typical A-values are: $A = 0.25$ for vacuum, $A = 0.26$ for Ne, $A = 0.9$ for CO, $A = 1.3$ for $\mathrm{SiO_2}$, $A = 1.6$ for $\mathrm{Al_2O_3}$, and $A = 3.6$ for $\mathrm{Cr_2O_3}$ [65,66]. On the other hand, the interband susceptibility χ_{i} is not affected by the particle size reduction for clusters larger than ~ 200 atoms [63, 65]. Here this is case, thus I consider χ_{i} size-independent. Therefore, the size dependent dielectric function of the metal spherical particle is

$$\epsilon_{\mathrm{b}}(\omega, a) = 1 + \chi_{\mathrm{d}}(\omega, a) + \chi_{\mathrm{i}}(\omega). \tag{4.5}$$

In addition, nonlocal corrections (the material polarization at a certain point $\mathbf{r}$ depends on the electric field at $\mathbf{r}$ and neighboring points of $\mathbf{r}$) must be taken into account for a more exact description of electromagnetic response of a few nanometers size metallic particle. The main difference with respect to local response is that the inclusion of nonlocal effects renders the appearance of additional resonant plasmonic frequencies beyond the plasma frequency ω_p [67, 68]. Since the emission and absorption spectra are below the plasma frequency ω_p, I have disregarded nonlocal corrections.

In Fig. 4.3, the silver dielectric function ϵ_b as a function of the free-space wavelength λ_o is plotted for the bulk and particle radii $a = 2.5$ nm, 7.5 nm and 12.5 nm. Since the A-value for water is not reported elsewhere, I have chosen $A = 0.9$ (an intermediate value with respect to the aforementioned A-values). The plots of Fig. 4.3 were obtained as follows. The bulk silver dielectric function $\epsilon_\mathrm{b}(\omega)$ comes from linear interpolation in log-log scale (this linear interpolation is better than that in linear-linear scale [69, 70]) of the experimental data [71]. Then by using $\epsilon_\mathrm{b}(\omega)$ and the aforementioned Drude model silver parameters, $\chi_\mathrm{i}(\omega)$ is obtained from Eq. (4.1). Lastly, the size-dependent silver dielectric function $\epsilon_\mathrm{b}(\omega, a)$ [Eq. (4.5)] can be calculated from Eqs. (4.3) and (4.4). As seen in Fig. 4.3, the deviations of Re$[\epsilon_\mathrm{b}]$ and Im$[\epsilon_\mathrm{b}]$ with respect to the bulk increase as a decreases and λ_o increases. These deviations are more significant for Im$[\epsilon(\lambda_\mathrm{o})]$ than for Re$[\epsilon(\lambda_\mathrm{o})]$.

4.3 Surface plasmons in nanoparticles

In metallic nanoparticles, collective charge oscillations can occur. These oscillations are called surface plasmons and can be excited with electromagnetic fields. The excitation of these surface plasmons enables the nanoscale confinement of light energy.

The Mie theory describes analytically the electromagnetic response of a sphere and the conditions for light excitation surface plasmons. In Mie theory, the scattering and the sphere internal fields are expanded in a vector spherical harmonics series in which the weighting coefficients of the expansion elements depend on

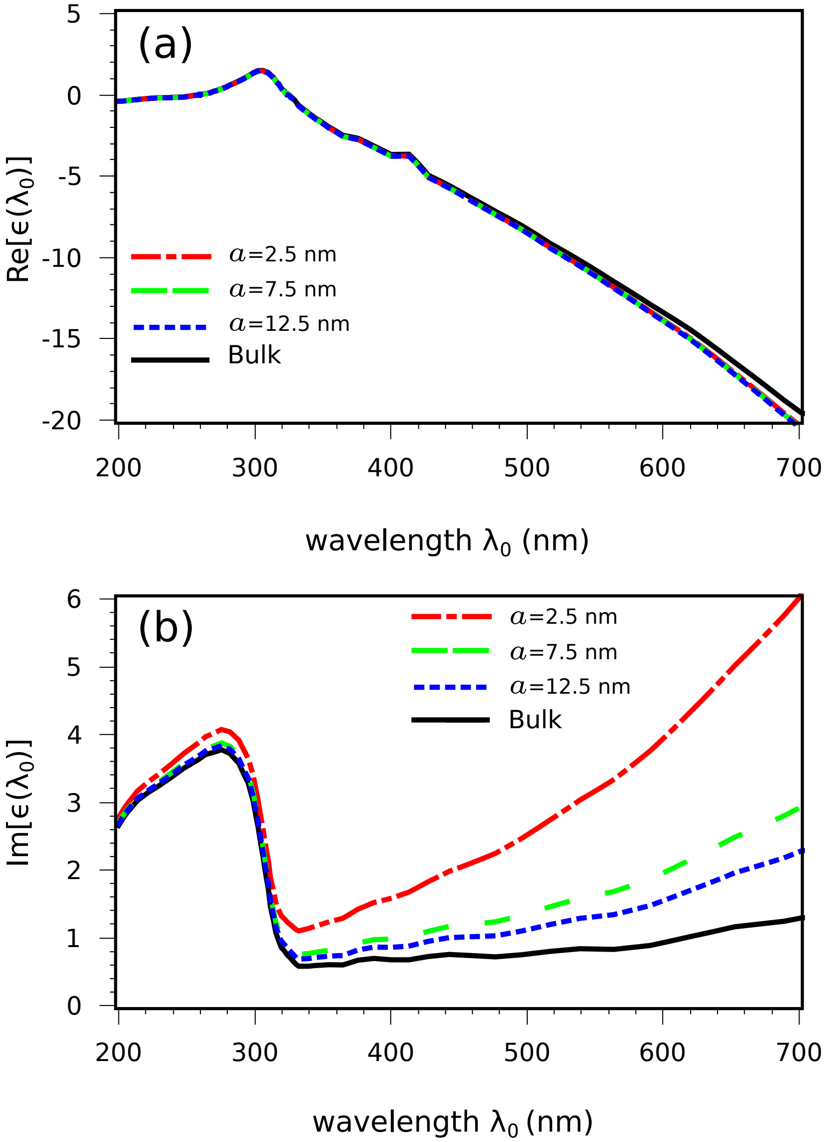

Figure 4.3: Silver dielectric function $\epsilon_{\rm p}$ as a function of the wavelength $\lambda_{\rm o}$ for the bulk and $a = 2.5$ nm, 7.5 nm and 12.5 nm. (a) Real part. (b) Imaginary part. In this case the plasma wavelength is $\lambda_{\rm p} = 137$ nm.

the excitation field. According to Mie theory in the limit $\omega\sqrt{\epsilon_{\rm m}}\,a/c \to 0$, surface plasmons can be excited when [nonmagnetic sphere ($\mu = 1$)]

$$n\epsilon_{\rm b}(\omega) + (n+1)\epsilon_{\rm m}(\omega) = 0, \tag{4.6}$$

where $n = 1, 2, 3, \ldots$. The left hand side of Eq. (4.6) shows up not only in the denominator of some of the Mie scattering and internal coefficients but also in the denominator of the quasi-static polarizabilities $\alpha_n(\omega)$ [see Eq. (3.15)]. This connection is consistent with the quasi-static approach that I am using.

To roughly estimate the localization of surface plasmons resonant frequencies, I consider that $\epsilon_{\rm m}$ is nearly constant and Im$[\epsilon_{\rm m}] = 0$ (nonabsorbing) in the spectral range in which these resonances occur and that $|$Re$[\epsilon_{\rm b}]| \gg$ Im$[\epsilon_{\rm b}]$. Hence, Eq. (4.6) under these considerations is reduced to

$$\text{Re}[\epsilon_{\rm b}(\bar{\omega}_n)] = -\frac{(n+1)}{n}\epsilon_{\rm m}, \tag{4.7}$$

where $\bar{\omega}_n$ ($n = 1, 2, 3, \ldots$) are the plasmon resonant frequencies. I remark that, in general, the resonant frequencies $\bar{\omega}_n$ depend on the particle embedding medium, the particle dielectric function, and the *geometrical shape* of the nanoparticle.

To illustrate the surface plasmon excitation by light, I assume an oscillating dipole that is placed 1 nm away from the surface of a silver sphere (embedded in water) with radius $a = 7.5$ nm. The dipole oscillates with frequencies that correspond to the free-space wavelength $\lambda_{\rm o} = 666$ nm (off-resonance), 395 nm (near dipole resonance, $n = 1$), and 371 nm (near quadrupole resonance, $n = 2$). Figure 4.4 displays the contour plots of the total electric field intensity $|\mathbf{E}(\mathbf{r})|^2$ generated by a dipole that is oriented in the x-direction and is oscillating at the aforementioned frequencies, as well as the partial *scattering* and *internal* electric field intensities of the first and second terms of the multipolar expansion [see Eq. (3.18)], namely, the dipole ($|\mathbf{E}_{\rm dp}(\mathbf{r})|^2$) and quadrupole ($|\mathbf{E}_{\rm qd}(\mathbf{r})|^2$) contributions, respectively; whereas Fig. 4.5 shows the same field intensity distributions, but the dipole is oriented in the z-direction. By comparing the left column intensity distributions of Figs. 4.4 and 4.5 with those of the middle and right columns, it can be noticed an enhancement of the scattering and internal fields due to the excitation of plasmonic resonances. As seen in Figs. 4.4 and 4.5 (middle row), the dipole intensity $|\mathbf{E}_{\rm dp}(\mathbf{r})|^2$ inside the sphere, as expected, is constant. Moreover, inside the sphere, the intensity strengths for wavelengths $\lambda_{\rm o} = 395$ nm and $\lambda_{\rm o} = 371$ nm (near resonance) are of the same order of magnitude and they are about 2 orders of magnitude larger than that for $\lambda_{\rm o} = 666$ nm (out of resonance). Conversely, outside the sphere, for the x-oriented dipole and near plasmonic resonance, the intensity $|\mathbf{E}_{\rm dp}(\mathbf{r})|^2$ decreases in a lower rate as the distance from the sphere increases for $\lambda_{\rm o} = 395$ nm (near dipole resonance) than for $\lambda_{\rm o} = 371$ nm (near quadrupole resonance). This behavior is also observed for the z-oriented dipole, but the largest intensity level that occurs at the vicinity of the sphere surface [see Fig. 4.5 middle row, and middle and right columns] is one order of magnitude larger for this dipole orientation than for the x-oriented dipole. On the other hand, inside the sphere, the quadrupole intensity $|\mathbf{E}_{\rm qd}(\mathbf{r})|^2$ varies spatially (see Figs. 4.4 and 4.5 bottom row). Also, at plasmonic resonance [Figs. 4.4 and 4.5 bottom row, and middle and right columns], the high intensity regions of $|\mathbf{E}_{\rm qd}(\mathbf{r})|^2$ are also concentrated near the sphere surface and their intensity strength can be as high as for the dipole contribution. Actually, the field confinement in the vicinity of sphere surface is the reason why these excitations are denominated surface plasmons. As side note, surface plasmons in nanoparticles can be applied in near field microscopy (resolution beyond the diffraction limit) due to aforementioned field enhancement and confinement. Since the resonant frequencies are very sensitive to the sphere surrounding dielectric function, surface plasmon can be implemented for biodetectors. Currently, the study of the optical response of metallic nanostructures (plasmonics or nanoplasmonics) is a very active research field.

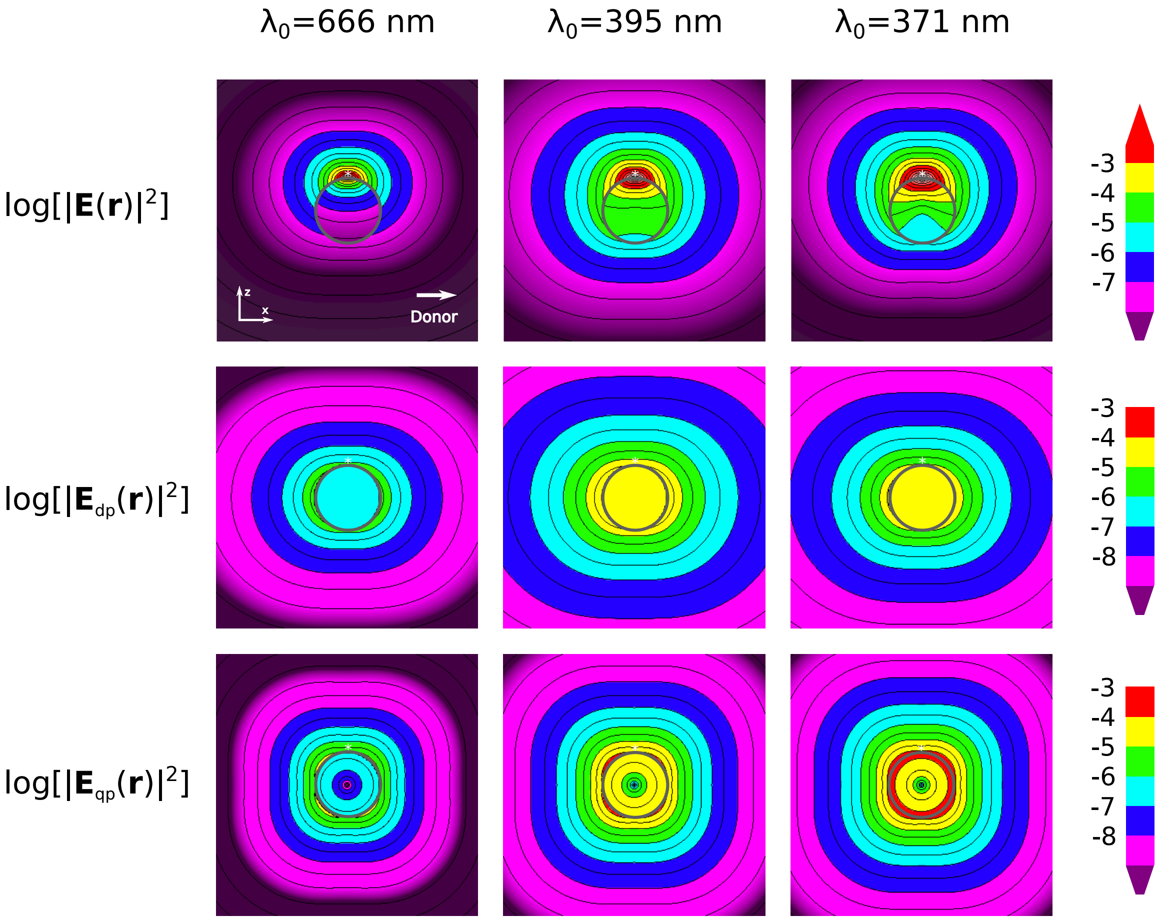

Figure 4.4: Contour plots of the electric field intensity (at the xz-plane) that is generated by the an electric dipole. The sphere has a radius $a = 7.5$ nm and is embedded in a liquid with $\epsilon_{\rm m} = 1.77$. An oscillating dipole with frequency $\omega_{\rm o} = 2\pi c/\lambda_{\rm o}$ is oriented in the x-direction and is placed 1 nm away from the sphere surface. Upper row: total electric field intensity $|\mathbf{E}(\mathbf{r})|^2$. Middle row: partial dipole contribution $|\mathbf{E}_{\rm dp}(\mathbf{r})|^2$. Bottom row: partial quadrupole contribution $|\mathbf{E}_{\rm qp}(\mathbf{r})|^2$. Left column: $\lambda_{\rm o} = 666$ nm. Middle column: $\lambda_{\rm o} = 395$ nm. Right column: $\lambda_{\rm o} = 371$ nm. The electric field intensity has arbitrary units.

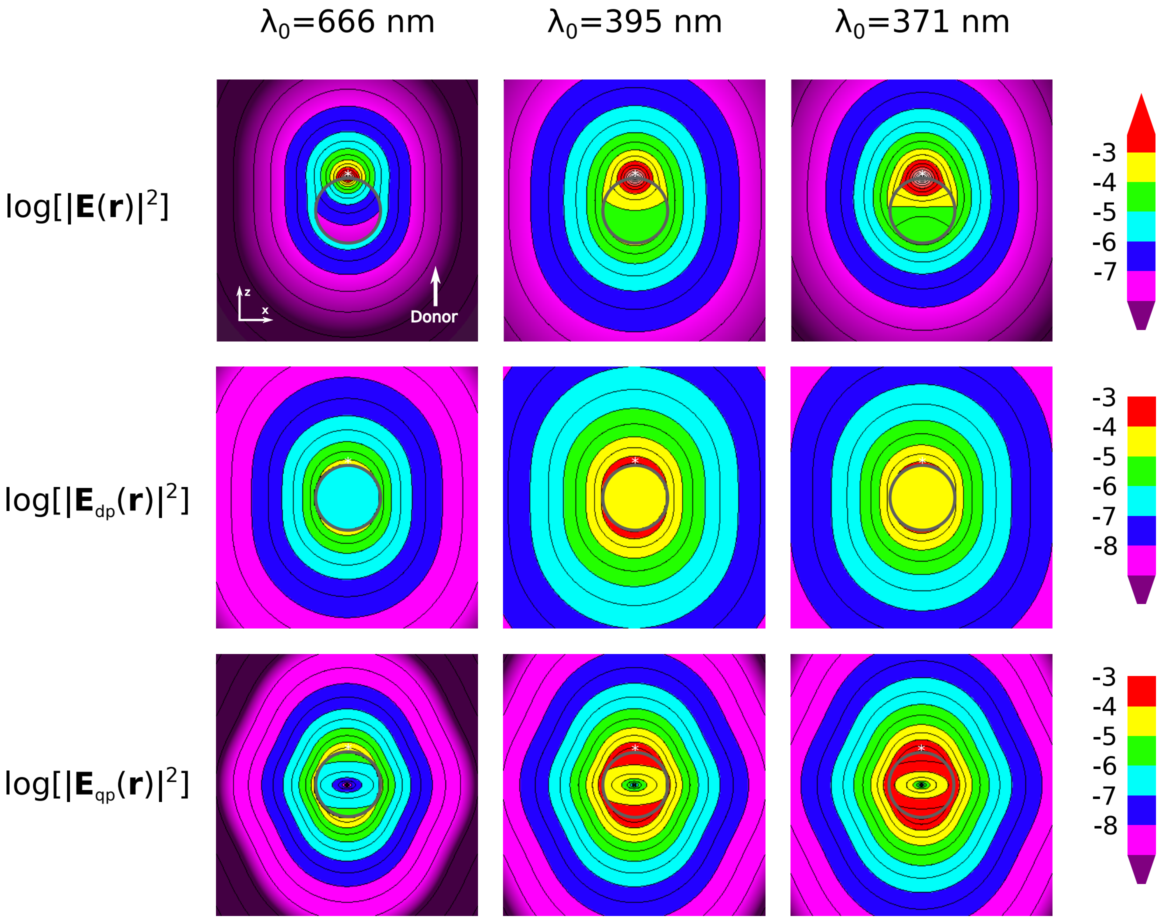

Figure 4.5: Contour plots of the electric field intensity (at the xz-plane) that is generated by the an electric dipole. The sphere has a radius $a = 7.5$ nm and is embedded in a liquid with $\epsilon_{\mathrm{m}} = 1.77$. An oscillating dipole with frequency $\omega_{\mathrm{o}} = 2\pi c/\lambda_{\mathrm{o}}$ is oriented in the z-direction and is placed 1 nm away from the sphere surface. Upper row: total electric field intensity $|\mathbf{E}(\mathbf{r})|^2$. Middle row: partial dipole contribution $|\mathbf{E}_{\mathrm{dp}}(\mathbf{r})|^2$. Bottom row: partial quadrupole contribution $|\mathbf{E}_{\mathrm{qp}}(\mathbf{r})|^2$. Left column: $\lambda_{\mathrm{o}} = 666$ nm. Middle column: $\lambda_{\mathrm{o}} = 395$ nm. Right column: $\lambda_{\mathrm{o}} = 371$ nm. The electric field intensity has arbitrary units.

4.4 Förster energy transfer rate $K_{\rm F}$

Now I study the influence on the Forster energy transfer rate $K_{\rm F}(\mathbf{r}_{\rm A}, \mathbf{r}_{\rm D})$ by the presence of a *silver* spherical nanoparticle. I consider

$$\tilde{K}_{\rm F}(\mathbf{r}_{\rm A}) \equiv K_{\rm F}(\mathbf{r}_{\rm A}, \mathbf{r}_{\rm D} = z_{\rm o}\mathbf{n}_z)/K_{\rm D0}, \tag{4.8}$$

that is, the normalized Förster energy transfer rate $K_{\rm F}(\mathbf{r}_{\rm A}, \mathbf{r}_{\rm D} = z_{\rm o}\mathbf{n}_z)$ (donor placed at the z-axis and outside the sphere) with respect to the donor decay rate *without* sphere ($K_{\rm D0}$). $K_{\rm D0}$ is the expression with the exclusion of the scattering term $[\overleftrightarrow{\mathbf{Q}}_1(\mathbf{r}_{\rm A}, z_{\rm o}\mathbf{n}_{\rm D}; \omega)]$ in Eq. (3.24). Then by using this expression for $K_{\rm D0}$ and Eq. (3.21), the ratio $K_{\rm F}/K_{\rm D0}$ is obtained. $K_{\rm D0}$ is independent of the donor position $\mathbf{r}_{\rm D}$ and the donor orientation $\mathbf{n}_{\rm D}$. Of course, I consider donor-acceptor pairs: Cy5-Cy5.5 (off-resonance) and Lysotracker$^{\rm TM}$Blue-F2N12S (on-resonance). These molecules are embedded in an aqueous medium with dielectric constant $\epsilon_{\rm m} = 1.77$.

4.4.1 Donor and acceptor dipole moments oriented in the z-direction

The normalized Förster energy transfer rate $\tilde{K}_{\rm F}(\mathbf{r}_{\rm A})$ ($\mathbf{r}_{\rm A} \in xz-$plane) is analyzed for donor and acceptor dipole moments that are oriented in the z-direction. Figure 4.6 displays contour plots of the normalized Förster energy transfer rate $\tilde{K}_{\rm F}(\mathbf{r}_{\rm A})$ for particle radius $a = 2.5$ nm, donor positions $z_{\rm o} - a = 2$ nm, 6 nm, and 12 nm, and the off(on)-resonance case [left(right) column of Fig. 4.6]. For comparison purposes, $\tilde{K}_{\rm F}$ is depicted without silver sphere (top of Fig. 4.6). As seen in Figs. 4.6(b)-(d) and (f)-(h), the contour plots of $\tilde{K}_{\rm F}$ are modified with the presence of a metallic sphere. By comparing the graphs with and without sphere, the contour lines $\log[\tilde{K}_{\rm F}] = 1, 2, 3$ that enclose a region in which the acceptor is placed very near the donor ($\lesssim 3$ nm separation) suffer only a slight change of the

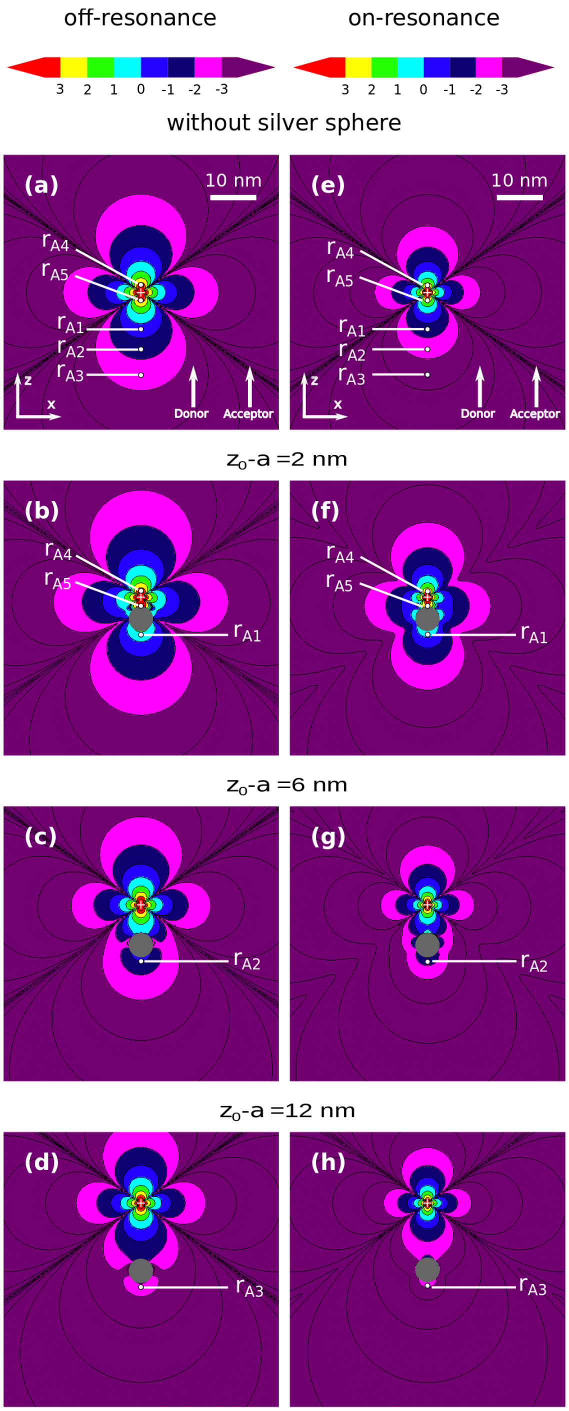

Figure 4.6: Contour plots of $\log[\tilde{K}_{\mathrm{F}}(\mathbf{r}_{\mathrm{A}})]$ ($\mathbf{r}_{\mathrm{A}}$ belongs to the xz-plane) for $a = 2.5$ nm, and both acceptor and donor dipoles oriented in the z-direction. Off-resonance: (a) without sphere, (b) $z_{\mathrm{o}} - a = 2$ nm, (c) $z_{\mathrm{o}} - a = 6$ nm, and (d) $z_{\mathrm{o}} - a = 12$ nm. On-resonance: (e) without sphere, (f) $z_{\mathrm{o}} - a = 2$ nm, (g) $z_{\mathrm{o}} - a = 6$ nm, and (h) $z_{\mathrm{o}} - a = 12$ nm. Here $z_{\mathrm{o}} - a$ is the donor-surface separation (the coordinate system origin is placed at the sphere center). Here, $\mathbf{r}_{\mathrm{A}i}$ $(i = 1, 2, 3, 4, 5)$ is a particular acceptor position, which will be used in Table 4.1 to calculate the enhancement factor $K_{\mathrm{F}}/K_{\mathrm{F0}}$.

bottom lobe when the donor is placed at a distance $z_{\rm o} - a = 2$ nm and 6 nm. [see Figs. 4.6 (a)-(c) and (e)-(g)]. In this region, the direct acceptor-donor interaction dominates, thus the influence of the sphere is weak. On the contrary, the contour lines $\log[\tilde{K}_{\rm F}] = -3, -2, -1, 0$ are greatly altered by the presence of the metallic particle. In fact, when the donor is placed near the sphere ($z_{\rm o} - a = 2$ nm), these contour lines enclose a larger area than for case without particle, as illustrated in Figs. 4.6 (a)-(b) and (e)-(f). This means that these levels of $\tilde{K}_{\rm F}$ can occur at a larger donor-acceptor separation in presence of the sphere than without the sphere. Also as seen in Figs. 4.6 (b) and (f), the shape of lobes corresponding to these contour line values are smoother for the on-resonance case than for off-resonance. This difference is due to the excitation of surface plasmons which originates strong scattering fields in the vicinity of the sphere. Unexpectedly, when the donor-surface separation is 6 nm, the area enclosed by the contour lines for $\log[\tilde{K}_{\rm F}] = -3, -2, -1, 0$ have shrunk with respect to the 2 nm donor-surface separation and even to the case in the absence of the sphere. This area enhancement-reduction effect arises as a result of the interference between the direct and scattering fields that are generated by the donor dipole (the strength of the scattering field depends strongly on the donor position). From Fig. 4.6 (g), small lateral lobes for the contour line $\log[\tilde{K}_{\rm F}] = -2$ can be noticed beside the sphere. At a donor-surface distance $z_{\rm o} - a = 12$ nm, the contour plots that are depicted in Figs. 4.6(d) and (h) look almost like their corresponding contour plots in absence of sphere [Figs. 4.6(a) and (e), respectively] with the exception of the bottom lobe for $\log[\tilde{K}_{\rm F}] = -3$. As the donor-surface separation is further increased, the patterns of the contour plots without sphere should be recovered.

The relative enhancement of the Förster energy transfer rate in presence of the nanoparticle is usually calculated with respect to Förster energy transfer rate without sphere ($K_{\rm F}/K_{\rm F0}$). This enhancement factor can be obtained from the contour plots of Fig. 4.6 as $K_{\rm F}/K_{\rm F0} = \tilde{K}_{\rm F}(\mathbf{r}'_{\rm A})/\tilde{K}_{\rm F0}(\mathbf{r}'_{\rm A})$ ($\tilde{K}_{\rm F0}$ refers to the case in which the sphere is absent and the argument $\mathbf{r}'_{\rm A}$ indicates the acceptor position

Table 4.1: Enhancement of the energy transfer Förster rate with respect the case in the absence of the sphere ($\tilde{K}_{\mathrm{F}}/\tilde{K}_{\mathrm{F0}}$) at particular points $\mathbf{r}_{\mathrm{A}i}$ (shown in Fig. 4.6 and $i = 1, \ldots, 5$) and donor locations (z_{o}). Here, the donor and acceptor dipoles are oriented in the z-direction and the sphere has a radius $a = 2.5$ nm. Note that although $z_0 - a$ and $|\mathbf{r}_{\mathrm{A}i} - \mathbf{r}_{\mathrm{D}}|$ are the same for $\mathbf{r}_{\mathrm{A4}}$ and $\mathbf{r}_{\mathrm{A5}}$, these acceptor positions are not the same.

			off-resonance	on-resonance
$\mathbf{r}_{\mathrm{A}i}$	$z_{\mathrm{o}} - a$ (nm)	$\|\mathbf{r}_{\mathrm{A}i} - \mathbf{r}_{\mathrm{D}}\|$ (nm)	$\tilde{K}_{\mathrm{F}}/\tilde{K}_{\mathrm{F0}}$	$\tilde{K}_{\mathrm{F}}/\tilde{K}_{\mathrm{F0}}$
$\mathbf{r}_{\mathrm{A1}}$	2	8	14.5164	68.6564
$\mathbf{r}_{\mathrm{A2}}$	6	12	4.0718	14.2887
$\mathbf{r}_{\mathrm{A3}}$	12	18	2.0233	6.0451
$\mathbf{r}_{\mathrm{A4}}$	2	1.5	1.0259	1.0394
$\mathbf{r}_{\mathrm{A5}}$	2	1.5	1.5548	2.0395

relative to the donor position). To illustrate the order of magnitude of $\tilde{K}_{\mathrm{F}}/\tilde{K}_{\mathrm{F0}}$, I have chosen five points $\mathbf{r}_{\mathrm{A}i}$ ($i = 1, \ldots, 5$) that are marked in Figs. 4.6 (b)-(d) and (f)-(h) (with sphere) and the corresponding points without sphere are marked in Figs. 4.6 (a) and (e). The enhancement factors $\tilde{K}_{\mathrm{F}}/\tilde{K}_{\mathrm{F0}}$ for these points are tabulated in Table 4.1. From Table 4.1, it can be noticed that a large enhancement of $\tilde{K}_{\mathrm{F}}/\tilde{K}_{\mathrm{F0}}$ occurs when the donor and acceptor are placed in the opposite sides of the sphere and the acceptor is close to the particle ($\mathbf{r}_{\mathrm{A1}}$, $\mathbf{r}_{\mathrm{A2}}$, and $\mathbf{r}_{\mathrm{A3}}$ and the intermolecular separation falls in the range $8 - 18$ nm). The largest enhancement $\tilde{K}_{\mathrm{F}}/\tilde{K}_{\mathrm{F0}}$ happens for the smallest donor-surface separation and on-resonance. On the other hand a very modest enhancement $\tilde{K}_{\mathrm{F}}/\tilde{K}_{\mathrm{F0}}$ is obtained at $\mathbf{r}_{\mathrm{A4}}$ (on top of donor and sphere) and $\mathbf{r}_{\mathrm{A5}}$ (between donor and sphere) that are just located 1.5 nm apart from the donor. From these results, the enhancement of $\tilde{K}_{\mathrm{F}}/\tilde{K}_{\mathrm{F0}}$ is greater at larger intermolecular separations. However, this enhancement of $\tilde{K}_{\mathrm{F}}/\tilde{K}_{\mathrm{F0}}$ must be carefully interpreted. Actually, the Förster energy transfer rate K_{F} at points $\mathbf{r}_{\mathrm{A1}}$, $\mathbf{r}_{\mathrm{A2}}$, and $\mathbf{r}_{\mathrm{A3}}$ is much smaller than the direct donor decay rate K_{D0}. Consequently, the direct donor decay event would be more likely to occur and therefore the Förster occurence is very unlikely. On the contrary, the Förster energy transfer rate is larger than the direct donor decay rate at $\mathbf{r}_{\mathrm{A4}}$ and $\mathbf{r}_{\mathrm{A5}}$. In this case, the Förster energy transfer occurrence is more probable than the direct decay donor process (high efficiency). Even the Förster efficiency becomes more deteriorated when the direct donor decay modification due to the presence of sphere is considered. This will be treated in detail in Secs. 4.5 and 4.6.

Figure 4.7 shows the contour plots of $\tilde{K}_{\mathrm{F}}(\mathbf{r}_{\mathrm{A}})$ for a silver sphere with radius $a = 7.5$ nm. As in Fig. 4.6, I consider the on- and off-resonance cases and the cases for which $z_{\mathrm{o}} - a = 2$ nm, 6 nm, and 12 nm. Also the top $\tilde{K}_{\mathrm{F}}(\mathbf{r}_{\mathrm{A}})$ contour plots [Figs. 4.7 (a) and (e)] correspond to the situation without sphere. Analogously to previous case ($a = 2.5$ nm), the contour lines $\log[\tilde{K}_{\mathrm{F}}] = 1, 2, 3$ are practically unchanged with the exception of the bottom lobes for the shortest donor-surface separation ($z_{\mathrm{o}} - a = 2$ nm), while the contour lines $\log[\tilde{K}_{\mathrm{F}}] = -3, -2, -1, 0$ are strongly modified with the presence of the sphere. When the donor is placed close to the surface at $z_{\mathrm{o}} = 2$ nm $+ a$, the contour lines $\log[\tilde{K}_{\mathrm{F}}] = -3, -2, -1, 0$ enclose a larger area than those for the case without sphere [see Fig. 4.7(b) and (f)]. This behavior is similar to the case for which $a = 2.5$ nm, however the enlargement of these contour lines is more remarkable [compare Fig. 4.6(b) with Fig. 4.7(b), and Fig. 4.6(f) with Fig. 4.7(f)]. Again for this donor-surface separation, the lobed patterns for the contour lines $\log[\tilde{K}_{\mathrm{F}}] = -3, -2, -1, 0$ are smoother for the on-resonance case than for off-resonance, as seen in Figs. 4.7(b) and (f). Moreover, these lobed patterns for on-resonance are even smoother than the case with a smaller particle size [see Figs. 4.7(f) and 4.6(f)]. Now let us consider the situation when donor-surface distance is increased to $z_{\mathrm{o}} - a = 6$ nm [Figs. 4.7(c) and (g)]. The area enclosed by the contour lines $\log[\tilde{K}_{\mathrm{F}}] = -3, -2, -1, 0$ is smaller for this distance than for $z_{\mathrm{o}} - a = 2$ nm, but there is the appearance of additional lateral lobes for the contour line $\log[\tilde{K}_{\mathrm{F}}] = -3$ next to the sphere and bottom lobes for the contour lines $\log[\tilde{K}_{\mathrm{F}}] = -3$ and -2 that are extended below the sphere. At last, when the donor-surface separation becomes $z_{\mathrm{o}} - a = 12$ nm, the contour line patterns almost resemble the ones without sphere [see Figs. 4.7(a,d) and (e,h)]. Overall, the main difference from the case for $a = 7.5$ nm and $a = 2.5$ nm is that the effect of the enhancement of the area enclosed is greater for the larger

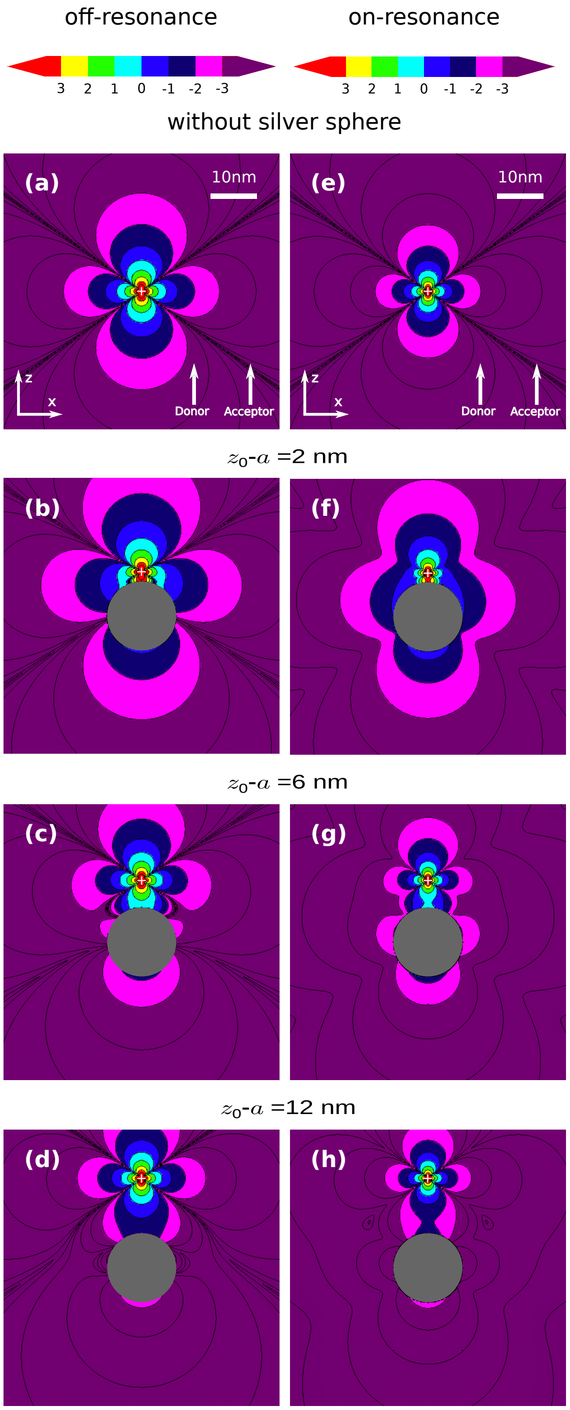

Figure 4.7: Contour plots of $\log[\tilde{K}_{\mathrm{F}}(\mathbf{r}_{\mathrm{A}})]$ ($\mathbf{r}_{\mathrm{A}}$ belongs to the xz-plane) for $a = 7.5$ nm, and both acceptor and donor dipoles oriented in the z-direction. Off-resonance: (a) without sphere, (b) $z_{\mathrm{o}} - a = 2$ nm, (c) $z_{\mathrm{o}} - a = 6$ nm, and (d) $z_{\mathrm{o}} - a = 12$ nm. On-resonance: (e) without sphere, (f) $z_{\mathrm{o}} - a = 2$ nm, (g) $z_{\mathrm{o}} - a = 6$ nm, and (h) $z_{\mathrm{o}} - a = 12$ nm. Here $z_{\mathrm{o}} - a$ is the donor-surface separation (the coordinate system origin is placed at the sphere center).

particle size. This is explained by taking into account that the strength of the multipolar polarizabilties α_n [$n = 1, 2, 3, \ldots$, Eq. (3.15)] increases as the particle size increases which yields a stronger electric field.

Next I discuss the case for which $a = 12.5$ nm. The contour plots of $\tilde{K}_\mathrm{F}(\mathbf{r}_\mathrm{A})$ are depicted in Fig. 4.8 which considers the same donor-surface distances as Figs. 4.6 and 4.7 and includes contour plots of $\tilde{K}_\mathrm{F}(\mathbf{r}_\mathrm{A})$ without sphere. It is also observed from Fig. 4.8 that only the bottom contour lines of $\log[\tilde{K}_\mathrm{F}] = 1, 2, 3$ are barely modified when the donor is located 2 nm away form the sphere surface. Conversely, as previous cases, the contour lines $\log[\tilde{K}_\mathrm{F}] = -3, -2, -1$ are modified with the presence of the sphere. The effect is strongest for the shortest donor-surface separation ($z_\mathrm{o} - a = 2$ nm). In fact, the lobed patterns corresponding to these contour curves are larger than for $a = 7.5$ nm at the same donor-surface separation ($z_\mathrm{o} - a = 2$ nm), but these dimensional changes are minimal ($\sim 10\%$), despite the sphere volume is a factor 4.63 larger [compare Fig. 4.8(b) with Fig. 4.7(b), and Fig. 4.8(f) with Fig. 4.7(f)]. Also at the donor-surface separation $z_\mathrm{o} - a = 2$ nm, in comparison with the sphere absent case, the change of the shapes for the contour lines $\log[\tilde{K}_\mathrm{F}] = -3, -2, -1$ is more notorious for the on-resonance (surface plasmon excitation) case than for the off-resonance case. Furthermore, the bottom lobe for $\log[\tilde{K}_\mathrm{F}] = -2$ shows up for the on-resonance case, whereas this lobe is absent for the off-resonance case [see Figs. 4.8(b) and (f)]. When the donor is moved to a distance $z_\mathrm{o} - a = 6$ nm from the sphere surface [Figs. 4.8(c) and (g)], the lobed patterns above the sphere look similar in shape and dimension than those for $a = 7.5$ nm; small lateral lobes for $\log[\tilde{K}_\mathrm{F}] = -3$ appear beside the sphere only for the on-resonance case, but the bottom lobe for this contour curve level emerges below the sphere for both on- and off-resonance. The contour curves $\log[\tilde{K}_\mathrm{F}]$ at a donor-surface separation $z_\mathrm{o} - a = 12$ nm almost retake the shape when sphere is absent (excluding the bottom lobes for $\log[\tilde{K}_\mathrm{F}] = -3, -2$).

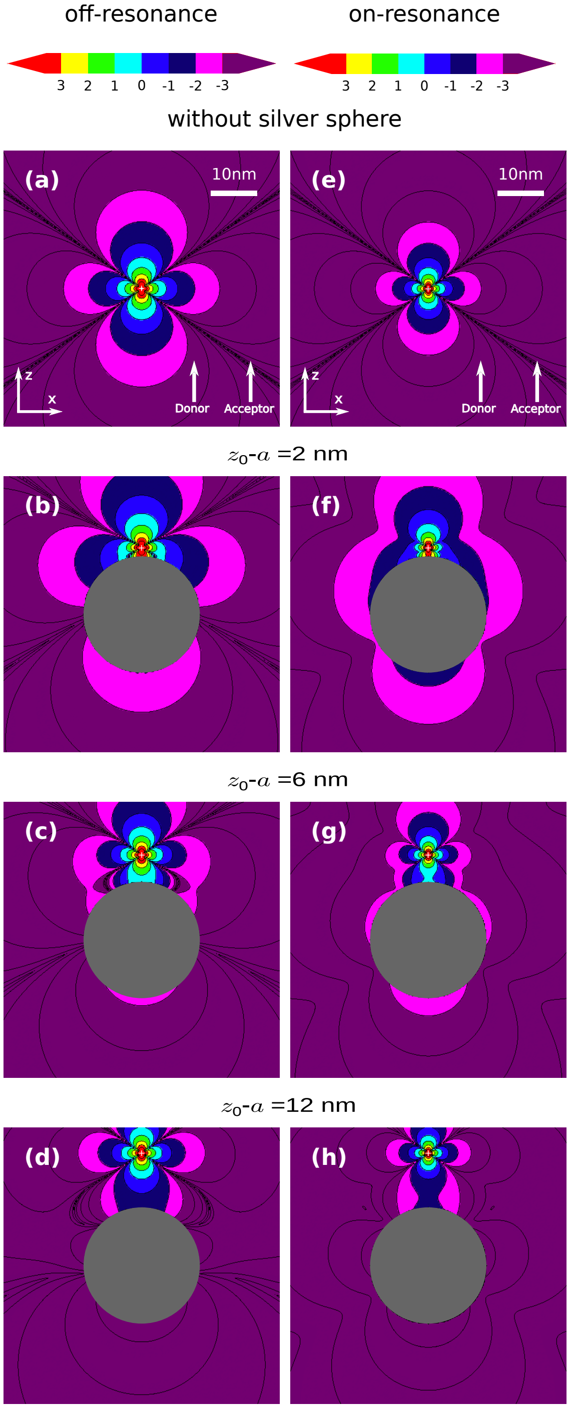

Figure 4.8: Contour plots of $\log[\tilde{K}_{\mathrm{F}}(\mathbf{r}_{\mathrm{A}})]$ ($\mathbf{r}_{\mathrm{A}}$ belongs to the xz-plane) for $a = 12.5$ nm, and both acceptor and donor dipoles oriented in the z-direction. Off-resonance: (a) without sphere, (b) $z_{\mathrm{o}} - a = 2$ nm, (c) $z_{\mathrm{o}} - a = 6$ nm, and (d) $z_{\mathrm{o}} - a = 12$ nm. On-resonance: (e) without sphere, (f) $z_{\mathrm{o}} - a = 2$ nm, (g) $z_{\mathrm{o}} - a = 6$ nm, and (h) $z_{\mathrm{o}} - a = 12$ nm. Here $z_{\mathrm{o}} - a$ is the donor-surface separation (the coordinate system origin is placed at the sphere center).

4.4.2 Donor and acceptor dipole moments oriented in the x-direction

In this section, I study $\tilde{K}_{\rm F}(\mathbf{r}_{\rm A})$ ($\mathbf{r}_{\rm A} \in xz-$ plane) when the donor and acceptor dipole moments are oriented in the x-direction. As in Sec. 4.4.1, I consider particle sizes $a = 2.5$ nm, 7.5 nm, and 12.5 nm; donor-surface separations $z_{\rm o} - a = 2$ nm, 6 nm, and 12 nm; off- and on-resonance cases.

The contour plots of $\tilde{K}_{\rm F}(\mathbf{r}_{\rm A})$ for $a = 2.5$ nm appear in Fig. 4.9. Figure 4.9 also shows the contour plots $\tilde{K}_{\rm F}(\mathbf{r}_{\rm A})$ for the bulk medium (without sphere). It can be noticed that the contour curves $\log[\tilde{K}_{\rm F}] = 1, 2, 3$ practically remain unchanged regardless of the donor-surface separation (except for the bottom lobes for $z_{\rm o} - a = 2$ nm). As mentioned, in the donor vicinity ($\lesssim 3$ nm separation), the field scattered by the sphere at the acceptor position is much weaker than the direct electric field generated by the donor. When the donor is placed at a distance 2 nm away from the sphere surface [Figs. 4.9(b) and (f)], in comparison with the bulk medium, the contour lines $\log[\tilde{K}_{\rm F}] = -3, -2, -1, 0$ are modified. The distortion of these contour curves is more notorious for the on-resonance case than for the off-resonance case. As seen in Sec. 4.4.1 this is due to the excitation of surface plasmons. Contrary to the z-oriented molecular dipoles [Figs. 4.6(b) and (f)], the area enclosed by the curves $\log[\tilde{K}_{\rm F}] = -3, -2, -1$ is not enhanced, but reduced with respect to the bulk medium. Of course, this difference arises from the sphere electromagnetic response dependence on the exciting dipole (donor) orientation. This difference can be alternately seen by considering the image description in which the field created by the dipole in vicinity of the sphere can be represented as generated by the actual dipole, an image dipole, and an image line current that are embedded in the bulk medium (the z-oriented image dipole oscillate with π phase shift with respect to the the x-oriented image dipole) [72]. Now by increasing 4 nm the donor-surface distance [Figs. 4.9(c) and (g)], the sphere influence on $\tilde{K}_{\rm F}$ is appreciably rather weak because the lobes for

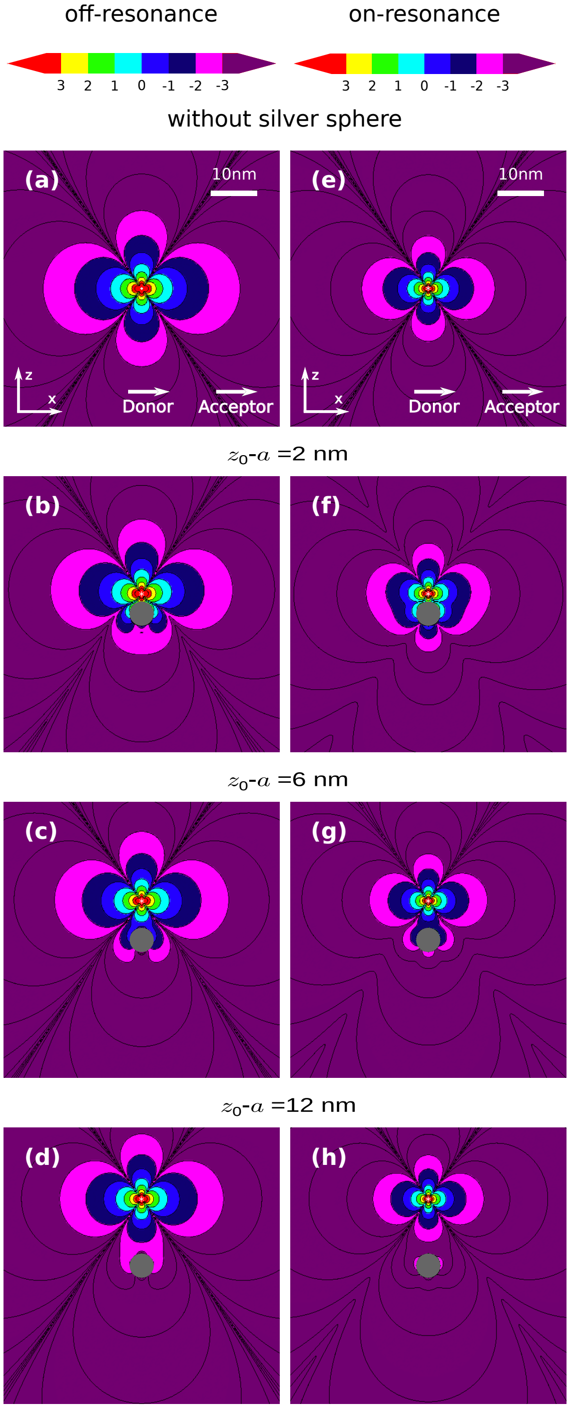

Figure 4.9: Contour plots of $\log[\tilde{K}_{\rm F}(\mathbf{r}_{\rm A})]$ ($\mathbf{r}_{\rm A}$ belongs to the xz-plane) for $a = 2.5$ nm, and both acceptor and donor dipoles oriented in the x-direction. Off-resonance: (a) without sphere, (b) $z_{\rm o} - a = 2$ nm, (c) $z_{\rm o} - a = 6$ nm, and (d) $z_{\rm o} - a = 12$ nm. On-resonance: (e) without sphere, (f) $z_{\rm o} - a = 2$ nm, (g) $z_{\rm o} - a = 6$ nm, and (h) $z_{\rm o} - a = 12$ nm. Here $z_{\rm o} - a$ is the donor-surface separation (the coordinate system origin is placed at the sphere center).

$\log[\tilde{K}_{\mathrm{F}}] = -3, -2, -1$ take already the shape for the bulk medium case (disregarding the small perturbation of the lobes that wrap the sphere). At a donor-surface distance $z_{\mathrm{o}} - a = 12$ nm for the on resonance case, the lobed patterns above the sphere resemble the ones for the bulk medium [Figs. 4.9(c) and (g)] with the exception of the $\log[\tilde{K}_{\mathrm{F}}] = -3$ bottom lobe which is elongated and envelops the sphere for off-resonance and the small $\log[\tilde{K}_{\mathrm{F}}] = -3$ side lobes next to the sphere for on-resonance. In addition, the contour patterns for $\log[\tilde{K}_{\mathrm{F}}] = -3, -2, -1, 0$ are reduced even a bit more in comparison with the $z_{\mathrm{o}} - a = 6$ nm donor-surface separation.

Now I deal with the case for which $a = 7.5$ nm. The contour plots of $\tilde{K}_{\mathrm{F}}(\mathbf{r}_{\mathrm{A}})$ are shown in Fig. 4.10. Again these contour plots consider donor-surface separations $z_{\mathrm{o}} - a = 2$ nm, 6 nm and 12 nm, the off- and on-resonace cases, and the situation without sphere. When the donor is separated 2 nm from the surface [Figs. 4.10(b) and (f)], the presence of the sphere influences strongly the lobes for $\log[\tilde{K}_{\mathrm{F}}] = -3, -2, -1, 0$ with respect to the bulk medium. This is due to the enhancement of the field as a result of the particle size increase. Also, as a consequence of the surface plasmon excitation, the lobe reshaping is more remarkable for the on-resonance case than its counterpart. Furthermore for the on-resonance case, the contour curves $\log[\tilde{K}_{\mathrm{F}}] = -3, -2, -1, 0$ envelope a larger area than for $a = 2.5$ nm [see Fig. 4.10(f) and Fig. 4.9(f)]. The opposite effect happens for the off-resonance case [see Fig. 4.10(b) and Fig. 4.9(b)]. By placing the donor at distance of 6 nm from the surface [Figs. 4.10(c) and (g)], the lateral and top lobes recapture their corresponding bulk medium shapes and are almost identical to the case for which $a = 2.5$ nm [Figs. 4.9(c) and (g)]. Only the bottom lobes suffer distortion for the contour levels $\log[\tilde{K}_{\mathrm{F}}] = -3, -2$ which partially cover the sphere. At a donor-surface separation $z_{\mathrm{o}} - a = 12$ nm, the contour curve patterns, with the exclusion of the contour line $\log[\tilde{K}_{\mathrm{F}}] = -3$, are practically equal as those for $a = 2.5$ nm [Figs. 4.10(d) and (h) and Figs. 4.9(d) and (h)]. In the off-resonance case, the bottom lobe contour line $\log[\tilde{K}_{\mathrm{F}}] = -3$ is similar as for $a = 2.5$ nm,

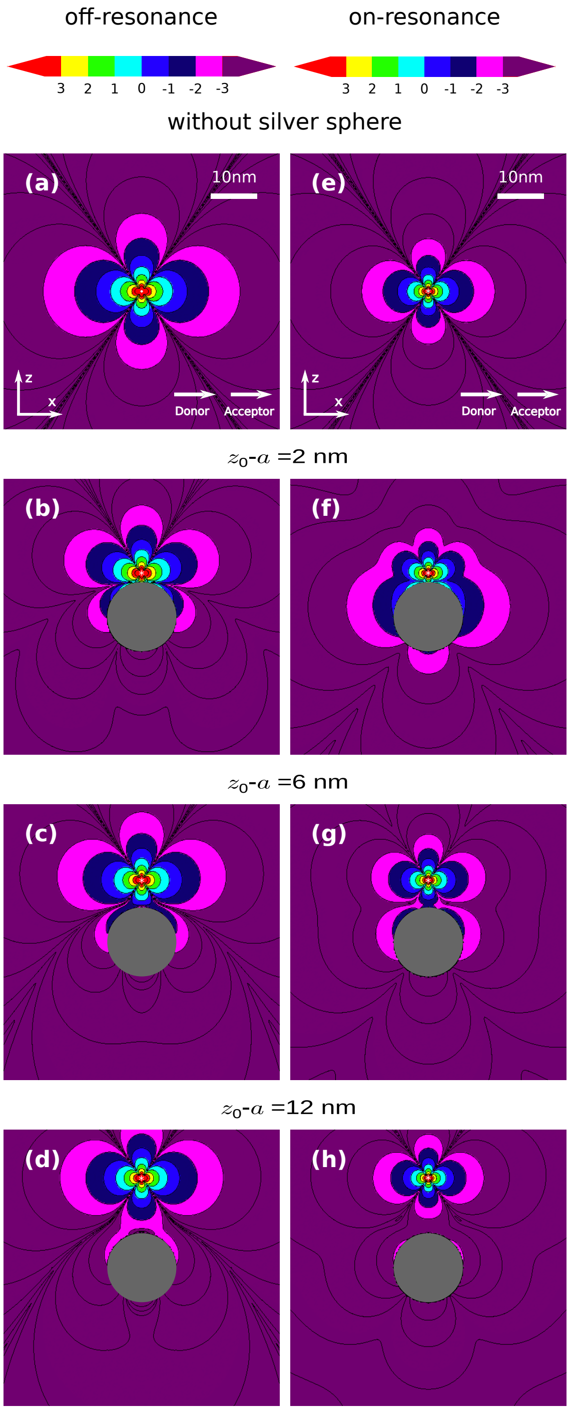

Figure 4.10: Contour plots of $\log[\tilde{K}_\mathrm{F}(\mathbf{r}_\mathrm{A})]$ ($\mathbf{r}_\mathrm{A}$ belongs to the xz-plane) for $a = 7.5$ nm, and both acceptor and donor dipoles oriented in the x-direction. Off-resonance: (a) without sphere, (b) $z_\mathrm{o} - a = 2$ nm, (c) $z_\mathrm{o} - a = 6$ nm, and (d) $z_\mathrm{o} - a = 12$ nm. On-resonance: (e) without sphere, (f) $z_\mathrm{o} - a = 2$ nm, (g) $z_\mathrm{o} - a = 6$ nm, and (h) $z_\mathrm{o} - a = 12$ nm. Here $z_\mathrm{o} - a$ is the donor-surface separation (the coordinate system origin is placed at the sphere center).

but it embraces only the upper part of the sphere; whereas in the on resonance case, the appereance of lateral side lobes beside the sphere is also similar as for $a = 2.5$ nm.

At last, the sphere radius is set to $a = 12.5$ nm, the same donor-surface separations $z_\mathrm{o} - a = 2$ nm, 6 nm, and 12 nm are considered as well as the the off- and on-resonance cases. The $\tilde{K}_\mathrm{F}(\mathbf{r}_\mathrm{A})$ contour plots for these cases are shown in Fig. 4.11, including the bulk medium case. It is noted, as all previous cases, that, with respect to the bulk medium, the contour lines $\log[\tilde{K}_\mathrm{F}] = 1, 2, 3$ are virtually unperturbed by the presence of the sphere. By comparing Fig. 4.11 ($a = 12.5$ nm) with Fig. 4.10 ($a = 7.5$ nm), there is only a modest difference of contour lines $\log[\tilde{K}_\mathrm{F}] = -3, -2, -1$, mainly in the region nearby the sphere. At a donor-surface separation $z_\mathrm{o} - a = 2$ nm and on-resonance, the lateral lobes of the contour level $\log[\tilde{K}_\mathrm{F}] = -3$ next to sphere are scarcely greater (height and width) for $a = 12.5$ nm than for $a = 7.5$ nm [see Figs. 4.11(f) and 4.10(f)]. At the same donor-surface separation, but off-resonance, the $\log[\tilde{K}_\mathrm{F}] = -3, -2$ lobes above the sphere are barely reduced for the larger sphere than the smaller one [see Figs. 4.11(b) and 4.10(b)], while the bottom lobes are adhere to the upper part of the sphere [see Fig. 4.11(b)]. The comparison of Figs. 4.11(c,g) with Figs. 4.10(c,g) [donor-surface distance 6 nm] yields that the enlargement of the particle has no effect on the lobed patterns $\log[\tilde{K}_\mathrm{F}] = -3, -2$ above the sphere. This also happens as the donor-surface distance is further increase to $z_\mathrm{o} - a = 12$ nm [see Figs. 4.11(d,h) and 4.10(d,h)].

4.4.3 Additional remarks

I recall from Appendix D that, to calculate the imaginary part of the polarizability Im$[\alpha]$ (absorption), a typical value for the magnitude of the acceptor molecule dipole moment was assumed ($|\boldsymbol{\mu}_\mathrm{A}| = 1.6 \times 10^{-29}$ Cm). Since $\tilde{K}_\mathrm{F} \propto |\boldsymbol{\mu}_\mathrm{A}|^2$, if $|\boldsymbol{\mu}_\mathrm{A}|$ is increased one order of magnitude, then the value of the contour lines of all the $\log \tilde{K}_\mathrm{F}(\mathbf{r}_\mathrm{A})$ plots would be shifted 2 orders of magnitude, namely, $\log \tilde{K}_\mathrm{F}(\mathbf{r}_\mathrm{A}) =$

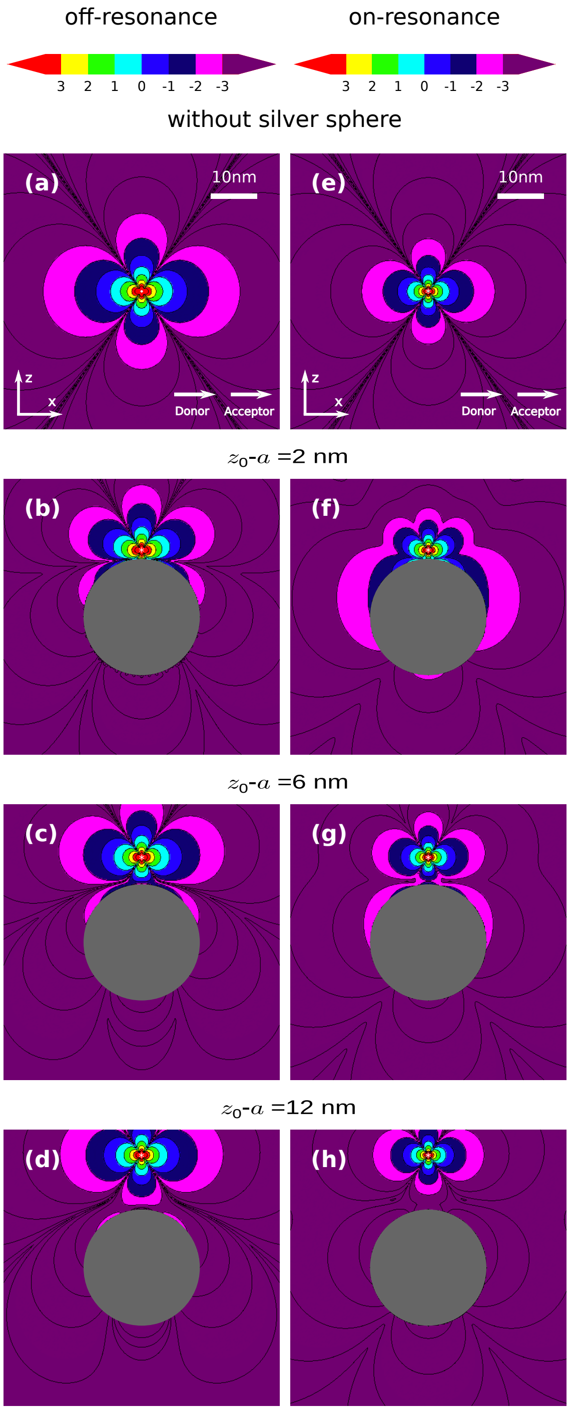

Figure 4.11: Contour plots of $\log[\tilde{K}_{\mathrm{F}}(\mathbf{r}_{\mathrm{A}})]$ ($\mathbf{r}_{\mathrm{A}}$ belongs to the xz-plane) for $a = 12.5$ nm, and both acceptor and donor dipoles oriented in the x-direction. Off-resonance: (a) without sphere, (b) $z_{\mathrm{o}} - a = 2$ nm, (c) $z_{\mathrm{o}} - a = 6$ nm, and (d) $z_{\mathrm{o}} - a = 12$ nm. On-resonance: (e) without sphere, (f) $z_{\mathrm{o}} - a = 2$ nm, (g) $z_{\mathrm{o}} - a = 6$ nm, and (h) $z_{\mathrm{o}} - a = 12$ nm. Here $z_{\mathrm{o}} - a$ is the donor-surface separation (the coordinate system origin is placed at the sphere center).

constant $\rightarrow$ constant $+ 2$. This situation can happen if instead of molecules, quantum dots are considered. This artificial structure can be seen as a large atom (~ 5 nm size), thus its dipole moment is a least one order of magnitude larger than that for a molecule.

4.5 Donor decay rate K_{D}

Now the donor direct decay rate K_{D} (as if the acceptor was absent) modification is examined in the environment with nanosphere. I present how the direct decay rate changes as a function of the donor position. Of course, I consider particularly Cy5 (off-resonance) and Lysotracker$^{\mathrm{TM}}$ Blue (on-resonance) donors that are embedded in a liquid with $\epsilon_{\mathrm{m}} = 1.77$. As in previous section, I normalize K_{D} with respect to the direct donor decay rate without nanoparticle K_{D0} as

$$\tilde{K}_{\mathrm{D}}(z_{\mathrm{o}}) \equiv K_{\mathrm{D}}(\mathbf{r}_{\mathrm{D}} = z_0 \mathbf{n}_{\mathrm{D}})/K_{\mathrm{D0}}. \tag{4.9}$$

K_{D} is obtained from Eq. (3.24).

4.5.1 z-direction oriented donor dipole moment

First I analyze the normalized donor decay rate $\tilde{K}_{\mathrm{D}}$ when the donor dipole moment is oriented in the z-direction. Figure 4.12 displays $\tilde{K}_{\mathrm{D}}$ against $z_{\mathrm{o}} - a$ for $a = 2.5$ nm, 7.5 nm, and 12.5 nm, and on- and off-resonance cases. As seen in Fig. 4.12, when the donor is placed in the vicinity of the sphere, its decay rate is influenced strongly by the metallic nanosphere. A donor-surface separation of a few nanometers yields at least 3 orders of magnitude decay rate enhancement with respect to K_{D0}. I recall that the decay rate is proportional to the energy released by the dipole in which a part of the energy is converted into radiation and the other part is dissipated in the sphere (Joule losses) [Eq. (2.14)]. Since the donor dipole is located in the vicinity of the sphere, it can excite all multipoles whose

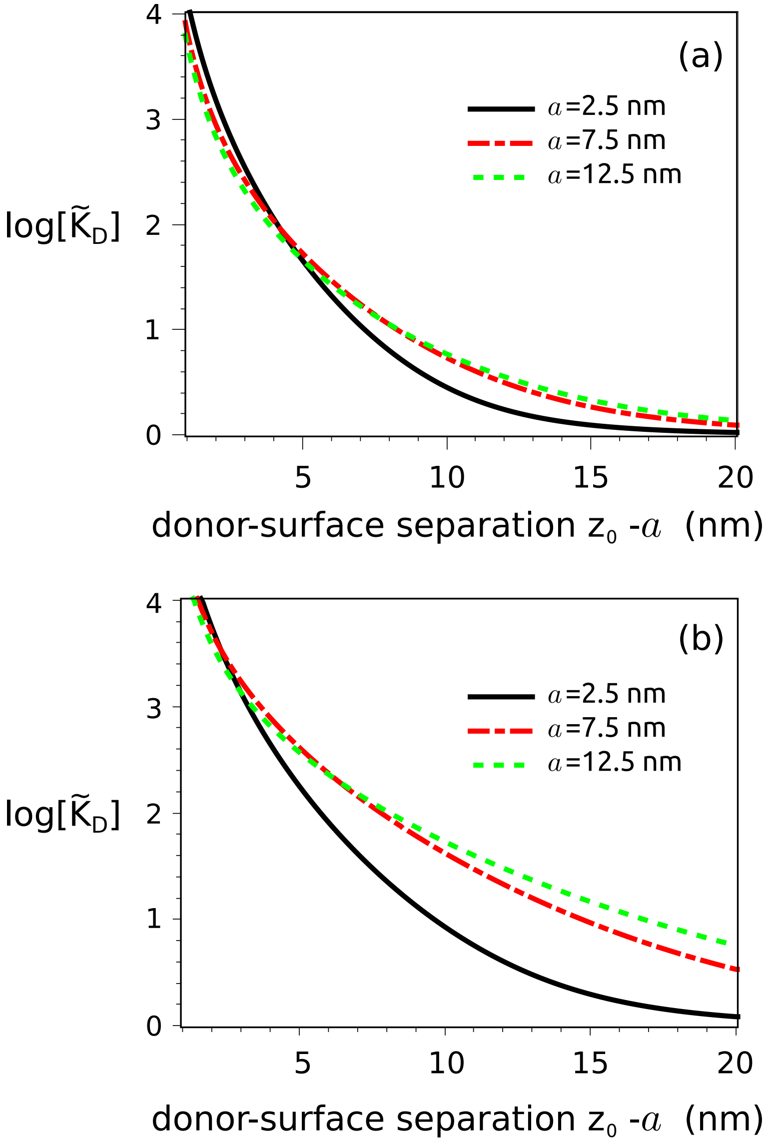

Figure 4.12: Normalized donor decay rate $\tilde{K}_{\mathrm{D}}$ against $z_{\mathrm{o}} - a$ for a z-direction oriented donor dipole moment and sphere radii $a = 2.5$ nm, 7.5 nm and 12.5 nm. (a) Off-resonance case. (b) On resonance.

strength is determined by the donor-surface separation and material dielectric properties of the sphere which depends on the driving frequency. As seen, the metallic particle can be simultaneously a good scatterer and good absorber, thus the enhancement of the decay rate is not surprising. Moreover, since the radiated energy arises from the lowest order multipole (dipole), the higher order multipoles contribute only to the dissipation [41, 73]. Also, it can be observed that, at a certain donor-surface distance, the decay rate enhancement is larger for the on-resonance case than for the off-resonance case. This is consequence of the surface plasmons excitation which enhances the internal field inside the sphere and scattered field by the sphere. In the off-resonance case, the $\tilde{K}_{\mathrm{D}}$ curves for $a = 7.5$ nm and 12.5 nm are almost identical [Fig. 4.12(a)]; in the opposite case [Fig. 4.12(b)], this sameness applies only if the donor-surface separation is less than 7 nm (when $z_{\mathrm{o}} - a > 7$ nm, the $\tilde{K}_{\mathrm{D}}$ curve for $a = 7.5$ nm decreases a bit faster than for $a = 12.5$ nm). The $\tilde{K}_{\mathrm{D}}$ curves intersect at $z_{\mathrm{o}} - a \approx 4$ nm(≈ 2.5 nm$)$ for off(on)-resonance. For the smallest particle, $\tilde{K}_{\mathrm{D}}$ decreases more rapidly than the other particle sizes as the donor-surface separation is augmented from the aforementioned crossing distances [see Fig. 4.12]. As might be expected, as the donor distance from the sphere grows, $\tilde{K}_{\mathrm{D}} \to 1$. The on-resonance $\tilde{K}_{\mathrm{D}}$ curves take a longer donor-surface separation for reaching nearly the value of 1. On the other hand, when the donor-surface separation is smaller than the intersecting points [$z_{\mathrm{o}} - a \approx 4$ nm (≈ 2.5 nm) for off(on)-resonance], the K_{D} curves deviate slightly from each other regardless of the different particle sizes. Even, in the off-resonance case, the magnitude of $\tilde{K}_{\mathrm{D}}$ is greater for $a = 2.5$ nm than for the other particle radii.

4.5.2 x-direction oriented donor dipole moment

Now the donor dipole moment is oriented in the x-direction. In Fig. 4.13, the normalized decay rate $\tilde{K}_{\mathrm{D}}$ as a function of the donor-surface separation $z_{\mathrm{o}} -$

a is shown for sphere radii $a = 2.5$ nm, 7.5 nm and 12.5 nm, and off- and on-resonance cases. Again for this dipole orientation, the decay rate $\tilde{K}_{\rm D}$ of the donor is greatly influenced when it is placed in the vicinity of a metal particle. Also the enhancement of the decay rate $\tilde{K}_{\rm D}$ is larger for the on-resonance case that for the off-resonance case, although $\tilde{K}_{\rm D}$ is weaker in comparison with the z-direction oriented dipole moment. Furthermore by comparing the $\tilde{K}_{\rm D}$ curves of Fig. 4.13(a) [Fig. 4.13(b)] with Fig. 4.12(a) [Fig. 4.12(b)], it is noticed that the behavior of these curves for the x- and z-oriented dipoles are similar. In the off-resonance case, $\tilde{K}_{\rm D}$ curves are nearly independent of the the particle radius a when $z_{\rm o} - a \lesssim 4$ nm, whereas $\tilde{K}_{\rm D}$ for $a = 2.5$ nm deviates downwards from the $\tilde{K}_{\rm D}$ curves for $a = 7.5$ nm and 12 nm in the range $z_{\rm o} - a \gtrsim 4$ nm. On the other hand, in the on-resonance case, the shown $\tilde{K}_{\rm D}$ curves are almost equal close to the sphere until $z_{\rm o} - a$ reaches about 3 nm and therefrom $\tilde{K}_{\rm D}$ for $a = 7.5$ nm and 12.5 nm separate upwardly from the curve for $a = 2.5$ nm and then the $\tilde{K}_{\rm D}$ curves for $a = 7.5$ nm and 12.5 nm bifurcate at $z_{\rm o} - a \sim 6$ nm ($\tilde{K}_{\rm D}$ being greater for $a = 12.5$ nm than for $a = 7.5$ nm). In relation to the z-direction oriented donor dipole case, $\tilde{K}_{\rm D}$ decreases faster to the level $\tilde{K}_{\rm D} = 1$ as $z_{\rm o} - a$ increases.

4.6 Förster energy transfer efficiency η

As mentioned, the donor can be de-excited via two pathways: the Förster energy transfer and the direct donor decay. In Secs. 4.4 and 4.5, I analyzed separately the Förster energy transfer rate $K_{\rm F}$ and the direct donor decay rate $K_{\rm D}$, respectively. The relative difference between these rates defines which de-excitation mechanism is more probable for happening. This section is devoted to the analysis of the likelihood of the Förster process when the molecules are nearby the spherical nanoparticle. I recall from Sec. 2.3 that this likelihood can be quantified by the efficiency η defined in Eq. (2.18). I rewrite Eq. (2.18) in terms of $\tilde{K}_{\rm F}(\mathbf{r}_{\rm A})$

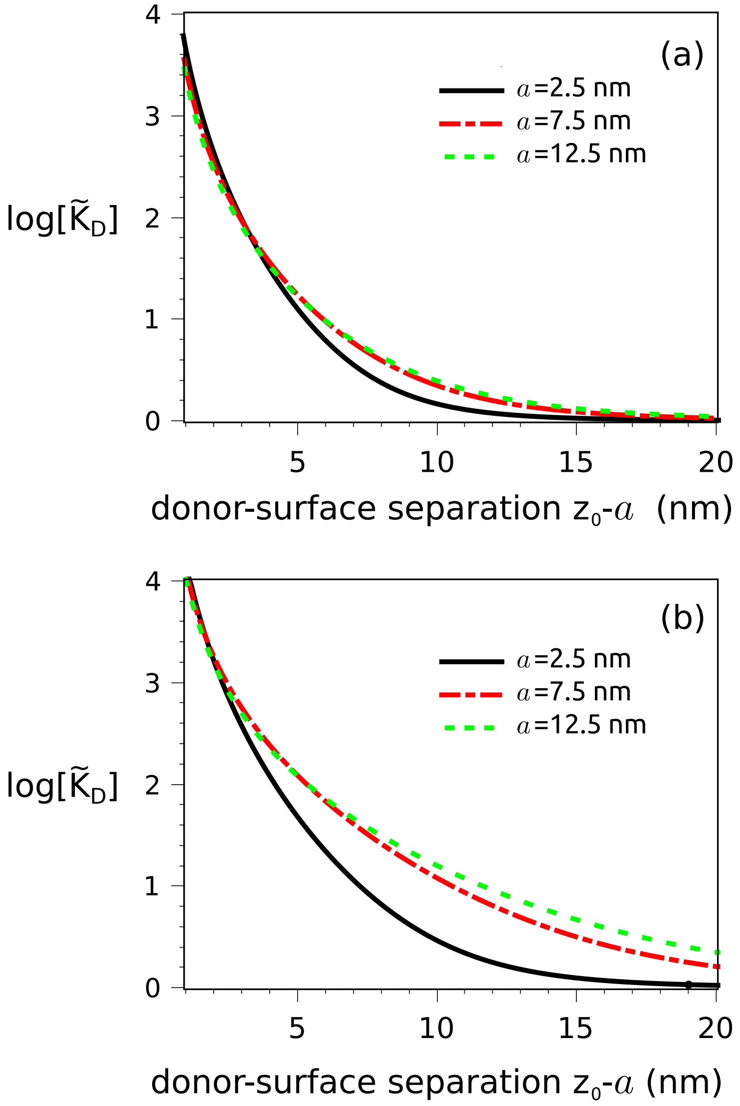

Figure 4.13: Normalized donor decay rate $\tilde{K}_{\mathrm{D}}$ against $z_{\mathrm{o}} - a$ for a x-direction oriented donor dipole moment and sphere radii $a = 2.5$ nm, 7.5 nm and 12.5 nm. (a) Off-resonance case. (b) On resonance.

and $\tilde{K}_{\rm D}(z_{\rm o})$ as

$$\eta(\mathbf{r}_{\rm A}) \equiv \frac{\tilde{K}_{\rm F}(\mathbf{r}_{\rm A})}{\tilde{K}_{\rm F}(\mathbf{r}_{\rm A}) + \tilde{K}_{\rm D}(z_{\rm o})} = \frac{1}{1 + \tilde{K}_{\rm D}(z_{\rm o})/\tilde{K}_{\rm F}(\mathbf{r}_{\rm A})}. \tag{4.10}$$

I consider the particular analyzed cases in Secs. 4.4 and 4.5, thus the calculations of $\tilde{K}_{\rm F}(\mathbf{r}_{\rm A})$ and $\tilde{K}_{\rm D}(z_{\rm o})$ in these sections are directly substituted into Eq. (4.10) for obtaining the efficiency $\eta(\mathbf{r}_{\rm A})$.

4.6.1 z-direction oriented donor and acceptor dipole moments

In this section I assume that donor and acceptor dipole moments are oriented in the z-direction. The contour plots of the Förster energy transfer efficiency $\eta(\mathbf{r}_{\rm A})$ ($\mathbf{r}_{\rm A} \in xz-$plane) for $a = 2.5$ nm are shown in Fig. 4.14. Figure 4.14 also includes contour plots of $\eta(\mathbf{r}_{\rm A})$ for the bulk medium (on top). When the donor-surface distance is $z_{\rm o} - a = 2$ nm [Figs. 4.14(b) and (f)], the contour line patterns are reduced (about a factor of 3) in comparison with the free-sphere case. Also the shape of lobes is practically unchanged with the presence of the sphere, excepting a small perturbation of the bottom lobes for $\eta \leq 0.4$ nearby the sphere surface. An additional parameter, commonly used for measuring the limiting extension of the high efficiency Förster region, is the Förster radius $R_{\rm o}$. The Förster radius $R_{\rm o}$ is the intermolecular distance for which $\tilde{K}_{\rm F} = \tilde{K}_{\rm D}$. Then from Eq. (4.10), the Förster radius $R_{\rm o}$ corresponds to $\eta = 0.5$ (this efficiency level is indicated with a black solid contour line in all efficiency contour plots). According to Fig. 4.12, $\log \tilde{K}_{\rm D} \approx 3.2$ (3.6) at a 2 nm donor-surface separation for off-resonance (on-resonance), thus region of high Förster efficiency happens for $\log \tilde{K}_{\rm F} > 3.2\ (3.6)$, namely, the region [$\lesssim 2$ nm around the donor] that is dominated by the direct donor-acceptor interaction [see Sec. 4.4]. Therefore, this is the reason why the lobed contour lines are simply reduced bulk patterns (this reduction being smaller for on-resonance case than for off-resonance case). When the donor is moved further from the sphere at a donor-surface separation $z_{\rm o} - a = 6$ nm [Figs. 4.14(c) and (g)], the same

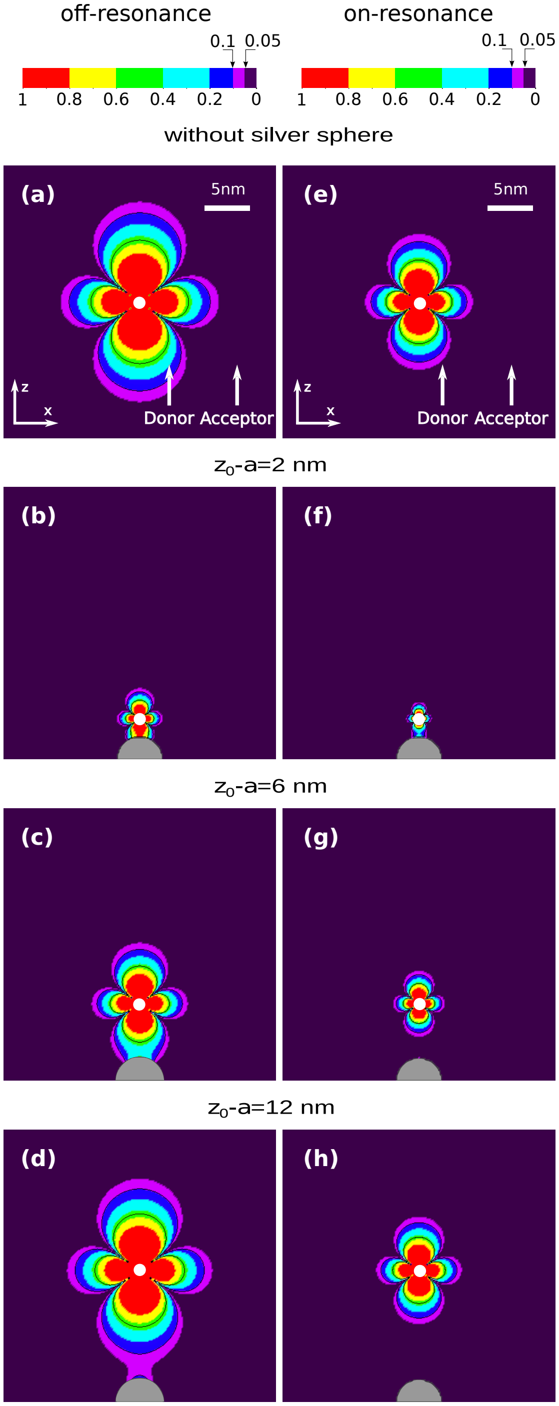

Figure 4.14: Contour plots of $\eta(\mathbf{r}_\mathrm{A})$ ($\mathbf{r}_\mathrm{A} \in xz$-plane) for $a = 2.5$ nm, and donor and acceptor dipole moments oriented in the z-direction. Off-resonance: (a) without sphere, (b) $z_\mathrm{o} - a = 2$ nm, (c) $z_\mathrm{o} - a = 6$ nm, and (d) $z_\mathrm{o} - a = 12$ nm. On-resonance: (e) without sphere, (f) $z_\mathrm{o} - a = 2$ nm, (g) $z_\mathrm{o} - a = 6$ nm, and (h) $z_\mathrm{o} - a = 12$ nm. Here $z_\mathrm{o} - a$ is the donor-surface separation (the coordinate system origin is placed at the sphere center).

behavior of scale reduction and unaltered shape of the efficiency contour lines is observed, but the efficiency patterns are larger than for $z_{\mathrm{o}} - a = 2$ nm. This is explained by the fact that the normalized direct decay $\log \tilde{K}_{\mathrm{D}}$ has decreased to 1.2 (2) for off-resonance (on-resonance) and the area for which $\log \tilde{K}_{\mathrm{F}} > 1.2$ (2) is still dominated by the direct donor-acceptor interaction. At a donor-surface separation $z_{\mathrm{o}} - a = 12$ nm [Figs. 4.14(c) and (g)] the efficiency contour lines of the bulk medium are almost recovered (these contour lines are slightly reduced) with the exception of bottom lobe for off-resonance $\eta = 0.05$. At this donor-surface distance, K_{F} is weakly influenced by the sphere [Figs. 4.6 (d)] and $\tilde{K}_{\mathrm{D}}$ nearly reaches 1, the bulk medium limit (Fig. 4.12).

Figure 4.15 displays the contour plots of $\eta(\mathbf{r}_{\mathrm{A}})$ for a silver sphere with radius $a = 7.5$ nm. At a donor-surface distance separation $z_{\mathrm{o}} - a = 2$ nm, by comparing Figs. 4.15(b) and (f) with Figs. 4.14(b) and (f), respectively, there is *not* any appreciable difference between the corresponding efficiency contour lines, even though the particle radius has increased 200%. Also this occurs when Figs. 4.15(c) and (g) are compared with Figs. 4.14(c) and (g) [$z_{\mathrm{o}} - a = 6$ nm]. The reason is that the normalized direct decay rate $\tilde{K}_{\mathrm{D}}$ at these donor positions is nearly equal for both particle sizes $a = 7.5$ nm and 2.5 nm (see Fig. 4.12), thus the high efficiency Förster region [$\eta(\mathbf{r}_{\mathrm{A}}) > 0.5$] is dominated by the direct donor-acceptor interaction. When donor is placed 12 nm away from the sphere, in the on-resonance case, direct decay rate $\tilde{K}_{\mathrm{D}}$ is substantially greater for $a = 7.5$ nm than for $a = 2.5$ nm (Fig. 4.12). By taking into account this and the fact that at this donor position the sphere influence on the Förster energy transfer rate is weak, the efficiency contour line lobes are a bit smaller for $a = 7.5$ nm than for $a = 2.5$ nm [Figs. 4.15(h) and 4.14(h)]. Conversely, in the off-resonance case, the $\tilde{K}_{\mathrm{D}}$ difference for $a = 7.5$ nm and 2.5 nm is not significant and therefore the efficiency contour lines of η of Figs. 4.15(d) and 4.14(d) are similar.

Now I consider the sphere with radius $a = 12.5$ nm. The contour plots of Förster efficiency $\eta(\mathbf{r}_{\mathrm{A}})$ for this size are depicted in Fig. 4.16. It can be noticed

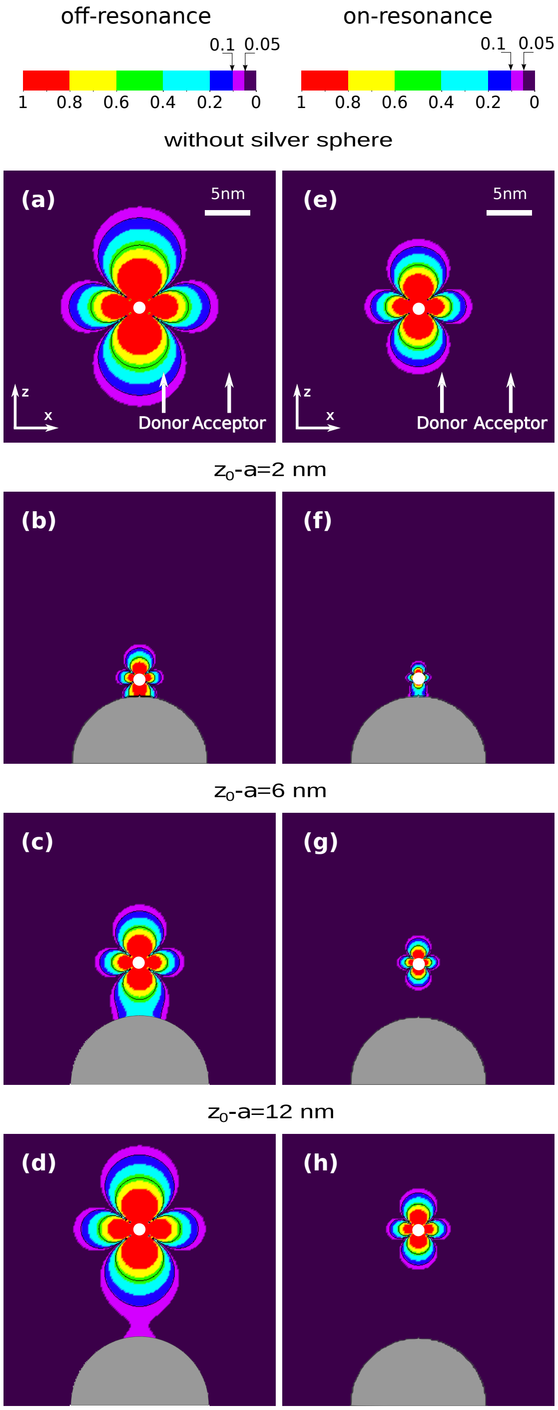

Figure 4.15: Contour plots of $\eta(\mathbf{r}_\mathrm{A})$ ($\mathbf{r}_\mathrm{A}$ belongs to the xz-plane) for $a = 7.5$ nm, and both acceptor and donor dipoles oriented in the z-direction. Off-resonance: (a) without sphere, (b) $z_\mathrm{o} - a = 2$ nm, (c) $z_\mathrm{o} - a = 6$ nm, and (d) $z_\mathrm{o} - a = 12$ nm. On-resonance: (e) without sphere, (f) $z_\mathrm{o} - a = 2$ nm, (g) $z_\mathrm{o} - a = 6$ nm, and (h) $z_\mathrm{o} - a = 12$ nm. Here $z_\mathrm{o} - a$ is the donor-surface separation (the coordinate system origin is placed at the sphere center).

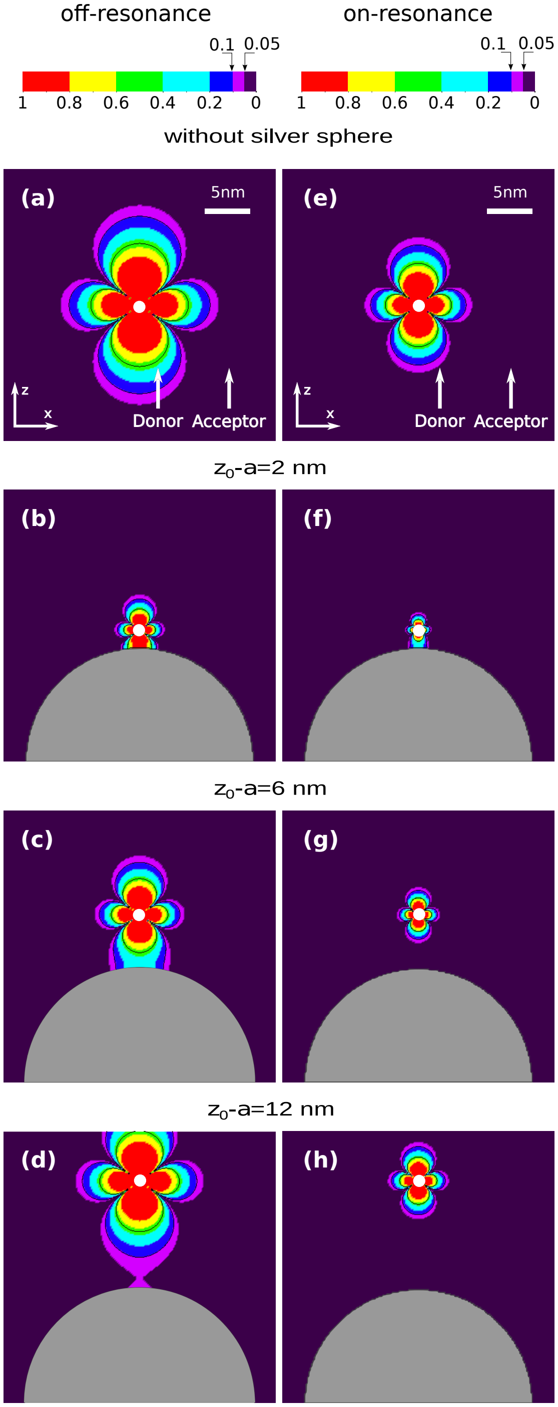

Figure 4.16: Contour plots of $\eta(\mathbf{r}_\mathrm{A})$ ($\mathbf{r}_\mathrm{A}$ belongs to the xz-plane) for $a = 12.5$ nm, and both acceptor and donor dipoles oriented in the z-direction. Off-resonance: (a) without sphere, (b) $z_\mathrm{o} - a = 2$ nm, (c) $z_\mathrm{o} - a = 6$ nm, and (d) $z_\mathrm{o} - a = 12$ nm. On-resonance: (e) without sphere, (f) $z_\mathrm{o} - a = 2$ nm, (g) $z_\mathrm{o} - a = 6$ nm, and (h) $z_\mathrm{o} - a = 12$ nm. Here $z_\mathrm{o} - a$ is the donor-surface separation (the coordinate system origin is placed at the sphere center).

that efficiency contour plots of Fig. 4.16 have not suffered almost no change with respect to the corresponding efficiency contour plots of Fig. 4.15 ($a = 7.5$ nm). The strength of $\tilde{K}_{\rm D}$, at donor positions $z_{\rm o} - a = 2$ nm, 6 nm, and 12 nm, is almost the same for $a = 12.5$ nm and $a = 7.5$ nm, and for both off- and on-resonance cases. Then it follows that the direct donor-acceptor interaction is the strongest contribution in the high Förster efficiency region ($\eta > 0.5$).

4.6.2 x-direction oriented donor and acceptor dipole moments

Now I discuss the case in which the donor and acceptor dipole moments are oriented in the x-direction. In Fig. 4.17, the contour plots of $\eta(\mathbf{r}_{\rm A})$ for $a = 2.5$ nm are illustrated as well as for the bulk medium (without sphere). When the donor is placed a 2 nm distance from the sphere [Figs. 4.17(b) and (f)], the efficiency contour line patterns, analogously as for previous case [Figs. 4.14(b) and (f)], are the shrunk bulk medium efficiency patterns (about a reduction factor of 3), excepting the small lobes of the low efficiency contour lines $\eta = 0.05$ and 0.1 appearing above the sphere for the off-resonance case. For these donor dipole orientation and position, the normalized decay rate $\log \tilde{K}_{\rm D}$ is approximately 2.6 (3.2) for off(on)-resonance [Fig. 4.13]. Although these $\tilde{K}_{\rm D}$-values are smaller than for the z-oriented donor dipole, they are not small enough and hence the reduction of the high Förster efficiency region ($\eta > 0.5$), in which again the direct donor-acceptor interaction dominates. The Förster efficiency lobes $\eta(\mathbf{r}_{\rm A})$, at a donor position 6 nm away from the sphere [Figs. 4.17(c) and (g)], look in shape like for $z_{\rm o} - a = 2.5$ nm, but they are larger [Figs. 4.14(b) and (f)]. Although the Förster radius $R_{\rm o}$ is still smaller than for the bulk. In consideration of Sec. 4.6.1, this effect could have been anticipated since, at this donor position, the normalized direct decay $\log \tilde{K}_{\rm D}$ is approximately 0.8 (1.4) for off-resonance (on-resonance) and consequently the largest field contribution comes from the direct interaction in the high Förster efficiency region [$\eta > 0.5$ or equivalently $\log \tilde{K}_{\rm D} > 0.8$ (1.4)]. When the donor-surface separation is $z_{\rm o} - a = 12$ nm, the normalized direct donor

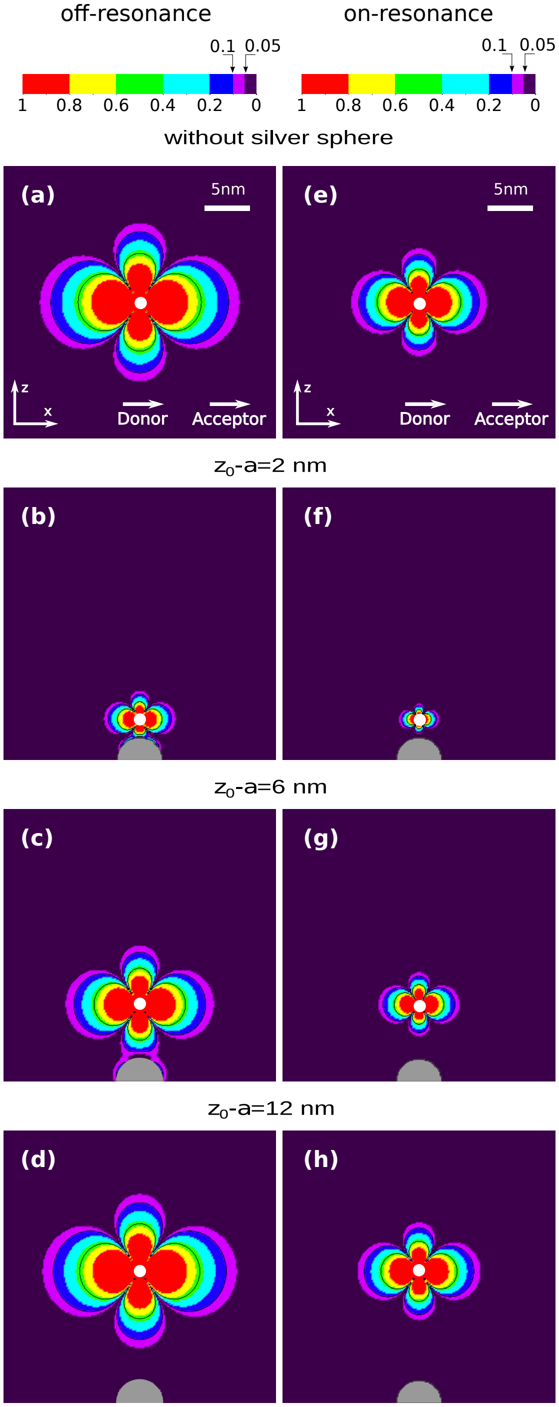

Figure 4.17: Contour plots of $\eta(\mathbf{r}_\mathrm{A})$ ($\mathbf{r}_\mathrm{A}$ belongs to the xz-plane) for $a = 2.5$ nm, and both acceptor and donor dipoles oriented in the x-direction. Off-resonance: (a) without sphere, (b) $z_\mathrm{o} - a = 2$ nm, (c) $z_\mathrm{o} - a = 6$ nm, and (d) $z_\mathrm{o} - a = 12$ nm. On-resonance: (e) without sphere, (f) $z_\mathrm{o} - a = 2$ nm, (g) $z_\mathrm{o} - a = 6$ nm, and (h) $z_\mathrm{o} - a = 12$ nm. Here $z_\mathrm{o} - a$ is the donor-surface separation (the coordinate system origin is placed at the sphere center).

decay rate $\tilde{K}_{\mathrm{D}}$ is close to 1, but the field scattered by the sphere is very weak so the efficiency contour plots of $\eta(\mathbf{r}_{\mathrm{A}})$ almost recapture the shape and dimension of the corresponding bulk plots.

Figure 4.18 shows the contour plots of $\eta(\mathbf{r}_{\mathrm{A}})$ for a sphere with radius $a = 7.5$ nm. Again the contour plots for the bulk medium are depicted at top. At the donor-surface separation $z_{\mathrm{o}} - a = 2$ nm [Figs. 4.18(b) and (f)], the contour plots of η look nearly equal as those for $a = 2.5$ nm [Figs. 4.17(b) and (f)]. The only difference is that lobes of $\eta = 0.05, 0.1$ appearing nearby the sphere in Fig. 4.17(b) are absent for $a = 7.5$ nm. This is explained by the fact that, in this region, K_{F} is larger for a sphere with radius $a = 2.5$ nm than for a sphere with $a = 7.5$ nm [see Fig. 4.9(b) and Fig. 4.10(b)]. This is attributed to $\tilde{K}_{\mathrm{D}}$, at this donor-surface separation, is the same for $a = 2.5$ nm as for $a = 7.5$ nm. As the donor is moved to a 6 nm distance away from the sphere, in the off-resonance case, $\tilde{K}_{\mathrm{D}}$ is still the same for $a = 2.5$ nm as for $a = 7.5$ nm, whereas, in the on-resonance case, $\tilde{K}_{\mathrm{D}}$ is larger for $a = 7.5$ nm than for $a = 2.5$ nm. As a consequence, the off-resonance contour plot of Fig. 4.18(c) is alike to Fig. 4.17(c) [excluding the low efficiency lobes $\eta = 0.05, 0.1$ beside the smaller sphere], while the on-resonance efficiency patterns of Fig. 4.18(g) are smaller than those of Fig. 4.17(g). In Fig. 4.18(d) [off-resonance and donor-surface distance $z_{\mathrm{o}} - a = 12$ nm], the efficiency contour lobes retake already the bulk medium limit. However, on-resonance and at this donor position, these efficiency contour lobes are still smaller than the bulk medium [Fig. 4.18(h)], due to $\log \tilde{K}_{\mathrm{D}} \approx 1$.

The contour plots of $\eta(\mathbf{r}_{\mathrm{A}})$ for a sphere with radius $a = 12.5$ nm are displayed in Fig. 4.19. In this case, there is no difference between the efficiency contour plots of this figure and their corresponding plots of Fig. 4.18 [$a = 7.5$ nm]. This is due to the curves of $\tilde{K}_{\mathrm{D}}(z_{\mathrm{o}} - a)$ for $a = 12.5$ nm and 7.5 nm are almost equal (see Fig. 4.13). Again the direct donor-acceptor interaction is responsible in the high Förster efficiency region ($\eta > 0.5$).

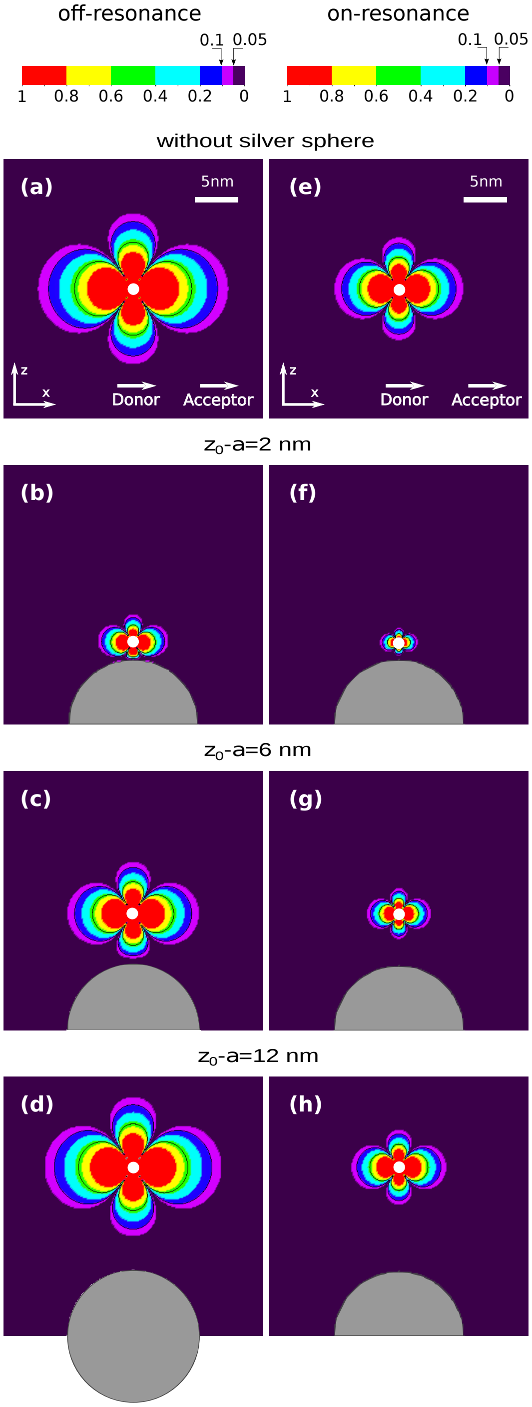

Figure 4.18: Contour plots of $\eta(\mathbf{r}_\mathrm{A})$ ($\mathbf{r}_\mathrm{A}$ belongs to the xz-plane) for $a = 7.5$ nm, and both acceptor and donor dipoles oriented in the x-direction. Off-resonance: (a) without sphere, (b) $z_\mathrm{o} - a = 2$ nm, (c) $z_\mathrm{o} - a = 6$ nm, and (d) $z_\mathrm{o} - a = 12$ nm. On-resonance: (e) without sphere, (f) $z_\mathrm{o} - a = 2$ nm, (g) $z_\mathrm{o} - a = 6$ nm, and (h) $z_\mathrm{o} - a = 12$ nm. Here $z_\mathrm{o} - a$ is the donor-surface separation (the coordinate system origin is placed at the sphere center).

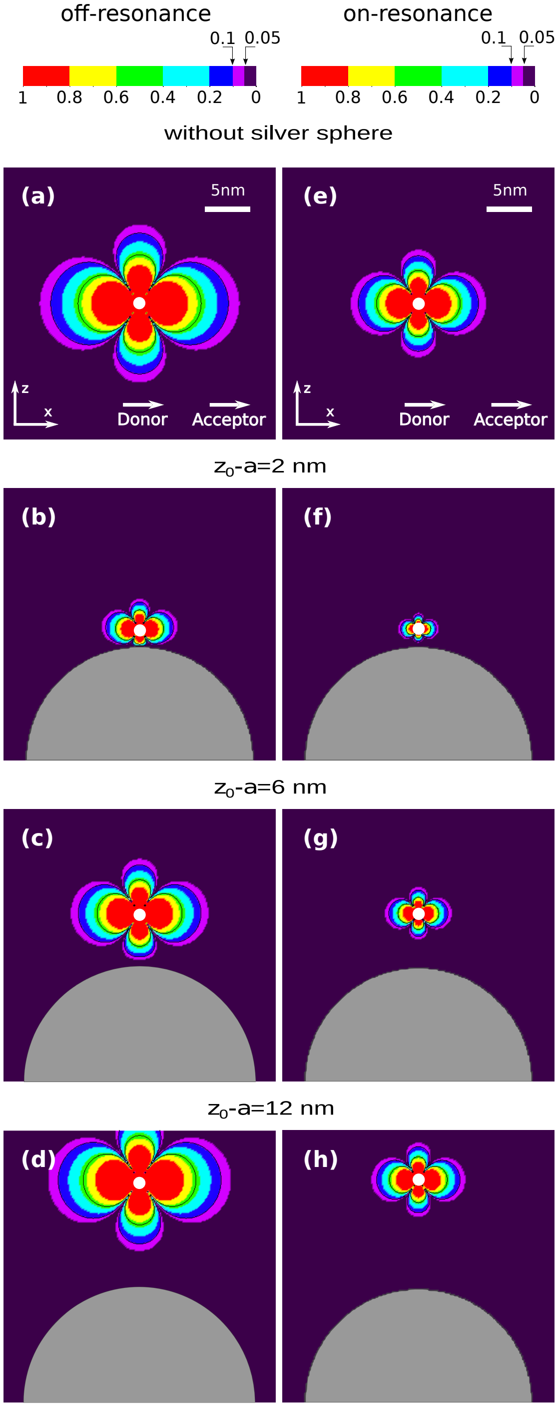

Figure 4.19: Contour plots of $\eta(\mathbf{r}_\mathrm{A})$ ($\mathbf{r}_\mathrm{A}$ belongs to the xz-plane) for $a = 12.5$ nm, and both acceptor and donor dipoles oriented in the x-direction. Off-resonance: (a) without sphere, (b) $z_\mathrm{o} - a = 2$ nm, (c) $z_\mathrm{o} - a = 6$ nm, and (d) $z_\mathrm{o} - a = 12$ nm. On-resonance: (e) without sphere, (f) $z_\mathrm{o} - a = 2$ nm, (g) $z_\mathrm{o} - a = 6$ nm, and (h) $z_\mathrm{o} - a = 12$ nm. Here $z_\mathrm{o} - a$ is the donor-surface separation (the coordinate system origin is placed at the sphere center).

4.6.3 Additional remarks

As mentioned, the experimental works [26, 27] report efficiency enhancement of Förster energy transfer (obtained from acceptor fluorescence measurements) due to the presence of the nanosphere and this efficiency increases as the particle size increases. These results are not in accordance with the results obtained herein. In these experiments, the Cy5-Cy5.5 pair is used (the same chosen donor-acceptor pair in my thesis) and the donor is excited with a wavelength $\lambda_{\mathrm{o}} = 635$ nm light. As seen in Fig. 4.1, the external beam not only excites the donor but also the acceptor. Hence, this establishes an additional channel for acceptor excitation. The excitation rate γ_{ex} through this channel is proportional to the external excitation field intensity at the acceptor position. This excitation rate γ_{ex} is even larger in presence of the sphere than without the sphere because of the field enhancement due to the nanoparticle. As a consequence of the added acceptor excitation channel, the fluorescence rate of the light coming out from the acceptor cannot be solely attributed to the energy Förster transfer. This might explain why these experimental results differ with the theoretical outcomes of my thesis. Alike as Refs. [26, 27], efficiency enhancement of Förster energy transfer nearby a metallic particle were reported in Refs. [29, 30] (measurements were performed with an ensemble of donor and acceptor molecules). With the information contain therein, I was not able to extract a plausible cause why these experimental results are not in agreement with my numerical simulations.

On the contrary, the experimental article [28], obtaining a reduction of the Förster process occurrence likelihood nearby nanodisks, assures that the exciting donor light beam does not interact with the acceptor. In this case, the experimental outcomes of this article coincide qualitatively with my numerical results described in this Section. In the experimental study [31], the acceptor was only excited via Förster energy transfer and likewise as in Ref. [28], the observed effects of this study (Förster energy transfer rate enhancement and efficiency reduction for a donor-acceptor pair with a ~ 3.8 nm intermolecular separation) are consistent with my results.

In the experimental paper [32], the Förster energy transfer rate between quantum dots [donor (acceptor) diameter ~ 2.5 nm (~ 3.3 nm)] placed on the opposite sides ($|\mathbf{r}_\mathrm{D} - \mathbf{r}_\mathrm{A}| =$ 23.4 nm) of a gold sphere ($a =$ 2.75 nm) is enhanced by a factor ~ 80 and the Förster efficiency increases from $\sim 0.12\%$ (without sphere) to $\sim 8\%$ (with sphere). As discussed in Sec. 4.4, the dipole moments for quantum dots are about one order of magnitude larger than for molecules (even higher order multipole transitions in quantum dots might be needed [74]). Since $\tilde{K}_\mathrm{F}(\mathbf{r}_\mathrm{A}) \propto |\boldsymbol{\mu}_\mathrm{A}|^2$, it might be expected that, at a certain acceptor position, $\tilde{K}_\mathrm{F}$ for quantum dots becomes much larger than for molecules. Hence, according to Eq. (4.10), the efficiency could be improved. Although, a more detailed theoretical analysis is required to determine whether this efficiency enhancement can be attained with quantum dots nearby metallic nanoparticles.

Chapter 5

Conclusions

I explored extensively the Förster energy transfer rate K_{F} as a function of the acceptor position in the vicinity of a *silver* nano-sphere for several: donor positions, particle radii, and orientations of the acceptor and donor dipole moments. In addition, I studied the influence of the excitation of surface plasmons on the Förster energy transfer rate K_{F}. Hence, I considered two particular donor-acceptor pairs of fluorophores: Cy5-Cy5.5 (Lysotracker$^{\mathrm{TM}}$ Blue-F2N12S) whose emission-absorption spectral overlap lies outside (inside) of the spectral range of the plasmonic resonant frequencies. I also investigated the Förster efficiency η as a function of the acceptor position in the vicinity of a silver nano-sphere with the same degree of depth as the Förster energy transfer rate K_{F}. I recall that since the donor can be de-excited through two pathways: (1) Förster energy transfer and (2) donor direct decay, there is a competition between these de-excitation processes; the likelihood of occurrence of the Förster energy transfer process can be quantified by the efficiency $\eta \equiv K_{\mathrm{F}}/(K_{\mathrm{F}}+K_{\mathrm{D}})$ [K_{D} direct donor decay rate]. As a consequence K_{D} is necessary for obtaining η, thus I calculated K_{D} against the donor position for several: particle radii and orientations of the donor dipole. I assumed that the dielectric response of the sphere is modified due to the nanoscale confinement of the free-electrons of the metal and the interaction of these electrons with the surface atoms of the background medium. As a result of these effects, the dielectric response is described by the Drude model with a size dependent collision rate parameter. The electric field arising from a dipole (donor) and interacting with the acceptor was obtained from the quasi-static approach. This approach was justified from the fact that the donor-acceptor interaction nearby the nanoparticle occur within a volume much less than λ^3 (optical wavelength).

Particularly, I considered spherical particles with radii $a = 2.5$ nm, 7.5 nm and 12.5 nm and donor-surface distances $z_{\rm o} - a = 2$ nm, 6 nm and 12 nm. The high-value contour lines of $\log \tilde{K}_{\rm F}({\rm r_A}) = 1, 2, 3$ (reminding that $\tilde{K}_{\rm F}$ is the normalized Förster energy transfer rate $K_{\rm F}$ with respect to the direct donor decay without sphere $K_{\rm D0}$) turned out to be practically unperturbed by the presence of the sphere. This follows from the fact that, in the region (nearby the donor, $\lesssim 3$ nm) enclosed by these contour lines, the electric field originating from the direct donor-acceptor interaction pathway is stronger than the field by scattered the sphere. On the contrary, in comparison with the background medium, the low-value contour curves $\log \tilde{K}_{\rm F}({\rm r_A}) = -3, -2, -1, 0$ are strongly distorted and resized with the presence of the sphere. This is consequence of the interference between the direct and scattering electric fields. When the donor is 2 nm separated from the sphere surface, these contour lines become more distorted and this distortion is more notorious for on-resonance case (excitation of surface plasmons that leads to enhancement of the scattering field) than for off-resonance case and for larger particle sizes (particle radii $a = 7.5$ nm and 12.5 nm). Also, the shape of the contour lines $\log \tilde{K}_{\rm F} = -3, -2, -1, 0$ depends on the orientations of both donor and acceptor dipole moments. For donor and acceptor dipoles oriented in the z-direction and donor-surface distance equal to 2 nm, the contour lines $\log \tilde{K}_{\rm F} = -3, -2, -1, 0$ are enlarged with respect to the background medium; in the case of x-oriented donor and acceptor dipoles and the same donor separation, this enlargement effect is observed only for the on-resonance case and larger sphere sizes (particle radii $a = 7.5$ nm and 12.5 nm). As the donor-surface distance increases to $z_{\rm o} - a = 7.5$ nm and 12 nm, the lobes of

$\log\tilde{K}_{\rm F} = -3,-2,-1,0$ above the donor shrink, and the lobes of $\log\tilde{K}_{\rm F} = -3,-2$ below the donor become perturbed around the sphere by the scattering field. These lobes perturbations are more remarkable for the z-oriented donor and acceptor dipoles than for the x-oriented molecular dipoles. When the donor is placed at a distance 12 nm away from the sphere surface, the contour plots of $\log\tilde{K}_{\rm F}(\rm r_A)$ almost retake those for the background medium with the exception of the bottom lobes beside the sphere for the contour line $\log\tilde{K} = -3,-2$. In summary, high-value contour lines $\log\tilde{K}_{\rm F} \geq 1$ are practically unchanged with the particle presence, whereas the low-value contour lines $\log\tilde{K}_{\rm F} = -3,-2,-1,0$ are perturbed by the presence of the sphere and they depend on the donor position, orientations of the donor and acceptor dipoles, and whether surface plasmons are excited.

I calculated the enhancement factor of the Förster energy rate with sphere with respect to the background medium, namely, $K_{\rm F}(\rm r_A)/K_{\rm F0}(\rm r_A)$ at a few particular acceptor positions for a particle with radius $a = 2.5$ nm, donor-surface distance $z_{\rm o} - a = 2$ nm and z-oriented molecular dipoles. In agreement with Refs. [20,21], the largest enhancement factors of $K_{\rm F}/K_{\rm F0}$ occurred when donor and acceptor are placed on opposite sides of the sphere. At these donor-acceptor locations, $K_{\rm F}/K_{\rm F0}$ is greater for on-resonance than for off-resonance. From the contour plots of $\tilde{K}_{\rm F}(\rm r_A)$, it can be inferred that a larger particle size can yield an even larger $K_{\rm F}/K_{\rm F0}$ enhancement. I emphasize that an enhancement of $K_{\rm F}/K_{\rm F0}$ does not necessarily mean an increase of occurrence probability of the Förster process. The results of Secs. 4.4, 4.5 and 4.6 show that the donor direct decay is more probable than the Förster energy transfer (low Förster efficiency η, $K_{\rm D} > K_{\rm F}$) when a large $K_{\rm F}/K_{\rm F0}$ enhancement factor occur.

In presence of the sphere, the high Förster efficiency region contour lines ($\eta > 0.5$) have the same shape as the bulk, but their lengths are reduced. This translates into a reduction of the Förster radius $R_{\rm o}$ that depends strongly on the donor location as a consequence of the large enhancement of the donor decay (in comparison with the case without sphere) as the donor approaches to the sphere. Moreover, in the Förster high efficiency region ($\eta > 0.5$), the direct donor-acceptor electromagnetic interaction pathway dominates, and the particle size and the plasmonic excitation do not have a significant impact.

I discussed how my theoretical outcomes compare with the results of several experiments of Förster energy transfer in the vicinity of metallic nanoparticles. In fact, in presence of the nanoparticle, some of these experiments found improvement of Förster efficiency and others efficiency reduction. The experiments that report Förster efficiency enhancement are not in accordance with my numerical outcomes. In some of these experiments, I addressed that a possible reason explaining the Förster enhancement efficiency is the unwanted excitation of the acceptor by the external donor pump light which might perturb the acceptor fluorescent measurements. Also in another experiment with quantum dots, the Förster efficiency was enhanced with the presence of the sphere. Presumably this effect can be attributed to the fact that the Förster energy transfer rate between a quantum dot pair could be larger than between a molecular pair and therefore an improvement of the Förster efficiency could be attained. The increase of Förster energy transfer rate is because the dipole moment strength for quantum dots is larger than for molecules. On the other hand, experiments that ensure only acceptor excitation via Förster transfer energy mechanism rendered a reduction of the Förster efficiency. The results of these experiments are in qualitative accordance with my theoretical outcomes.

As mentioned the Förster transfer energy process is implemented for detecting real-time nanometric displacements of proteins. The size of the largest spatial step that can be resolved with this technique is about the Förster radius R_{o}. As seen the presence of the metallic sphere reduces the Förster radius R_{o}. Therefore, the inclusion of a metallic sphere can be used as a controlling device for reducing the Förster radius R_{o}, thus decrease of the size of largest resolvable spatial step. Therefore, the influence of the nanoparticle on the Förster energy transfer can be exploited for extending the current capabilities of this technique.

Appendix A

Green tensor and power released (absorbed) by a dipole (polarizable particle)

A.1 Green tensor

The frequency domain Maxwell equations in a linear, isotropic, inhomogeneous [$\epsilon(\mathbf{r},\omega)$], and nonmagnetic medium ($\mu = 1$) are

$$\begin{aligned}
\nabla \times \mathbf{E}(\mathbf{r},\omega) &= i\omega\mu_{\mathrm{o}}\mathbf{H}(\mathbf{r},\omega), & \text{(A.1)}\\
\nabla \times \mathbf{H}(\mathbf{r},\omega) &= -i\omega\epsilon_{\mathrm{o}}\epsilon(\mathbf{r},\omega)\mathbf{E}(\mathbf{r},\omega) + \mathbf{j}(\mathbf{r},\omega), & \text{(A.2)}\\
\nabla \cdot \mathbf{D}(\mathbf{r},\omega) &= \rho(\mathbf{r},\omega), & \text{(A.3)}\\
\nabla \cdot \mathbf{B}(\mathbf{r},\omega) &= 0. & \text{(A.4)}
\end{aligned}$$

Here, $\mathbf{E}(\mathbf{r},\omega)$ is the electric field, $\mathbf{D}(\mathbf{r},\omega) = \epsilon_{\mathrm{o}}\epsilon(\mathbf{r},\omega)\mathbf{E}(\mathbf{r},\omega)$ is the electric displacement, $\mathbf{H}(\mathbf{r},\omega)$ is the magnetic field, $\mathbf{B}(\mathbf{r},\omega)$ is the magnetic induction, $\mathbf{j}(\mathbf{r},\omega)$ is the external current density, and $\rho(\mathbf{r},\omega)$ is the external charge density. From these equations, the electric field $\mathbf{E}(\mathbf{r},\omega)$ fulfills the wave equation with sources

$$\nabla \times \nabla \times \mathbf{E}(\mathbf{r},\omega) - k_{\mathrm{o}}^2 \epsilon(\mathbf{r},\omega)\mathbf{E}(\mathbf{r},\omega) = i\omega\mu_{\mathrm{o}}\mathbf{j}(\mathbf{r},\omega), \tag{A.5}$$

where $k_{\mathrm{o}}^2 = \omega^2/c^2$. The solution of Eq. (A.5) can be obtained from the Green tensor as

$$\mathbf{E}(\mathbf{r},\omega) = i\omega\mu_{\mathrm{o}} \int_V \overleftrightarrow{\mathbf{G}}(\mathbf{r},\mathbf{r}',\omega)\cdot\mathbf{j}(\mathbf{r}',\omega)\,\mathrm{d}^3\mathbf{r}', \tag{A.6}$$

where the Green tensor satisfies

$$\nabla \times \nabla \times \overleftrightarrow{\mathbf{G}}(\mathbf{r},\mathbf{r}',\omega) - k_{\mathrm{o}}^2 \epsilon(\mathbf{r},\omega)\overleftrightarrow{\mathbf{G}}(\mathbf{r},\mathbf{r}',\omega) = \overleftrightarrow{\mathbf{I}}\,\delta(\mathbf{r}-\mathbf{r}'). \tag{A.7}$$

Here, $\overleftrightarrow{\mathbf{I}}$ is the unit dyad. Notice that $\overleftrightarrow{\mathbf{G}}(\mathbf{r},\mathbf{r}',\omega)$ depends on the environment in which the sources are embedded.

For the case of a point dipole $\boldsymbol{\mu}$ located at $\mathbf{r}_{\mathrm{o}}$, the density current is

$$\mathbf{j}(\mathbf{r},\omega) = -i\omega\boldsymbol{\mu}\delta\left(\mathbf{r}-\mathbf{r}_{\mathrm{o}}\right). \tag{A.8}$$

It follows straightforwardly from Eq.(A.6) that the electric field generated by this dipole current is

$$\mathbf{E}(\mathbf{r},\omega) = \frac{k_{\mathrm{o}}^2}{\epsilon_{\mathrm{o}}}\overleftrightarrow{\mathbf{G}}(\mathbf{r},\mathbf{r}_{\mathrm{o}},\omega)\cdot\boldsymbol{\mu}, \tag{A.9}$$

where I used the fact that $\mu_{\mathrm{o}} = 1/(c^2\epsilon_{\mathrm{o}})$. According to Eq. (A.9), physically, the Green tensor is the electromagnetic response of the environment to a point dipole $\boldsymbol{\mu}$.

A.1.1 Green tensor in an unbounded medium

In an unbounded medium with dielectric constant ϵ_{m}, the Green tensor in Cartesian coordinates can be written as [56]

$$\overleftrightarrow{\mathbf{G}}_0(\mathbf{r},\mathbf{r}';\omega) = \frac{\exp(ikR)}{4\pi R}\left[\left(1+\frac{ikR-1}{k^2R^2}\right)\overleftrightarrow{\mathbf{I}} + \frac{3-3ikR-k^2R^2}{k^2R^2}\frac{\mathbf{RR}}{R^2}\right], \tag{A.10}$$

where $k = (\omega/c)\sqrt{\epsilon_{\mathrm{m}}}$, $\mathbf{R} = \mathbf{r} - \mathbf{r}'$ and $R = |\mathbf{R}|$.

A.2 Power released (absorbed) by a dipole (polarizable particle)

A.2.1 Power released by a point dipole

The average power released by a harmonically oscillating dipole (angular frequency ω) is obtained from [56]

$$P = -\frac{1}{2}\int_V \mathrm{Re}[\mathbf{j}^*(\mathbf{r}) \cdot \mathbf{E}(\mathbf{r})]\, \mathrm{d}^3\mathbf{r}. \tag{A.11}$$

Equivalently, P is the average work per unit of time done by the current density $\mathbf{j}$ on the electric field. The current density $\mathbf{j}$ for a point dipole, located at $\mathbf{r}_{\mathrm{o}}$, is given by Eq. (A.8) and the electric field $\mathbf{E}$ generated by this current is calculated from Eq. (A.9). By substituting Eq. (A.8) into Eq. (A.11), the average power released by the point dipole becomes

$$P = -\frac{\omega}{2}\int_V \mathrm{Re}[i\boldsymbol{\mu}^*\delta(\mathbf{r} - \mathbf{r}_{\mathrm{o}}) \cdot \mathbf{E}(\mathbf{r})]\, \mathrm{d}^3\mathbf{r} = \frac{\omega}{2}\mathrm{Im}[\boldsymbol{\mu}^* \cdot \mathbf{E}(\mathbf{r}_{\mathrm{o}})]. \tag{A.12}$$

Notice that $\mathbf{E}(\mathbf{r}_{\mathrm{o}})$ is the field created by the dipole at its own position. Finally, the substitution of Eq. (A.9) into Eq. (A.12) renders

$$P = \frac{\omega^3|\boldsymbol{\mu}|^2}{2c^2\varepsilon_{\mathrm{o}}}\mathrm{Im}[\mathbf{n}_\mu \cdot \overleftrightarrow{\mathbf{G}}(\mathbf{r}_{\mathrm{o}}, \mathbf{r}_{\mathrm{o}}, \omega) \cdot \mathbf{n}_\mu]. \tag{A.13}$$

where $\mathbf{n}_\mu$ is a unit vector in the direction of the dipole moment $\boldsymbol{\mu}$.

A.2.2 Power absorbed by a polarizable particle

Let us consider an external harmonically oscillating electric field $\mathbf{E}(\mathbf{r})$ interacting with a polarizable particle (located at $\mathbf{r}_{\mathrm{o}}$). As a result of this interaction, the electric field $\mathbf{E}(\mathbf{r})$ induces a dipole (if the wavelength is larger than the particle size). The strength of this induced dipole is

$$\boldsymbol{\mu} = \overleftrightarrow{\boldsymbol{\alpha}}(\omega) \cdot \mathbf{E}(\mathbf{r}_{\mathrm{o}}) = [\alpha(\omega)\mathbf{n}_{\mu}\mathbf{n}_{\mu}] \cdot \mathbf{E}(\mathbf{r}_{\mathrm{o}}), \tag{A.14}$$

where $\overleftrightarrow{\boldsymbol{\alpha}}$ is the polarizability tensor. Equation (A.14) assumes particularly that the electric field can only induce a dipole moment along the unit vector $\mathbf{n}_{\mu}$. Then, the average power absorbed by the polarizable particle is obtained from

$$P_{\mathrm{a}} = \frac{1}{2}\int_{V} \mathrm{Re}[\mathbf{j}^{*}(\mathbf{r}) \cdot \mathbf{E}(\mathbf{r})]\, \mathrm{d}^{3}\mathbf{r}. \tag{A.15}$$

Although, at first instance, Eq. (A.15) looks similar to Eq. (A.11), there are differences. In this case, $\mathbf{j}$ is an induced current, $\mathbf{E}$ is an external field. Now P_{a} can be seen as the average work per unit of time done by the electric field **E** on the polarizable particle, thus there is a negative sign difference between Eqs. (A.15) and (A.11). By subtituting Eq. (A.8) into Eq. (A.15), it follows straightforwadly that

$$P_{\mathrm{a}} = -\frac{\omega}{2}\mathrm{Im}[\boldsymbol{\mu}^{*} \cdot \mathbf{E}(\mathbf{r}_{\mathrm{o}})]. \tag{A.16}$$

At last by placing Eq. (A.14) into Eq. (A.16), the average power absorbed turns out to be

$$P_{\mathrm{a}} = \frac{\omega}{2}\mathrm{Im}[\alpha(\omega)]|\mathbf{n}_{\mu} \cdot \mathbf{E}(\mathbf{r}_{\mathrm{o}})|^{2}. \tag{A.17}$$

Appendix B

Potential created by a dipole in the vicinity of a sphere

In this appendix, I derive the electric potential $\Phi(\mathbf{r})$ created by a point dipole nearby a sphere from the electric potential $\Phi^{\mathrm{e}}(\mathbf{r})$ created by a point charge outside the sphere.

B.1 Point charge potential

I use the same geometry of Fig. (3.1) where a point charge q is located at $\mathbf{r}_{\mathrm{D}} = z_{\mathrm{o}}\mathbf{n}_z$ ($z_{\mathrm{o}} > a$). By considering the same arguments mentioned in Sec. 3.1, the potential $\Phi^{\mathrm{e}}(\mathbf{r})$ can be expressed as

$$\Phi^{\mathrm{e}}(\mathbf{r}) = \begin{cases} \Phi_0^{\mathrm{e}}(\mathbf{r}) + \Phi_1^{\mathrm{e}}(\mathbf{r}), & |\mathbf{r}| > a \\ \Phi_2^{\mathrm{e}}(\mathbf{r}), & |\mathbf{r}| < a \end{cases}, \tag{B.1}$$

where Φ_0^{e} is the electric potential created by the point charge q embedded in an unbounded medium with dielectric constant ϵ_{m} (without sphere), Φ_1^{e} (Φ_2^{e}) is the electric potential outside (inside) the sphere due to the charge redistribution in the sphere (induced by the point charge q).

Now, $\Phi^{\mathrm{e}}(\mathbf{r})$ satisfies the Poisson equation

$$\nabla^2\Phi^{\mathrm{e}}(\mathbf{r}) = -\frac{\rho_{\mathrm{Q}}(\mathbf{r})}{\epsilon_{\mathrm{o}}\epsilon_{\mathrm{m}}}, \tag{B.2}$$

where $\rho_{\mathrm{Q}}(\mathbf{r}) = q\delta(\mathbf{r}-\mathbf{r}_{\mathrm{D}})$ is the charge density of a point charge q.

For spherical geometries, it is convenient to express the potential in a multipolar expansion with respect to a point, say the origin. In this case, the general form is [75]

$$\begin{aligned}\Psi(r,\theta,\phi) = & \sum_{n=0}^{\infty}\sum_{m=0}^{n}\Bigg[\left(b^{\mathrm{e}}_{nm}r^n + \frac{d^{\mathrm{e}}_{nm}}{r^{n+1}}\right)P_n^m(\cos\theta)(\cos m\phi) \\ & + \left(b^{\mathrm{o}}_{nm}r^n + \tfrac{d^{\mathrm{o}}_{nm}}{r^{n+1}}\right)P_n^m(\cos\theta)(\sin m\phi)\Bigg],\end{aligned} \tag{B.3}$$

where b^{e}_{nm}, d^{e}_{nm}, b^{o}_{nm} and d^{o}_{nm} are constants. Each term of the multipolar series satisfies Laplace equation [$\nabla^2\Psi(\mathbf{r}) = 0$]. In my case, the solution of $\Phi^{\mathrm{e}}(\mathbf{r})$ is simplified by the fact that $\Phi^{\mathrm{e}}(\mathbf{r})$ should be independent of the angle ϕ for the charge q placed at the z-axis (if r and θ are kept fixed, then one sees the same geometry for any ϕ). Consequently, the solution of Φ^{e} is reduced to

$$\Phi^{\mathrm{e}}(r,\theta,\phi) = \sum_{n=0}^{\infty}\left(b_n r^n + \frac{d_n}{r^{n+1}}\right)P_n(\cos\theta), \tag{B.4}$$

where $P_n(\cos\theta) = P_n^0(\cos\theta)$, $b_n = b^{\mathrm{e}}_{n0}$ and $d_n = d^{\mathrm{e}}_{n0}$ (all the remaining constants vanish).

The electric potential Φ^{e}_0 is a very well known solution which is given by

$$\Phi^{\mathrm{e}}_0(\mathbf{r}) = \frac{1}{4\pi\epsilon_{\mathrm{o}}\epsilon_{\mathrm{m}}}\frac{q}{|\mathbf{r}-\mathbf{r}_{\mathrm{D}}|}. \tag{B.5}$$

According to Eq. (B.4), the solution $\Phi^{\mathrm{e}}_1(\mathbf{r})$ (outside the sphere) should admit a multipolar expansion as

$$\Phi_1^{\mathrm{e}}(r,\theta,\phi) = \sum_{n=0}^{\infty} \frac{d_n}{r^{n+1}} P_n(\cos\theta), \tag{B.6}$$

The coefficients of terms that are proportional to r^n must vanish, since $\lim_{r\to\infty} \Phi^{\mathrm{e}}(r,\theta,\phi) = 0$. While inside the sphere [see Eq. (B.4)], Φ_2^{e} must have the form

$$\Phi_2^{\mathrm{e}}(r,\theta,\phi) = \sum_{n=0}^{\infty} b_n r^n P_n(\cos\theta), \tag{B.7}$$

I have disregarded the terms that are proportional to $r^{-(n+1)}$ because the potential must be finite at the origin. At this step, I need to find the coefficients b_n and d_n. These coefficients are obtained from the boundary conditions that $\Phi^{\mathrm{e}}(\mathbf{r})$ satisfy at the sphere surface.

Before evaluating the boundary conditions, I have to obtain the multipolar expansion of $\Phi_0^{\mathrm{e}}(\mathbf{r})$ that is valid at the sphere surface. The distance $|\mathbf{r} - \mathbf{r}_{\mathrm{D}}|$ can be expressed as

$$|\mathbf{r} - \mathbf{r}_{\mathrm{D}}| = (r^2 + z_{\mathrm{o}}^2 - 2rz_{\mathrm{o}}\cos\theta)^{1/2}, \tag{B.8}$$

where $r = |\mathbf{r}|$. I recognized that any point r belonging to the sphere fulfills the condition $r < z_{\mathrm{o}}$. Thus, I can write

$$\frac{1}{|\mathbf{r} - \mathbf{r}_{\mathrm{D}}|} = \frac{1}{z_{\mathrm{o}}\left[1 + \left(\frac{r}{z_{\mathrm{o}}}\right)^2 - 2\left(\frac{r}{z_{\mathrm{o}}}\right)\cos\theta\right]^{1/2}}. \tag{B.9}$$

Since $[(r/z_{\mathrm{o}}) < 1]$, I can expand the right hand side of Eq. (B.9) in a converging binomial series as

$$\frac{1}{|\mathbf{r} - \mathbf{r}_{\mathrm{D}}|} = \frac{1}{z_{\mathrm{o}}}\left[1 + \cos\theta\frac{r}{z_{\mathrm{o}}} + \frac{1}{2}\left(3\cos^2\theta - 1\right)\left(\frac{r}{z_{\mathrm{o}}}\right)^2 + \frac{1}{2}(5\cos^3\theta - 3\cos\theta)\left(\frac{r}{z_{\mathrm{o}}}\right)^3 + \cdots\right]. \tag{B.10}$$

It turns out that the multiplicative factors of $(r/z_\mathrm{o})^n$ ($n = 0, 1, 2, \ldots$) are precisely the Legendre polynomials $P_n(\cos\theta)$ [75]. Therefore, the multipolar expansion of $\Phi_0^\mathrm{e}(\mathbf{r})$ becomes

$$\Phi_o^e(r,\theta,\phi) = \frac{q}{4\pi\epsilon_\mathrm{o}\epsilon_\mathrm{m}}\frac{1}{z_\mathrm{o}}\sum_{n=0}^{\infty}\left(\frac{r}{z_\mathrm{o}}\right)^n P_n(\cos\theta), \qquad r < z_\mathrm{o}. \tag{B.11}$$

I remark that the expansion (B.11) is valid when $r < z_\mathrm{o}$.

The boundary conditions for $\Phi^\mathrm{e}(\mathbf{r})$ at the sphere surface demand

$$\begin{aligned} \Phi_0^\mathrm{e}(a,\theta,\phi) + \Phi_1^\mathrm{e}(a,\theta,\phi) &= \Phi_2^\mathrm{e}(a,\theta,\phi), & \text{(B.12)} \\ \epsilon_\mathrm{m}\left\{\frac{\partial}{\partial r}\left[\Phi_0^\mathrm{e}(r,\theta,\phi) + \Phi_1^\mathrm{e}(r,\theta,\phi)\right]\Big|_{r=a}\right\} &= \epsilon_\mathrm{b}\frac{\partial}{\partial r}\Phi_2^\mathrm{e}(r,\theta,\phi)\Big|_{r=a}. & \text{(B.13)} \end{aligned}$$

The first boundary condition (B.12) means that the potential $\Phi^\mathrm{e}(\mathbf{r})$ is continuous at the interface. The second boundary condition (B.13) comes from the continuity of the normal components of the displacement field **D**(**r**) at the interface. These boundary conditions lead to the following equations

$$\begin{aligned} a^n b_n + \frac{1}{a^{n+1}}d_n &= -\frac{1}{4\pi\epsilon_\mathrm{o}\epsilon_\mathrm{m}}\frac{q}{z_\mathrm{o}}\left(\frac{a}{z_\mathrm{o}}\right)^n, & \text{(B.14)} \\ \epsilon_\mathrm{b} n a^{n-1} b_n + \frac{\epsilon_\mathrm{m}(n+1)}{a^{n+2}}d_n &= \frac{n}{4\pi\epsilon_\mathrm{o}}\frac{q}{z_\mathrm{o}}\frac{a^{n-1}}{z_\mathrm{o}^n}. & \text{(B.15)} \end{aligned}$$

By solving this linear system for b_n and d_n, I obtain the solution $\Phi^\mathrm{e}(\mathbf{r})$ created by the point charge q in the presence of the sphere, that is,

$$\Phi^e(\mathbf{r}) = \begin{cases} \dfrac{q}{4\pi\epsilon_\mathrm{o}\epsilon_\mathrm{m}}\dfrac{1}{|\mathbf{r}-\mathbf{r}_\mathrm{D}|} + \dfrac{q}{4\pi\epsilon_\mathrm{o}\epsilon_\mathrm{m}}\displaystyle\sum_{n=0}^{\infty}\frac{n(\epsilon_\mathrm{m}-\epsilon_\mathrm{b})}{n\epsilon_\mathrm{b}+(n+1)\epsilon_\mathrm{m}}\frac{a^{2n+1}}{z_\mathrm{o}^{n+1}}\frac{P_n(\cos\theta)}{r^{n+1}}, & r > a \\ \\ \dfrac{q}{4\pi\epsilon_\mathrm{o}}\displaystyle\sum_{n=0}^{\infty}\frac{2n+1}{n\epsilon_\mathrm{b}+(n+1)\epsilon_\mathrm{m}}\frac{r^n}{z_\mathrm{o}^{n+1}}P_n(\cos\theta), & r < a \end{cases}. \tag{B.16}$$

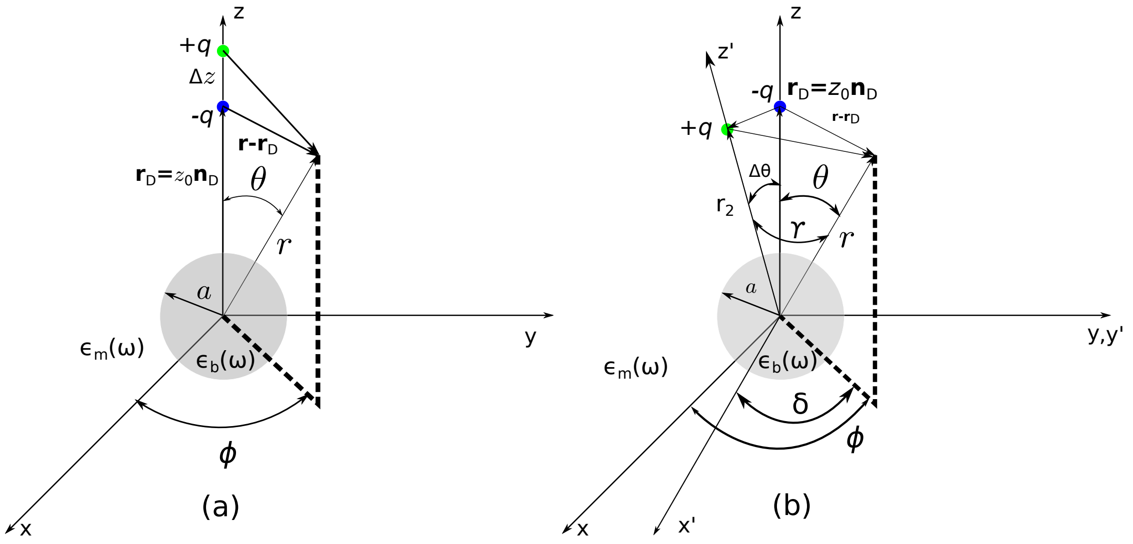

Figure B.1: In this case, an arbitrarily oriented dipole can be represented as the superposition of three dipoles oriented in the (a) z-direction and (b) x-direction

B.2 Point dipole potential

Now, I can derive the potential $\Phi(\mathbf{r})$ created by a point dipole at $\mathbf{r}_{\rm D} = z_{\rm o}\mathbf{n}_z$ in presence of a sphere from the potential $\Phi^{\rm e}(\mathbf{r})$ that was obtained in Sec. B.1. I recall that this is achieved by adding the potential $\Phi^{\rm e}(\mathbf{r})$ due to a point charge $-q$ at $\mathbf{r}_{\rm D} = z_{\rm o}\mathbf{n}_z$ and the potential $\Phi^{\rm e}(\mathbf{r})$ that is originated from a point charge q at $\mathbf{r}_{\rm D} + \Delta s\mathbf{n}_{\rm D}$ ($\boldsymbol{\mu}_{\rm D} = q\Delta s\mathbf{n}_{\rm D}$). Then, the point dipole potential is obtained when the limit $\Delta s \to 0$ is taken in such a way that $q\Delta s$ =constant= $|\boldsymbol{\mu}_{\rm D}|$. According to Eq. (3.4), the total potential $\Phi(\mathbf{r})$ for an arbitrarily oriented dipole $\boldsymbol{\mu}_{\rm D}$ can be decomposed as the superposition of three partial potentials due to the dipoles that are solely oriented along each of the three Cartesian directions.

Dipole oriented in the *z*-direction

For a dipole oriented in the z-direction, the charge $-q$ is located at $z_{\rm o}\mathbf{n}_z$, whereas charge q is placed at $\mathbf{r}_{\rm q}$ =$(z_{\rm o} + \Delta z)\mathbf{n}_z$, thus the dipole moment is $\boldsymbol{\mu}_{\rm D} = q\Delta z\mathbf{n}_z$

[see Fig. B.1 (a)]. The potential produced by $\boldsymbol{\mu}_{\mathrm{D}}$ is

$$\begin{aligned} \Phi_{\mathrm{D}_z}(\mathbf{r}) &= \Phi^{\mathrm{e}}_{\beta_z}(r,\theta,\phi;0,0,z_{\mathrm{o}}+\Delta z) - \Phi^{\mathrm{e}}_{\beta_z}(r,\theta,\phi;0,0,z_{\mathrm{o}}) \\ &= q\Delta z \frac{\Phi^{\mathrm{e}}_{\beta_z}(r,\theta,\phi;0,0,z_{\mathrm{o}}+\Delta z) - \Phi^{\mathrm{e}}_{\beta_z}(r,\theta,\phi;0,0,z_{\mathrm{o}})}{q\Delta z}. \end{aligned} \tag{B.17}$$

where $\beta = 0, 1, 2$. Notice that I have added a term in the argument of Φ^{e} that indicates the charge location in Cartesian coordinates. From Eq. (B.17), in the limit $\Delta z \to 0$, the potential originated by a point dipole μ_z ($\mu_z = q\Delta z$) at $\mathbf{r}_{\mathrm{D}} = z_{\mathrm{o}}\mathbf{n}_z$ is

$$\Phi_z(r,\theta,\phi) = \lim_{\Delta z \to 0} \Phi_{\mathrm{D}_z}(r,\theta,\phi) = \frac{\mu_z}{q}\frac{\partial}{\partial z_{\mathrm{o}}}\Phi^{\mathrm{e}}(r,\theta,\phi;z_{\mathrm{o}},0,0). \tag{B.18}$$

Equation (B.18) renders Eqs. (3.8,3.11,3.14).

Dipole oriented in the x-direction

The potential due to a dipole oriented in the $x-$direction is obtained by adding the potentials arising from a charge $-q$ placed at $\mathbf{r}_{\mathrm{D}} = z_{\mathrm{o}}\mathbf{n}_z$ and a charge q located at $\mathbf{r}_{\mathrm{q}} = z_{\mathrm{o}}\sin\Delta\theta\mathbf{n}_x + z_{\mathrm{o}}\cos\Delta\theta\mathbf{n}_z$.

The solution $\Phi^{\mathrm{e}}(\mathbf{r})$ [Eq. (B.16)] considers that the line passing through the charge location and the origin defines the azimuthal axis (z-axis). Therefore, the potential $\Phi^{\mathrm{e}}(\mathbf{r})$ generated by the off-axis charge q at $\mathbf{r}_{\mathrm{q}}$ must be taken with respect to a new reference system (r, γ, δ) in which the azimuthal axis (z'-axis) is the line that intersects the point $\mathbf{r}_{\mathrm{q}}$ and the origin. Since a rotational transformation relates both reference systems, the coordinate r is the same for both systems. The relation between γ and ($\theta, \phi, \Delta\theta$) is established from

$$\cos\gamma = \frac{\mathbf{r}_{\mathrm{q}}\cdot\mathbf{r}}{|\mathbf{r}_{\mathrm{q}}||\mathbf{r}|} = \frac{\mathbf{r}_{\mathrm{q}}\cdot\mathbf{r}}{z_{\mathrm{o}}r} = \sin\theta\cos\phi\sin\Delta\theta + \cos\theta\cos\Delta\theta. \tag{B.19}$$

Strictly speaking, $\Phi^{\mathrm{e}}(\mathbf{r})$ does not depend on δ; thus, the relation between δ and ($\theta, \phi, \Delta\theta$) is not necessary. Therefore, the potential due to this pair of charges is

$$\begin{aligned}\Phi_{\mathrm{D}_x}(\mathbf{r}) &= \Phi^{\mathrm{e}}(r,\gamma(\theta,\phi,\Delta\theta),\delta;0,0,z_{\mathrm{o}}) - \Phi^{\mathrm{e}}(r,\theta,\phi;0,0,z_{\mathrm{o}}) \\ &= qz_{\mathrm{o}}\Delta\theta\left(\frac{1}{qz_{\mathrm{o}}}\right)\left[\frac{\Phi^{\mathrm{e}}(r,\gamma(\theta,\phi,\Delta\theta),\delta;0,0,z_{\mathrm{o}}) - \Phi^{\mathrm{e}}(r,\theta,\phi;0,0,z_{\mathrm{o}})}{\Delta\theta}\right] \quad \text{(B.20)}\end{aligned}$$

I find the point dipole potential generated by a dipole oriented in the x-direction when I apply the limit $\Delta\theta \to 0$ to Eq. (B.20) (keeping $qz_{\mathrm{o}}\Delta\theta$ =constant=μ_x). In this limit, $\gamma \to \theta$, $\delta \to \phi$, and the potential sum becomes a partial derivative with respect to $\Delta\theta$, that is,

$$\Phi_x(r,\theta,\phi) = \lim_{\Delta\theta\to 0}\Phi_{\mathrm{D}_x}(r,\theta,\phi) = \frac{\mu_x}{qz_{\mathrm{o}}}\frac{\partial}{\partial\Delta\theta}\Phi^{\mathrm{e}}[r,\gamma(\theta,\phi,\Delta\theta),\delta;0,0,z_{\mathrm{o}}]\Big|_{\Delta\theta=0}. \quad \text{(B.21)}$$

By using Eq. (B.21) and Eq. (B.16), I obtain the Eqs. (3.6,3.9,3.12).

Dipole oriented in the y-direction

The potential produced by a point dipole oriented in the $y-$direction is obtained in a similar manner as for the dipole oriented in the $x-$direction. Here, the azimuthal axis z' lies in the $zy-$plane, the point charge q is placed at $\mathbf{r}_{\mathrm{q}} = z_{\mathrm{o}}\sin\Delta\theta\mathbf{n}_y + z_{\mathrm{o}}\cos\Delta\theta\mathbf{n}_z$ ($\Delta\theta$ is also the angle between the azimuthal axes z' and z). and the relation between the polar angle γ and the ($\theta,\phi,\Delta\theta$) is now

$$\cos\gamma = \sin\theta\sin\Delta\theta\sin\phi + \cos\theta\cos\Delta\theta. \quad \text{(B.22)}$$

Therefore, the potential Φ can be also obtained from Eq. (B.21), but the polar angle γ is now defined by Eq. (B.22) and μ_x is replaced by μ_y.

Appendix C

Quasi-static Green's tensor

The quasi-static Green tensor elements [Eq. (3.19)] are obtained by using the relation

$$\begin{aligned}\frac{\partial}{\partial x}\Phi_j(r,\theta,\phi) = &\ \sin\theta\cos\phi\frac{\partial}{\partial r}\Phi_j(r,\theta,\phi) + \frac{\cos\theta\cos\phi}{r}\frac{\partial}{\partial\theta}\Phi_j(r,\theta,\phi)\\ &-\frac{\sin\phi}{r\sin\theta}\frac{\partial}{\partial\phi}\Phi_j(r,\theta,\phi),\end{aligned} \tag{C.1}$$

$$\begin{aligned}\frac{\partial}{\partial y}\Phi_j(r,\theta,\phi) = &\ \sin\theta\sin\phi\frac{\partial}{\partial r}\Phi_j(r,\theta,\phi) + \frac{\cos\theta\sin\phi}{r}\frac{\partial}{\partial\theta}\Phi_j(r,\theta,\phi)\\ &-\frac{\cos\phi}{r\sin\theta}\frac{\partial}{\partial\phi}\Phi_j(r,\theta,\phi),\end{aligned} \tag{C.2}$$

$$\frac{\partial}{\partial z}\Phi_j(r,\theta,\phi) = \cos\theta\frac{\partial}{\partial r}\Phi_j(r,\theta,\phi) - \frac{\sin\theta}{r}\frac{\partial}{\partial\theta}\Phi_j(r,\theta,\phi), \tag{C.3}$$

where ($j = x, y, z$). By substituting Eqs. (3.6-3.14) and Eqs. (C.1-C.3) into Eq. (3.18), I can calculate the Green tensor components. Outside the sphere

$$\overleftrightarrow{\mathbf{Q}}_0(\mathbf{r}, z_\mathrm{o}\mathbf{n}_z) = \frac{1}{4\pi\epsilon_\mathrm{o}\epsilon_\mathrm{m}}\frac{1}{R^3}\left[-\overleftrightarrow{\mathbf{I}} + \frac{3\mathbf{R}\mathbf{R}}{R^2}\right], \tag{C.4}$$

where $\mathbf{R} = \mathbf{r} - z_{\mathrm{o}}\mathbf{n}_z$. While the scattering elements of $\overleftrightarrow{\mathbf{Q}}_1$ are

$$\begin{aligned} Q_{1_{xx}}(r,\theta,\phi) &= -\frac{\sin^2\theta\cos^2\phi}{4\pi\epsilon_{\mathrm{o}}\epsilon_{\mathrm{m}}^2}\sum_{n=1}^{\infty}\frac{(n+1)\alpha_n}{z_{\mathrm{o}}^{n+2}}\frac{\Pi_n(\theta)}{r^{n+2}} \\ &\quad+\frac{\cos\theta\cos^2\phi}{4\pi\epsilon_{\mathrm{o}}\epsilon_{\mathrm{m}}^2}\sum_{n=1}^{\infty}\frac{\alpha_n}{z_{\mathrm{o}}^{n+2}}\frac{\tau_n(\theta)}{r^{n+2}}+\frac{\sin^2\phi}{4\pi\epsilon_{\mathrm{o}}\epsilon_{\mathrm{m}}^2}\sum_{n=1}^{\infty}\frac{\alpha_n}{z_{\mathrm{o}}^{n+2}}\frac{\Pi_n(\theta)}{r^{n+2}}, \end{aligned} \tag{C.5}$$

$$\begin{aligned} Q_{1_{xy}}(r,\theta,\phi) &= -\frac{\sin^2\theta\sin 2\phi}{8\pi\epsilon_{\mathrm{o}}\epsilon_{\mathrm{m}}^2}\sum_{n=1}^{\infty}\frac{(n+1)\alpha_n}{z_{\mathrm{o}}^{n+2}}\frac{\Pi_n(\theta)}{r^{n+2}} \\ &\quad+\frac{\cos\theta\sin 2\phi}{8\pi\epsilon_{\mathrm{o}}\epsilon_{\mathrm{m}}^2}\sum_{n=1}^{\infty}\frac{\alpha_n}{z_{\mathrm{o}}^{n+2}}\frac{\tau_n(\theta)}{r^{n+2}}-\frac{\sin 2\phi}{8\pi\epsilon_{\mathrm{o}}\epsilon_{\mathrm{m}}^2}\sum_{n=1}^{\infty}\frac{\alpha_n}{z_{\mathrm{o}}^{n+2}}\frac{\Pi_n(\theta)}{r^{n+2}}, \end{aligned} \tag{C.6}$$

$$\begin{aligned} Q_{1_{xz}}(r,\theta,\phi) &= \frac{\sin\theta\cos\phi}{4\pi\epsilon_{\mathrm{o}}\epsilon_{\mathrm{m}}^2}\sum_{n=1}^{\infty}\frac{(n+1)^2\alpha_n}{z_{\mathrm{o}}^{n+2}}\frac{P_n(\cos\theta)}{r^{n+2}} \\ &\quad+\frac{\sin 2\theta\cos\phi}{8\pi\epsilon_{\mathrm{o}}\epsilon_{\mathrm{m}}^2}\sum_{n=1}^{\infty}\frac{(n+1)\alpha_n}{z_{\mathrm{o}}^{n+2}}\frac{\Pi_n(\theta)}{r^{n+2}}, \end{aligned} \tag{C.7}$$

$$\begin{aligned} Q_{1_{yx}}(r,\theta,\phi) &= -\frac{\sin^2\theta\sin 2\phi}{8\pi\epsilon_{\mathrm{o}}\epsilon_{\mathrm{m}}^2}\sum_{n=1}^{\infty}\frac{(n+1)\alpha_n}{z_{\mathrm{o}}^{n+2}}\frac{\Pi_n(\theta)}{r^{n+2}} \\ &\quad+\frac{\cos\theta\sin 2\phi}{8\pi\epsilon_{\mathrm{o}}\epsilon_{\mathrm{m}}^2}\sum_{n=1}^{\infty}\frac{\alpha_n}{z_{\mathrm{o}}^{n+2}}\frac{\tau_n(\theta)}{r^{n+2}}-\frac{\sin 2\phi}{8\pi\epsilon_{\mathrm{o}}\epsilon_{\mathrm{m}}^2}\sum_{n=1}^{\infty}\frac{\alpha_n}{z_{\mathrm{o}}^{n+2}}\frac{\Pi_n(\theta)}{r^{n+2}}, \end{aligned} \tag{C.8}$$

$$\begin{aligned} Q_{1_{yy}}(r,\theta,\phi) &= -\frac{\sin^2\theta\sin^2\phi}{4\pi\epsilon_{\mathrm{o}}\epsilon_{\mathrm{m}}^2}\sum_{n=1}^{\infty}\frac{(n+1)\alpha_n}{z_{\mathrm{o}}^{n+2}}\frac{\Pi_n(\cos\theta)}{r^{n+2}} \\ &\quad+\frac{\cos\theta\sin^2\phi}{4\pi\epsilon_{\mathrm{o}}\epsilon_{\mathrm{m}}^2}\sum_{n=1}^{\infty}\frac{\alpha_n}{z_{\mathrm{o}}^{n+2}}\frac{\tau_n(\theta)}{r^{n+2}}+\frac{\cos^2\phi}{4\pi\epsilon_{\mathrm{o}}\epsilon_{\mathrm{m}}^2}\sum_{n=1}^{\infty}\frac{\alpha_n}{z_{\mathrm{o}}^{n+2}}\frac{\Pi_n(\theta)}{r^{n+2}}, \end{aligned} \tag{C.9}$$

$$\begin{aligned} Q_{1_{yz}}(r,\theta,\phi) &= \frac{\sin\theta\sin\phi}{4\pi\epsilon_{\mathrm{o}}\epsilon_{\mathrm{m}}^{2}}\sum_{n=1}^{\infty}\frac{(n+1)^{2}\alpha_{n}}{z_{\mathrm{o}}^{n+2}}\frac{P_{n}(\cos\theta)}{r^{n+2}} \\ &\quad+\frac{\sin 2\theta\sin\phi}{8\pi\epsilon_{\mathrm{o}}\epsilon_{\mathrm{m}}^{2}}\sum_{n=1}^{\infty}\frac{(n+1)\alpha_{n}}{z_{\mathrm{o}}^{n+2}}\frac{\Pi_{n}(\theta)}{r^{n+2}}, \end{aligned} \tag{C.10}$$

$$\begin{aligned} Q_{1_{zx}}(r,\theta,\phi) &= -\frac{\sin 2\theta\cos\phi}{8\pi\epsilon_{\mathrm{o}}\epsilon_{\mathrm{m}}^{2}}\sum_{n=1}^{\infty}\frac{(n+1)\alpha_{n}}{z_{\mathrm{o}}^{n+2}}\frac{\Pi_{n}(\theta)}{r^{n+2}} \\ &\quad-\frac{\sin\theta\cos\phi}{4\pi\epsilon_{\mathrm{o}}\epsilon_{\mathrm{m}}^{2}}\sum_{n=1}^{\infty}\frac{\alpha_{n}}{z_{\mathrm{o}}^{n+2}}\frac{\tau_{n}(\theta)}{r^{n+2}}, \end{aligned} \tag{C.11}$$

$$\begin{aligned} Q_{1_{zy}}(r,\theta,\phi) &= -\frac{\sin 2\theta\sin\phi}{8\pi\epsilon_{\mathrm{o}}\epsilon_{\mathrm{m}}^{2}}\sum_{n=1}^{\infty}\frac{(n+1)\alpha_{n}}{z_{\mathrm{o}}^{n+2}}\frac{\Pi_{n}(\theta)}{r^{n+2}} \\ &\quad-\frac{\sin\theta\sin\phi}{4\pi\epsilon_{\mathrm{o}}\epsilon_{\mathrm{m}}^{2}}\sum_{n=1}^{\infty}\frac{\alpha_{n}}{z_{\mathrm{o}}^{n+2}}\frac{\tau_{n}(\theta)}{r^{n+2}}, \end{aligned} \tag{C.12}$$

$$\begin{aligned} Q_{1_{zz}}(r,\theta,\phi) &= \frac{\cos\theta}{4\pi\epsilon_{\mathrm{o}}\epsilon_{\mathrm{m}}^{2}}\sum_{n=1}^{\infty}\frac{(n+1)^{2}\alpha_{n}}{z_{\mathrm{o}}^{n+2}}\frac{P_{n}(\cos\theta)}{r^{n+2}} \\ &\quad-\frac{\sin^{2}\theta}{4\pi\epsilon_{\mathrm{o}}\epsilon_{\mathrm{m}}^{2}}\sum_{n=1}^{\infty}\frac{(n+1)\alpha_{n}}{z_{\mathrm{o}}^{n+2}}\frac{\Pi_{n}(\theta)}{r^{n+2}}. \end{aligned} \tag{C.13}$$

Finally, the quasi-static Green tensor elements inside the sphere turned out to be

$$\begin{aligned} Q_{2_{xx}}(r,\theta,\phi) &= -\frac{\sin^{2}\theta\cos^{2}\phi}{4\pi\epsilon_{\mathrm{o}}}\sum_{n=1}^{\infty}n\gamma_{n}\frac{r^{n-1}}{z_{\mathrm{o}}^{n+2}}\Pi_{n}(\cos\theta)-\frac{\cos\theta\cos^{2}\phi}{4\pi\epsilon_{\mathrm{o}}}\sum_{n=1}^{\infty}\gamma_{n}\frac{r^{n-1}}{z_{\mathrm{o}}^{n+2}}\tau_{n}(\cos\theta) \\ &\quad-\frac{\sin^{2}\phi}{4\pi\epsilon_{\mathrm{o}}}\sum_{n=1}^{\infty}\gamma_{n}\frac{r^{n-1}}{z_{\mathrm{o}}^{n+2}}\Pi_{n}(\cos\theta), \end{aligned} \tag{C.14}$$

$$\begin{aligned} Q_{2_{xy}}(r,\theta,\phi) &= -\frac{\sin^2\theta\sin 2\phi}{8\pi\epsilon_\mathrm{o}}\sum_{n=1}^{\infty} n\gamma_n \frac{r^{n-1}}{z_\mathrm{o}^{n+2}}\Pi_n(\cos\theta) - \frac{\cos\theta\sin 2\phi}{8\pi\epsilon_\mathrm{o}}\sum_{n=1}^{\infty}\gamma_n\frac{r^{n-1}}{z_\mathrm{o}^{n+2}}\tau_n(\cos\theta) \\ &\quad +\frac{\sin 2\phi}{8\pi\epsilon_\mathrm{o}}\sum_{n=1}^{\infty}\gamma_n\frac{r^{n-1}}{z_\mathrm{o}^{n+2}}\Pi_n(\cos\theta), \end{aligned} \tag{C.15}$$

$$\begin{aligned} Q_{2_{xz}}(r,\theta,\phi) &= \frac{\sin\theta\cos\phi}{4\pi\epsilon_\mathrm{o}}\sum_{n=1}^{\infty} n(n+1)\gamma_n \frac{r^{n-1}}{z_\mathrm{o}^{n+2}}P_n(\cos\theta) \\ &\quad -\frac{\sin 2\theta\cos\phi}{8\pi\epsilon_\mathrm{o}}\sum_{n=1}^{\infty}(n+1)\gamma_n\frac{r^{n-1}}{z_\mathrm{o}^{n+2}}\Pi_n(\cos\theta), \end{aligned} \tag{C.16}$$

$$\begin{aligned} Q_{2_{yx}}(r,\theta,\phi) &= -\frac{\sin^2\theta\sin 2\phi}{8\pi\epsilon_\mathrm{o}}\sum_{n=1}^{\infty} n\gamma_n \frac{r^{n-1}}{z_\mathrm{o}^{n+2}}\Pi_n(\cos\theta) - \frac{\cos\theta\sin 2\phi}{8\pi\epsilon_\mathrm{o}}\sum_{n=1}^{\infty}\gamma_n\frac{r^{n-1}}{z_\mathrm{o}^{n+2}}\tau_n(\cos\theta) \\ &\quad +\frac{\sin 2\phi}{8\pi\epsilon_\mathrm{o}}\sum_{n=1}^{\infty}\gamma_n\frac{r^{n-1}}{z_\mathrm{o}^{n+2}}\Pi_n(\cos\theta), \end{aligned} \tag{C.17}$$

$$\begin{aligned} Q_{2_{yy}}(r,\theta,\phi) &= -\frac{\sin^2\theta\sin^2\phi}{4\pi\epsilon_\mathrm{o}}\sum_{n=1}^{\infty} n\gamma_n \frac{r^{n-1}}{z_\mathrm{o}^{n+2}}\Pi_n(\cos\theta) - \frac{\cos\theta\sin^2\phi}{4\pi\epsilon_\mathrm{o}}\sum_{n=1}^{\infty}\gamma_n\frac{r^{n-1}}{z_\mathrm{o}^{n+2}}\tau_n(\cos\theta) \\ &\quad -\frac{\cos^2\phi}{4\pi\epsilon_\mathrm{o}}\sum_{n=1}^{\infty}\gamma_n\frac{r^{n-1}}{z_\mathrm{o}^{n+2}}\Pi_n(\cos\theta), \end{aligned} \tag{C.18}$$

$$\begin{aligned} Q_{2_{yz}}(r,\theta,\phi) &= \frac{\sin\theta\sin\phi}{4\pi\epsilon_\mathrm{o}}\sum_{n=1}^{\infty} n(n+1)\gamma_n \frac{r^{n-1}}{z_\mathrm{o}^{n+2}}P_n(\cos\theta) \\ &\quad -\frac{\sin 2\theta\sin\phi}{8\pi\epsilon_\mathrm{o}}\sum_{n=1}^{\infty}(n+1)\gamma_n\frac{r^{n-1}}{z_\mathrm{o}^{n+2}}\Pi_n(\cos\theta), \end{aligned} \tag{C.19}$$

$$\begin{aligned} Q_{2_{zx}}(r,\theta,\phi) &= -\frac{\sin 2\theta\cos\phi}{8\pi\epsilon_\mathrm{o}}\sum_{n=1}^{\infty} n\gamma_n \frac{r^{n-1}}{z_\mathrm{o}^{n+2}}\Pi_n(\cos\theta) \\ &\quad +\frac{\sin\theta\cos\phi}{4\pi\epsilon_\mathrm{o}}\sum_{n=1}^{\infty}\gamma_n\frac{r^{n-1}}{z_\mathrm{o}^{n+2}}\tau_n(\cos\theta), \end{aligned} \tag{C.20}$$

$$\begin{aligned} Q_{2_{zy}}(r,\theta,\phi) &= -\frac{\sin 2\theta \sin\phi}{8\pi\epsilon_{\mathrm{o}}}\sum_{n=1}^{\infty} n\gamma_n \frac{r^{n-1}}{z_{\mathrm{o}}^{n+2}}\Pi_n(\cos\theta) \\ &\quad +\frac{\sin\theta\sin\phi}{4\pi\epsilon_{\mathrm{o}}}\sum_{n=1}^{\infty}\gamma_n\frac{r^{n-1}}{z_{\mathrm{o}}^{n+2}}\tau_n(\cos\theta), \end{aligned} \tag{C.21}$$

$$\begin{aligned} Q_{2_{zz}}(r,\theta,\phi) &= \frac{\cos\theta}{4\pi\epsilon_{\mathrm{o}}}\sum_{n=1}^{\infty} n(n+1)\gamma_n \frac{r^{n-1}}{z_{\mathrm{o}}^{n+2}}P_n(\cos\theta) \\ &\quad +\frac{\sin^2\theta}{4\pi\epsilon_{\mathrm{o}}}\sum_{n=1}^{\infty}(n+1)\gamma_n\frac{r^{n-1}}{z_{\mathrm{o}}^{n+2}}\Pi_n(\cos\theta). \end{aligned} \tag{C.22}$$

Here, I have defined

$$\Pi_n[\theta] \equiv \frac{P_n^1[\cos\theta]}{\sin\theta}, \tag{C.23}$$

$$\tau_n[\theta] \equiv \frac{\partial}{\partial\theta}P_n^1[\cos\theta], \tag{C.24}$$

$$\gamma_n \equiv \frac{2n+1}{n\epsilon_{\mathrm{b}}+(n+1)\epsilon_{\mathrm{m}}}. \tag{C.25}$$

Appendix D

Determination of f_{D} and Im$[\alpha_{\mathrm{A}}]$

Herein, I describe how f_{D} and Im$[\alpha_{\mathrm{A}}]$ can be extracted from the data provided by the molecular probe companies. I recall that the spectral data $\sigma_{\mathrm{e(a)}}(\lambda_{\mathrm{o}i})$ [the subscript e (a) denotes emission (absorption)] is a discrete function of certain values of the free-space wavelength $\lambda_{\mathrm{o}i}$ $(i = 1, 2, \dots, M)$ in which Max$[\sigma_{\mathrm{e(a)}}(\lambda_{\mathrm{o}i})] = 100$.

According to Eqs. (3.21,3.24), K_{F} and K_{D} are obtained by integrations with respect to ω. However for numerical convenience, I carry out the integration for calculating K_{F} and K_{D} with respect to free-space wavevector k_{o}, thus I apply the variable transformation $k_{\mathrm{o}} = \omega/c$. Consequently, I require that f_{D} and Im$[\alpha]$ should be expressed as a function of k_{o}.

Let us suppose that the $\sigma_{\mathrm{e(a)}}(\lambda_{\mathrm{o}})$ is a continuous function of λ_{o}. First, I express the emission and absorption spectra as a function of k_{o}, that is,

$$\hat{\sigma}_{\mathrm{e(a)}}(k_o) = \frac{2\pi}{k_{\mathrm{o}}^2}\sigma_{\mathrm{e(a)}}(\lambda_o = 2\pi/k_{\mathrm{o}}). \tag{D.1}$$

The factor $2\pi/k_{\mathrm{o}}^2$ on the right hand size of Eq. (D.1) assures

$$\mathcal{N}_{\mathrm{e(a)}} = \int_0^\infty \hat{\sigma}_{\mathrm{e(a)}}(k_{\mathrm{o}})\,\mathrm{d}k_{\mathrm{o}} = \int_0^\infty \sigma_{\mathrm{e(a)}}(\lambda_{\mathrm{o}})\,\mathrm{d}\lambda_{\mathrm{o}}. \tag{D.2}$$

I must consider a normalized donor emission (acceptor absorption) $f_{\mathrm{D(A)}}(k_{\mathrm{o}})$

distribution, namely,

$$\int_0^\infty f_{\rm D(A)}(k_{\rm o})\,{\rm d}k_{\rm o} = 1. \tag{D.3}$$

Then, it follows that

$$f_{\rm D(A)}(k_{\rm o}) \equiv \frac{1}{\mathcal{N}_{{\rm e}(a)}}\hat{\sigma}_{\rm e(a)}(k_{\rm o}). \tag{D.4}$$

I remind that $f_{\rm D}(k_{\rm o})$ is just the normalized donor spectrum that is defined in Eq. (2.10). On the other hand, molecular polarizabilities scale with a factor $|\boldsymbol{\mu}|^2/(\hbar c)$ ($\boldsymbol{\mu}$ is electronic transition dipole moment) [56]. Therefore, I assume that the imaginary part of the acceptor polarizability can be expressed as

$$\text{Im}[\alpha_{\rm A}(k_{\rm o})] = \frac{\pi|\boldsymbol{\mu}_{\rm A}|^2}{\hbar c} f_{\rm A}(k_{\rm o}). \tag{D.5}$$

The discrete data $f_{\rm D(A)}(k_{{\rm o}i})$ ($i = 1, 2, 3, \ldots, M$) are obtained from the original data $\sigma_{\rm e(a)}(\lambda_{{\rm o}i})$ by using Eqs. (D.1,D.2,D.4) [$\mathcal{N}_{\rm e(a)}$ is obtained by numerical integration]. Then, the data $f_{\rm D(A)}(k_{{\rm o}i})$ are fitted by a superposition of Gaussian functions, that is,

$$f_{\rm D(A)}(k_{\rm o}) = \frac{1}{\sqrt{2\pi}\,N}\sum_{n=1}^{N}\frac{1}{\varPsi_n}\exp\left[-\frac{(k_{\rm o}-k_n)^2}{2\varPsi_n^2}\right]. \tag{D.6}$$

Here, N is the number of Gaussian functions (set *a priori*), k_n and $\varPsi_n$ are the central wavevector and the width of the n-th Gaussian function, respectively. The numerical algorithm yields the values k_n and $\varPsi_n$ that minimize the sum of the squared difference of the function original value and its fit value.

The Cy5 (emission), Cy5.5 (absorption), LysoTracker$^{\rm TM}$ Blue (emission), and F2N12S (absorption) original spectral data $[\sigma_{\rm e}(\lambda_{{\rm o}i})]$ are obtained from Ref. [76]. By applying the aforementioned methodology, I obtain the normalized donor emission profiles $f_{\rm D}(k_{\rm o})$ for Cy5 and LysoTracker$^{\rm TM}$ Blue, as well as the acceptor absorption profiles $f_{\rm A}(k_{\rm o})$ for Cy5.5 and F2N12S. The parameters k_n and $\varPsi_n$ that characterize the Gaussian decomposition of these emission and absorption profiles are tabulated in Tables D.1 and D.2, respectively.

Table D.1: Gaussian fit parameters (k_n and Ψ_n) of $f_{\mathrm{D}}(k_{\mathrm{o}})$ for Cy5 and LysoTracker$^{\mathrm{TM}}$ Blue. Here $\bar{k} = 1$ cm^{-1}.

	Cy5		LysoTracker$^{\mathrm{TM}}$ Blue	
n	$k_n/\bar{k}$	$\Psi_n/\bar{k}$	$k_n/\bar{k}$	$\Psi_n/\bar{k}$
1	$91\,258$	$4\,767$	$139\,915$	$6\,901$
2	$93\,657$	$1\,964$	$139\,973$	$15\,697$
3	$94\,738$	$1\,691$	$141\,538$	$3\,240$
4			$147\,528$	$1\,956$
5			$150\,369$	$1\,961$
6			$155\,149$	$2\,247$
7			$158\,275$	$2\,021$

Table D.2: Gaussian fit parameters (k_n and Ψ_n) of $f_{\mathrm{A}}(k_{\mathrm{o}})$ for Cy5.5 and F2N12S. Here $\bar{k} = 1$ cm^{-1}.

	Cy5.5		F2N12S	
n	$k_n/\bar{k}$	$\Psi_n/\bar{k}$	$k_n/\bar{k}$	$\Psi_n/\bar{k}$
1	$92\,617$	$1\,506$	$147\,173$	$7\,374$
2	$93\,375$	$2\,637$	$155\,187$	$11\,257$
3	$94\,252$	$2\,044$		
4	$100\,174$	$2\,889$		
5	$103\,280$	$6\,981$		

Figures 4.1 and 4.2 show the Cy5 and LysoTracker$^{\mathrm{TM}}$ Blue fit emission distributions $f_{\mathrm{D}}(k_{\mathrm{o}})$, respectively. On the other hand, I assume that $|\boldsymbol{\mu}_{\mathrm{A}}| = 1.602 \times 10^{-29}$ Cm $= 4.802$ D (typical strength of a dipole electronic transition, an electron charge e displaced 1 Å) for both Cy5.5 and F2N12S fluorophores. Then, the Im$[\alpha_{\mathrm{A}}(k_{\mathrm{o}})]$ functions for Cy5.5 and F2N12S are obtained by using the aforementioned transition dipole strength $|\boldsymbol{\mu}_{\mathrm{A}}|$ and their corresponding fit distributions $f_{\mathrm{A}}(k_{\mathrm{o}})$ (see Figs. 4.1 and 4.2).

List of Figures

List of Tables

Bibliography

[1] R. Clegg, "The history of FRET: From conception through the labors of birth," in "Reviews in Fluorescence," vol. 3, C. D. Chris and J. Lakowicz, eds. (Springer, Berlin, 2006), pp. 1–45.

[2] F. Weigert, "Über polarisiertes Fluoreszenzlicht," Verh. d. D. Phys. Ges. **23**, 100–102 (1920).

[3] E. Gaviola and P. Pringsheim, "Über den Einfluss delr Konzentration auf die Polarisation der Fluoreszenz von Farbstofflösungen," Z. Physik **24**, 24–36 (1924).

[4] G. Cario, "Über Entstehung wahrer Lichtabsorption und scheinbare Koppelung von Quantensprüngen," Z. Physik **10**, 185–199 (1922).

[5] J. Perrin, *Fluorescence et radiochimie* (Gauthier-Villars, Paris, 1925), pp. 322–325, 2^{e} Conseil de Chimie Solvay.

[6] H. Kallmann and F. London, "Über quantenmechanische Energieübertragungen zwischen atomaren Systemen," Z. Phys. Chem. B **2**, 207–242 (1929).

[7] F. Perrin, "Théorie quantique des transferts d'activation entre molécules de méme espèce. Cas des solutions fluorescentes," Ann. Chim. Phys. (Paris) **17**, 283–314 (1932).

[8] J. R. Oppenheimer, “Internal conversion in photosynthesis,” Phys. Rev. **60**, 158 (1941).

[9] Th. Förster, “Energiewanderung und Fluoreszenz,” Naturwissenschaften **6**, 166–175 (1946).

[10] Th. Förster, “Zwischenmolekulare Energiewanderung und Fluoreszenz,” Ann. Phys. **437**, 55–75 (1948).

[11] G. M. Cooper and R. E. Hausman, *The Cell: A Molecular Approach* (ASM press, Washington, 2009), 5th ed.

[12] G. D. Scholes, “Long-range resonance energy transfer in molecular systems,” Annu. Rev. Phys. Chem **54**, 57–87 (2003).

[13] C. R. Kagan, C. B. Murray, M. Nirmal, and M. G. Bawendi, “Electronic energy transfer in CdSe quantum dot solids,” Phys. Rev. Lett. **76** (1996).

[14] S. A. Crooker, J. A. Hollingsworth, S. Tretiak, and V. I. Klimov, “Spectrally resolved dynamics of energy transfer in quantum-dot assemblies: Towards engineered energy flows in artificial material,” Phys. Rev. Lett. **89**, 186802 (2002).

[15] L. Strayer and R. P. Haugland, “Energy transfer: A spectroscopic ruler,” Proc. Natl. Acad. Sci. **58**, 719–726 (1967).

[16] Y. Suzuki, T. Yasunaga, R. Ohkura, T. Wakabayashi, and K. Sutoh, “Swing of the lever arm of a myosin motor at the isomerization and phosphate-release steps.” Nature **396**, 380–383 (1998).

[17] S. Rice, A. W. Lin, D. Safer, C. L. Hart, N. Narber, B. O. Carragher, S. M. Cain, E. Pechantnikova, E. M. Wilson-Kubalek, M. Whittaker, E. Pate, R. Cooke, E. W. Taylor, and R. A. Milligan, “A structural change in the kinesin motor that drives motility,” Nature **402**, 778–784 (1999).

[18] S. Myong, M. M. Bruno, A. M. Pyle, and T. Ha, “Spring-loaded mechanism of dna unwinding mechanism by hepatitis C virus NS3 helicase,” Science **317**, 513–516 (2007).

[19] E. M. Purcell, “Spontaneous emission probabilities at radio frequencies,” Phys. Rev. **69**, 681 (1946).

[20] J. Gersten and A. Nitzan, “Accelerated energy transfer between molecules near a solid particle.” Chem. Phys. Lett. **104**, 31–37 (1984).

[21] X. M. Hua, J. I. Gersten, and A. Nitzan, “Theory of energy transfer between molecules near solid state particles,” J. Chem. Phys. **83**, 3650 (1985).

[22] A. O. Govorov, J. Lee, and N. A. Kotov, “Theory of plasmon-enhanced Förster energy transfer in optically excited semiconductor and metal nanoparticles,” Phys. Rev. B **76**, 125308 (2007).

[23] M. Durach, A. Rusina, V. I. Klimov, and M. I. Stockman, “Nanoplasmonic renormalization and enhancement of Coulomb interactions,” New J. Phys. **10**, 105011 (2008).

[24] H. Y. Xie, H. Y. Chung, P. T. Leung, and D. P. Tsai, “Plasmonic enhancement of förster energy transfer between two molecules in the vicinity of a metallic nanoparticle: Nonlocal optical effects,” Phys. Rev. B **80**, 155448 (2009).

[25] J. Malika, I. Gryczynski, J. Fang, J. Kusba, and J. R. Lakowicz, “Increased resonance energy transfer between fluorophores bound to DNA in proximity to metallic silver particles,” Anal. Biochem. **315**, 160–169 (2003).

[26] J. Zhang, Y. Fu, and J. R. Lakowicz, “Enhanced Förster resonance energy transfer (FRET) on single metal particle,” J. Phys. Chem. C **111**, 50–56 (2007).

[27] J. Zhang, Y. Fu, M. H. Chowdhury, and J. R. Lakowicz, “Enhanced Förster resonance energy transfer on single metal particle. 2. Dependence on

donor–acceptor separation distance, particle size, and distance from metal surface," J. Phys. Chem. C **111**, 11784–11792 (2007).

[28] F. Reil, U. Hohenester, J. R. Krenn, and A. Leitner, "Förster-type resonant energy transfer influenced by metal nanoparticles," Nano Lett. **8**, 4128–4133 (2008).

[29] M. Lessard-Viger, M. Riou, L. Rainville, and D. Boudreau, "FRET enhancement in multilayer soreshell nanoparticles," Nano Letters **9**, 3066–3071 (2009).

[30] M. L.-Viger, D. Brouard, and D. Boudreau, "Plasmon-enhanced resonance energy transfer from a conjugated polymer to fluorescent multilayer coreshell nanoparticles: A photophysical study," J. Phys. Chem. C **115**, 2974–2981 (2011).

[31] V. Faessler, C. Hrelescu, A. A. Lutich, L. Osinkina, S. Mayilo, F. Jäckel, and J. Feldmann, "Accelerating fluorescence resonance energy transfer with plasmonic nanoresonators," Chem. Phys. Lett. **508**, 67–70 (2011).

[32] M. Lunz, V. A. Gerard, Y. K. Gun′ko, V. Lesnyak, N. Gaponik, A. S. Susha, A. L. Rogach, and A. L. Bradley, "Surface plasmon enhanced energy transfer between donor and acceptor CdTe nanocrystal quantum dot monolayers," Nano Lett. **11**, 3341–3345 (2011).

[33] T. Kobayashi, Q. Zheng, and T. Sekiguchi, "Resonant dipole-dipole interaction in a cavity," Phys. Rev. A **52**, 2835–2846 (1995).

[34] G. S. Agarwal and S. D. Gupta, "Microcavity-induced modification of the dipole-dipole interaction," Phys. Rev. A **57**, 667–670 (1998).

[35] C. A. Marocico and J. Knoester, "Intermolecular resonance energy transfer in the presence of a dielectric cylinder," Phys. Rev. A **79**, 053816 (2009).

[36] P. Andrew and W. L. Barnes, “Förster energy transfer in an optical cavity,” Science **290**, 785–788 (2000).

[37] C. E. Finlayson, D. S. Ginger, and N. C. Greenham, “Enhanced Förster energy transfer in organic/inorganic bilayer optical microcavities,” Chem. Phys. Lett. **338**, 83–87 (2001).

[38] P. Andrew and W. L. Barnes, “Energy transfer across a metal film mediated by surface plasmon polaritons,” Science **306**, 1002–1005 (2004).

[39] K. H. Drexhage, M. Fleck, F. Shäfer, and W. Sperling, “Beeinflussung der Fluoreszenz eines Europiumchelates durch einen Spiegel,” Ber. Bunsenges. Phys. Chem. **70**, 1179 (1966).

[40] G. Ford and W. Weber, “Electromagnetic interactions of molecules with metal surfaces,” Phys. Rep. **113**, 195–287 (1984).

[41] H. Metiu, “Surface enhanced spectroscopy,” Prog. Surf. Sci. **17**, 153–320 (1984).

[42] E. Betzig and R. J. Chichester, “Single molecules observed by near-field scanning optical microscopy,” Science **262**, 1422–1424 (1993).

[43] X. S. Xie and R. C. Dunn, “Probing single molecule dynamics,” Science **265**, 361–364 (1994).

[44] P. Anger, P. Bharadwaj, and L. Novotny, “Enhancement and quenching of single-molecule fluorescence,” Phys. Rev. Lett. **96**, 113002 (2006).

[45] F. Cannone, G. Chirico, A. R. Bizzarri, and S. Cannistraro, “Quenching and blinking of fluorescence of a single dye molecule bound to gold nanoparticles,” J. Phys. Chem. B **110**, 16491–16498 (2006).

[46] S. Kühn, U. Håkanson, L. Rogobete, and V. Sandoghdar, “Enhancement of single-molecule fluorescence using a gold nanoparticle as an optical nanoantenna,” Phys. Rev. Lett. **97**, 017402 (2006).

[47] J. Seelig, K. Leslie, A. Renn, S. Kuhn, V. Jacobsen, M. van de Corput, C. Wyman, and V. Sandoghdar, “Nanoparticle-induced fluorescence lifetime modification as nanoscopic ruler: Demonstration at the single molecule level,” Nano Lett. **7**, 685–689 (2007).

[48] D. L. Andrews, “A unified theory of radiative and radiationless molecular energy transfer,” Chem. Phys. **135**, 195–201 (1989).

[49] D. L. Andrews and G. Juzeliūnas, “Intermolecular energy transfer: Retardation effects,” J. Chem. Phys. **96**, 6606–6612 (1992).

[50] J. D. Jackson, *Classical Electrodynamics* (John Wiley & Sons, New York, 1998), 3rd ed.

[51] D. Chandler, *Introduction to Moderm Statistical Mechanics* (Oxford University Press, Oxford, 1987).

[52] G. S. Agarwal, “Quantum electrodynamics in the presence of dielectrics and conductors. I. Electromagnetic-field response functions and black body fluctuations in finite geometries,” Phys. Rev. A **11**, 230–242 (1975).

[53] L. Knöll, S. Scheel, and D.-G. Welsch, ”QED in Dispersing and Absorbing Dielectric Media,” in *Coherence and statistics of photons and atoms*, J. Peřina ed., (John Wiley & Sons, New York, 2001), pp. 1–64.

[54] H. T. Dung, L. Knöll, and D.-G. Welsch, “Intermolecular energy transfer in the presence of dispersing and absorbing media,” Phys. Rev. A **65**, 043813 (2002).

[55] H. T. Dung, L. Knöll, and D.-G. Welsch, “Resonant dipole-dipole interaction in the presence of dispersing and absorbing surrounding,” Phys. Rev. A **66**, 063810 (2002).

[56] L. Novotny and B. Hecht, *Principles of Nano-optics* (Cambridge University Press, New York, 2006).

[57] V. Namias, “Application of the dirac delta function to electric charge and multipole distributions,” Am. J. Phys. **45**, 624–630 (1977).

[58] G. B. Arfken and H. J. Weber, *Mathematical Methods for Physicists* (Academic Press, San Diego, 2005), 6th edition.

[59] C. F. Bohren and D. R. Huffman, *Absorption and scattering of light by small particles* (Wiley-VCH, Weinheim, 1983).

[60] C. D. Hahn, C. K. Riener, and H. J. Gruber, “Labeling of antibodies with Cy3-, Cy3.5-, Cy5-, and Cy5.5-monofunctional dyes at defined dye/protein ratios,” Single Mol. **2** (2001).

[61] B. Chazotte, “Labeling lysosomes in live cells with Lysotracker,” Cold Spring Harb. Protoc. **2011**, 5571 (2011).

[62] J. Hicks and J. Bradford, “A novel violet-laser excitable ratiometric probe for the detection of membrane asymmetry breakdown during apoptosis,” Poster at the XXV Congress of the International Society for Advancement of Cytometry (2010).

[63] U. Kreibig, “Electronic properties of small silver particles: the optical constants and their temperature dependence,” J. Phys. F:Met. Phys. **4**, 999 (1974).

[64] B. Persson, “Polarizability of small spherical metal particles: influence of the matrix environment,” Surf. Sci. **281**, 153–162 (1993).

[65] H. Hövel, S. Fritz, A. Hilger, U. Kreibig, and M. Vollmer, “Width of cluster plasmon resonances: Bulk dielectric functions and chemical interface damping,” Phys. Rev. B **48**, 18178–18188 (1993).

[66] A. Hilger, M. Tenfelde, and U. Kreibig, “Silver nanoparticles deposited on dielectric surfaces,” Appl. Phys. B **73**, 361–372 (2001).

[67] B. B. Dasgupta and R. Fuchs, “Polarizability of a small sphere including nonlocal effects,” Phys. Rev. B **24**, 554–561 (1981).

[68] S. Raza, G. Toscano, A.-P. Jauho, M. Wubs, and N. A. Mortensen, “Unusual resonances in nanoplasmonic structures due to nonlocal response,” Phys. Rev. B **84**, 121412(R) (2011).

[69] M. Boström and B. E. Sernelius, “Comment on: Calculation of the casimir force between imperfectly conducting plates,” Phys. Rev. A **61**, 046101 (2000).

[70] A. Lambrecht and S. Reynaud, “Casimir force between metallic mirrors,” Eur. Phys. J. D **8**, 309–318 (2000).

[71] E. D. Palik, *Handbook of optical constants of solids*, vol. 4 (Academic Press, San Diego, 1998).

[72] J. R. Zurita-Sánchez, “Quasi-static electromagnetics fields created by an electric dipole in the vicinity of a dielectric sphere: method of images,” Rev. Mex. Fís. **55**, 443–449 (2009).

[73] P. Bharadwaj and L. Novotny, “Spectral dependence of single molecule fluorescence enhancement,” Opt. Express **15**, 14266–14274 (2007).

[74] J. R. Zurita-Sánchez and L. Novotny, “Multipolar interband absorption in a semiconductor quantum dot. I. Electric quadrupole enhancement,” J. Opt. Soc. Am. B **19**, 1355–1362 (2002).

[75] J. A. Stratton, *Electromagnetic theory* (McGraw-Hill, New York, 1941), 1st ed.

[76] “Spectra data of molecular probes,” `http://www.invitrogen.com`.